Using MARS Spectral CT for Identifying Biomedical Nanoparticles

A thesis submitted in partial fulfilment of the

requirements for the Degree

of Doctor of Philosophy in Medical Physics

in the University of Canterbury

by Raja Aamir Younis

University of Canterbury

2013

To my late mother

Abstract

The goal of this research is to contribute to the development of MARS spectral CT and to demonstrate the feasibility of molecular imaging using the technology. MARS is a newly developed micro CT scanner, incorporating the latest spectroscopic Medipix photon counting detector. I show that the scanner can identify both drug markers and stenosis of atherosclerosis labelled with non-toxic nanoparticles. I also show that spectral computed tomography using Medipix x-ray detectors can give quantitative measurements of concentrations of gold nanoparticles in phantoms, mice and excised atheroma.

The characterisation of the Medipix2 assemblies with Si and CdTe x-ray sensors using poly-energetic x-ray sources has been performed. I measure the inhomogeneities within the sensors; individual pixel sensitivity response; and their saturation effects at higher photon fluxes. The effects of charge sharing on the performance of Medipix2 have been assessed, showing that it compromises energy resolution much more than spatial resolution.

I have commissioned several MARS scanners incorporating several different Medipix2 and Medipix3 cameras. After the characterization of x-ray detectors and the geometrical assessment of MARS-CT, spectral CT data has been acquired, using x-ray energies that are appropriate for human imaging. The outcome shows that MARS scanner has the ability to discriminate among low atomic number materials, and from various concentrations of heavy atoms. This new imaging modality, used with functionalized gold nanoparticles, gives a new tool to assess plaque vulnerability. I demonstrated this by using gold nanoparticles, attached to antibodies, which targeted to thrombotic events in excised plaque. Likewise, the imaging modality can be used to track drugs labelled with any heavy atoms to assess how much drug gets into a target organ. Thus the methodology could be used to accelerate development of new drug treatments for cancers and inflammatory diseases.

Academic contributions

During the course of this thesis, the candidate's aim was to contribute to the development of MARS CT scanners, the physics, the engineering, and to some of its possible applications to biology and medicine. The candidate has contributed to the following publications and achievements.

Peer-reviewed journal articles

1. **R Aamir**, S P Lansley, R Zainon, M Fiederle, A Fauler, D. Greiffenberg e, P H Butler & A P H Butler., Pixel sensitivity variations in a CdTe-Medipix2 detector using poly-energetic x-rays. Journal of Instrumentation, 2011. 6(01): p. C01059.

Initial results based on the characterization of Medipix2-CdTe sensor layer are reported. The sensitivity of 65,536 pixels over a hundred frames has been assessed. I gathered the required data and performed all the statistical analysis. These results are important in understanding the detection characteristics of the sensor layers for high-quality imaging (see Chapter 4 of this thesis).

2. **R Aamir**, M F Walsh, S P Lansley, R M Doesburg, R Zainon, N J A de Ruiter, P H Butler & A P H Butler., Characterization of CdTe x-ray sensor layer on Medipix detector chip, Materials Science Forum, 700, 170-173, 2011

CdTe is a complex material to use as a sensor layer and has a number of distinctive characteristics, not all of them fully understood. It was a sequel paper on the CdTe characterisation and wrinkle pattern instability. The paper also presents the applicability of high-Z sensors for imaging new radiographic pharmaceuticals containing high-Z nano-particles (see Chapter 4). I gathered the required data and performed all the statistical analysis.

3. Hengyong Yu, Qiong Xu, Peng He, James Bennett, **Raja Aamir**, Bruce Dobbs, Xuanqin Mou, Biao Wei, Anthony Butler, Philip Butler, Ge Wang., Medipix-based Spectral Micro-CT. CT Theory and Applications 21(4), 2012.

Two Ph.D students from Virginia Tech, USA, visited our lab in September 2011 to use MARS scanner. I shared the data gathering (see Chapter 5). The paper is a

review of recent progress of Medipix-based spectral micro-CT with the emphasis on the results obtained under collaboration of Virginia Tech and MARS group. It includes the state-of-the-art Medipix detector, the system and method of a commercial MARS spectral micro-CT, and the design and colour diffusion of a hybrid spectral micro-CT.

Refereed conference proceedings

1. **R Aamir**, N G Anderson, A P H Butler, P H Butler, S P Lansley, R M Doesburg, M Walsh & J L Mohr., Characterization of Si and CdTe sensor layers in Medipix assemblies using a microfocus x-ray sources, Nuclear Science Symposium and Medical Imaging Conference (NSS/MIC), 4766-4769, 2011 IEEE

This conference paper reports the comparison of dual CdTe-Medipix2 and Si-Medipix2 detectors. Observations were made of the measured versus expected noise in CdTe and Si sensor materials. We have performed a flat field correction and have demonstrated the improvement this has on image quality and finally CT-images with CdTe are presented. I gathered the required data and performed all the statistical analysis (see Chapter 4).

2. Nate D Tang, Niels de Ruiter, J. L Mohr, A. P.H. Butler, P. H. Butler & **R. Aamir**., Using Algebraic Reconstruction in Computed Tomography, Image and Vision Computing New Zealand, 2012 IVCNZ (manuscript accepted).

A new CT reconstruction algorithm for the MARS group has been developed in the MARS team. In this conference paper, a comparison of newly developed Algebraic Reconstruction with commercially available Octopus reconstruction software is presented. My work on data acquisition contributed in this paper (see Chapter 6).

3. Raj Kumar Panta**,** Karen Alt, Christopher Bateman, **Raja Aamir**, Joe Healy, Niels de Ruiter, Karlheinz Peter, Anthony Butler, Nigel Anderson, Christopher Hagemeyer, S. Gieseg., Spectral Molecular Imaging of Multiple Intrinsic and Gold Nano-particle Labelled Bio-markers in Ex-vivo Atheroma in Diagnostic Energy Range, Abstract submitted in Radiological society of North America (RSNA-2013), Chicago, USA, 1-6 December, 2013.

In this conference, simultaneous discrimination among components of vulnerable atherosclerotic plaque and labelled biomarkers by imaging their energy response using MARS spectral CT will be presented. I am one of the leading investigators on these experiments from MARS group (see Chapter 6).

4. **Raja Aamir**, Gabrielle Dachs, Elizabeth Campbell, Khaled Greish, Margreet Vissers, Christopher Bateman, Katie Saunders, Anthony P Butler, Nigel G Anderson., Spectral molecular imaging of gold nanoparticles as a marker of angiogenesis in implanted mouse tumours, Abstract submitted in Radiological society of North America (RSNA-2013), Chicago, USA, 1-6 December, 2013.

Initial results based on the quantification of gold nanoparticles accumulating in cancer implanted mice using spectral molecular imaging, will be presented. I am one of the leading investigators on these experiments from MARS group (see Chapter 6)

Invited disseminations

These papers were presented by Dr Anthony Butler on behalf of MARS team.

1. Butler, A. P. H., Walsh, M., Ronaldson, J. P., Opie, A., **R Aamir**., Doesburg, R., de Ruiter, N., Zainon, R., Mohr, J., Cook, N., Bones, P., & Butler, P. H. (2011). MARS: A pre-clinical spectral microCT system based on the Medipix family of energy selective photon-counting detectors. Workshop on medical applications of spectroscopic x-ray detectors. CERN, Geneva, April 2011.

2. Anthony Butler, Mike Walsh, Ronaldson, Nicola Scott, Rafidah, Zainon, Steven Geiseg, Tejraj Janmale, Nick Cook, Alex Opie, **R Aamir**, Robert Doesburg, Niels de Ruiter, Hengyong Yu, James Bennett, Ge Wang, Tim Woodfield, Phil Bones, Judy Mohr, Nigel Anderson, Phil Butler (2012). Functional computed tomography using energy resolved photon counting detectors. Workshop on Academia meets Industry: Solid-State Position Sensitive Detectors. Hamburg, Germany, 26-27 March 2012.

3. Anthony Butler, Mike Walsh, Ronaldson, Nicola Scott, Rafidah, Zainon, Steven Geiseg, Tejraj Janmale, Nick Cook, Alex Opie, **R Aamir**, Robert Doesburg, Niels de Ruiter, Hengyong Yu, James Bennett, Ge Wang, Tim Woodfield, Phil

Bones, Judy Mohr, Nigel Anderson, Phil Butler (2012). Improvement in material decomposition and image recovery. Annual meeting at CERN, Geneva, April 2012.

Awards/financial grants based on a substantial assessment

1. 2012, **Best presentation award** in Bioengineering Conference held in June 2012 at University of Canterbury.

The title reads "Imaging of gold nanoparticles in MARS-CT".

2. 2011, **Recipient of 2011 IEEE NSS / MIC / RTSD Trainee Grant**.

This internationally competitive grant was awarded to present a paper in Workshop on Room-Temperature Semiconductor x-ray and Gama ray Detectors held from 23-29 Oct 2011, Valencia, Spain.

3. 2009, **Recipient of a Ph.D scholarship.**

I was awarded a Ph.D scholarship in Medical Physics from MARS Bioimaging Ltd research grant for three years from Dec 2009 to date.

Accreditation during Ph.D studies

1. 2012, **Associate Member of the Australasian College of Physical Scientists and Engineers in Medicine** (ACPSEM). Membership Number: A838.

ACPSEM is the only accreditation body for Medical Physicists, Physical Scientists and Biomedical Engineers in Australia and New Zealand.

Acknowledgements

I would like to thank Dr. Phil Butler and Dr. Anthony Butler for supervising my doctoral study and providing me an opportunity to contribute in MARS group. I am also grateful for their encouragement and financial support from FRST (now MBIE) research grant (UOCX0805 MARS-CT). I am also thankful to Dr. Nigel Anderson from University of Otago (UO) for his time and fruitful discussions.

I thank Dr. Stuart Lansley from University of Canterbury (UC) for many discussions and corrections on my initial detector characterisation work. Thanks to Dr. Bruce Dobbs (Christchurch District Health Board) and Dr. Katie Saunders (UO) for their help in mice injections. I also wish to thank Graeme Kershaw (Physics Mechanical Lab, UC) for helping me in fabrication of various phantoms and mice preservations.

I also like to convey my thanks to all fellow MARS team members particularly my colleague, Dr. Robert Doesburg, for valuable discussions, and for proofreading my thesis. Thanks to Dr. Karen (Baker IDI, Australia), Tejraj Janmale (Free Radical Biochemistry Lab, UC) and Raj Panta (UO) for their support and contribution in plaque study.

Finally, I wish to express my love and gratitude to my family for their help and patience throughout this study.

Contents

List of Figures

List of Tables

1 Introduction

This thesis reports on the development of the MARS CT scanners, including the characterisation of their geometry, and the properties of the Medipix-based MARS cameras. It demonstrates that a MARS spectral CT scanner can image and quantify biological processes taking place at the molecular and cellular level by using gold nanoparticles labels. Once the technique is developed, its advantages include – but are not limited to – 1) the imaging, quantification and assessment of vulnerable atherosclerotic plaque, 2) non-invasive anticancer drug development, 3) assessment of tumour response to treatment, and 4) quantification of drug gets into a tumour and 5) toxicity measurement to adjacent normal tissue. The same methodology can be further applied to other inflammatory diseases e.g., drugs to pneumonia and perhaps drugs to rheumatoid arthritis.

This thesis also analyses the sensitivity of more than 65,000 pixels for silicon (Si) and cadmium telluride (CdTe) assembled Medipix2 detectors. It evaluates the geometrical assessment of MARS scanners to deal with system related artefacts and their calibrations. The mechanical and geometrical alignment of the MARS-CT scanners was conducted in stages by fabricating customized phantoms. Motor driven movements have been plotted to check the measured displacement against corresponding index values.

Spectral computed tomography images tend to display information regarding energy based attenuation as different colours. Spectroscopic performance of MARS scanners, using CdTe Medipix2 and energy settings that are appropriate for human imaging, is evaluated for: simultaneous discrimination among low Z (atomic number) materials, and from various concentrations of high Z materials. This work will demonstrate the potential molecular imaging feature of MARS CT. The outcome proposed it as a new quantitative imaging tool with potential to make advances in non-invasive spectral molecular imaging at high spatial resolution.

My contribution in the MARS project is already highlighted in previous section of Academic contribution. This chapter includes my motivation for spectral imaging with high Z sensor materials, and contrast agents in sections 1.1 and 1.2 respectively. Clinical significance of my research is highlighted in section 1.3. A brief overview of the concept

of the spectral CT imaging and some of its benefits over conventional CT and dual energy CT will be given in section 1.5. The chapter also provides the outline for the rest of the thesis in section 1.6.

1.1 Motivation for spectral imaging with high Z sensors

The best understood sensor (detector) is Si due to the availability of good quality homogeneous material, and high transport properties of the charge carriers. However, Si sensors are almost transparent to x-rays above 30 keV. Distinguishing higher-Z contrast agents, such as gold (incorporated into nanoparticles), requires the use of x-ray energies upwards of 100 keV and thus higher-Z semiconductor sensors such as CdTe. 1 mm thick CdTe material offers absorption probability of more than 60% at energies up to 107 keV, making it suitable for the human diagnostic energy range (10 to 150 keV). It is underlined that the Medipix "flip-chip" design permits various sensors to be bump-bonded to the Medipix chip. Sensor materials include Si, GaAs, and CdTe for preclinical and clinical x-ray energy ranges (Yu, Xu et al. 2012). For most of this project, CdTe bump-bonded to a Medipix2 ASIC has been used, CdTe bonded to a Medipix3-RX has recently been received from Freiburg University and is being tested (at the time of writing).

1.2 Motivation for spectral imaging with high Z contrast agents

For this thesis, elements with more than 40 protons in the nucleus are referred as heavy atoms. Atoms heavier than this have unique spectral attenuation properties, i.e. K-edges of a suitable energy that make them easy to identify with spectroscopic detectors. The heavy atoms that I have quantified by using CdTe-Medipix2 include iodine, gadolinium and gold nanoparticles. These are found in standard radiological pharmaceuticals, e.g., Ultravist (non-ionic iodine), Magnevist (chelated gadolinium) and Aurovist (gold nanoparticles).

This project tests gold nanoparticles in MARS spectral CT to develop a technique for in-vivo scanning of mice injected with gold nanoparticles to translate the study into different mouse models; the feasibility of using functionalized gold nanoparticles for visualization and quantification of selectively targeted thrombotic events and cancer cells.

Gold nanoparticles have recently received much attention for the development of new CT imaging agents. Due to the higher Z, gold nanoparticles have an enhanced x-ray absorption coefficient, which resulting in ~3 time higher contrast than typical iodine agents. They also demonstrate a prolonged circulation profile in the blood pool and lower toxicity in vivo. They provide a high degree of flexibility in terms of functional groups for coating and targeting. Gold nanoparticles can be bound to drugs or targeted to tumour biomarkers or added to antibodies to attach at desired sites.

1.3 Clinical significance

The research has high significance in clinical imaging due to its applications to biology and medicine. It has the potential to make major advances in non-invasive spectral molecular imaging by utilizing nanoparticles in MARS spectral CT. The MARS scanner can image and quantify molecular specific biological processes and therefore have shown the presence of binding nanoparticles in regions with activated platelets of human plaque. The detection of plaque vulnerability is critical for preventing the severe downstream effects of heart disease. The technique could be further extended for early detection of tumour, the assessment of tumour response to treatment and anticancer drug toxicity measurement to adjacent normal tissues.

1.4 MARS spectral CT

Our team has developed a scanner using the latest photon-counting detector technology. It is suitable for preclinical spectral imaging of small animal models and human samples of disease. It is the Medipix photon-processing x-ray detector that allows for spectral computed tomography imaging and measures the number and energy of each x-ray photons (Llopart, Campbell et al. 2002; Ballabriga, Campbell et al. 2006). By measuring the energy of the x-rays using a photon processing detector, specific identification and quantification of the materials becomes possible making it a very innovative molecular imaging modality (Anderson, Butler et al. 2010). The combination of high spatial resolution with specific identification and quantification of multiple soft tissue components, non-invasively, is unique (Ronaldson, Butler et al. 2011). Different materials within a conventional CT image may have the same measurement at certain

concentrations and, therefore, cannot be differentiated from each other. MARS scanner is able to discriminate up to six elements at a time and is also translatable to human imaging. The current version of MARS scanner can image dead mice/rats; the next version, capable of live scanning, is in development.

1.5 What is spectral CT?

Photons from the wide x-ray spectrum are attenuated to different degrees depending on material's atomic composition. The attenuations of different materials are encoded by greyscale (Hounsfield Units or CT number). Conventional CT measures the attenuated signal over the entire range of the broad x-ray spectrum. However, different materials within a conventional CT image may have the same CT numbers at certain concentrations and, therefore, cannot be differentiated from each other. Figure 1.1 shows diagrammatically the evolution of CT imaging from conventional CT (top) to spectral CT (bottom).

Alvarez proposed the application of dual energy CT in 1976 (Alvarez and Macovski 1976). In current commercial dual-energy CT systems, materials can be differentiated either by having two x-ray tubes operating at different voltages or one tube quickly switching between voltages. Analysis techniques of the data show the varying response of material attenuations to two energies. The first commercial dual-energy CT scanner was developed by Siemens in 2006 (Flohr, McCollough et al. 2006). It offers the potential for a range of CT applications, like bone removal by a post-processing technique (Yamamoto, McWilliams et al. 2009), discrimination of calcium from iodine contrast material (Tran, Straka et al. 2009), kidney stone analysis, e.g., discrimination between stones containing uric acid and others (Stolzmann, Scheffel et al. 2008), abdominal imaging (Graser, Johnson et al. 2009) and in several others areas. Figure 1.1 (middle) shows dual-energy CT signal detection. However, dual-energy CT is limited to two energies and does not have a long term future due to a few drawbacks. Materials with closely related attenuation curves cannot be discriminated by dual-energy CT (Fornaro, Leschka et al. 2011). Another disadvantage is that an increased radiation dose is often required (Brenner and Hall 2007; Achenbach S 2008).

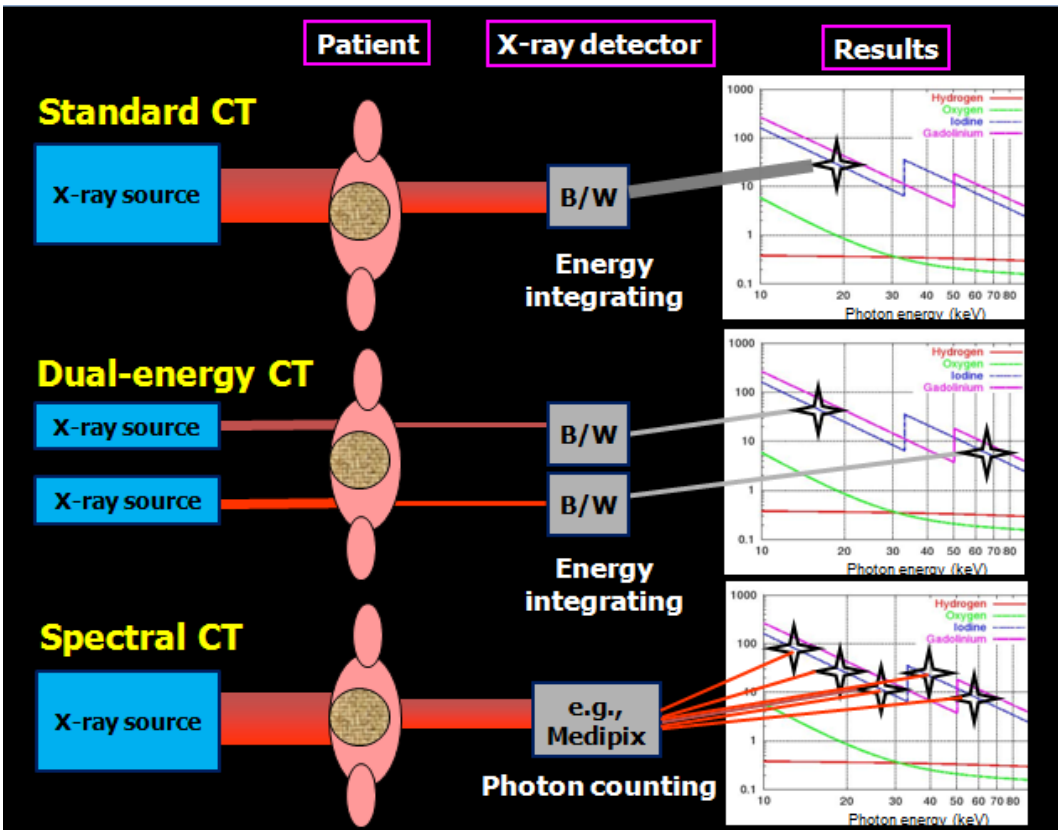

Figure 1.1 Illustration of differences between conventional CT (top), dual source CT (middle) and MARS spectral CT (bottom). Conventional CT measures attenuation over the entire broad spectrum, and dual-energy detects two attenuated spectra, whereas MARS spectral scanner detects the attenuated signal at different energies by using Medipix technology. Overall, this figure was first generated by Anderson (Anderson, Butler et al. 2010) but it is taken specifically from Rafidah's PhD thesis (Zainon 2012).

These problems can be solved by using a broad spectrum x-ray source, such as used in conventional CT, but with an energy resolving detector that can discriminate different materials within the same voxel. The MARS spectral CT scanner, incorporated with Medipix detector, divides a single wide spectrum into a separate energy bins to extract energy information from the x-ray beam as shown in Figure 1.1 (bottom). The Medipix photon-processing detector allows for K-edge imaging, which specifically identifies and differentiates high atomic number materials. K-edge imaging is based on the principle of imaging a narrow energy band on either side of the K absorption edge of high Z elements (Roessl and Proksa 2007). The Medipix2-MXR chip, with a CdTe sensor layer, measures up to 6 biomarkers simultaneously at a spatial resolution of 150-170 μm (see Chapter 6). It is hard to predict the full clinical significance of spectral CT, but an overview can be

gained by looking into the clinical results of: discrimination between iodine and barium by spectral CT (Anderson, Butler et al. 2010; Butler, Butzer et al. 2011), spectral imaging of atherosclerotic plaque (Zainon, Ronaldson et al. 2012), soft tissue quantification (Butler, Anderson et al. 2008; Melzer, Cook et al. 2008; Ronaldson JP 2011; Ronaldson 2012; Zainon 2012), imaging of gold nano-particles (to be discussed in Chapter 6) and various other research areas.

However, the performance of Medipix2 is limited by charge sharing over neighbouring pixels, compromising energy resolution much more than spatial resolution. To address this issue, Medipix3 was developed as a photon-processing chip (Ballabriga, Campbell et al. 2006). Special circuitry for each pixel in Medipix3 allows charge deposition in adjacent pixels to be summed and analyzed with two simultaneous energy thresholds without spectral distortion. The readout logic also supports eight energy thresholds over 110 × 110 μm for spectroscopic imaging. A detailed literature review of photon counting detectors and Medipix will be discussed in sections 3.3.2 and 3.5 respectively.

1.6 Thesis outline

This thesis will show experimental work for identifying biomedical nanoparticles in MARS-CT. The early chapters will review relevant background of x-rays physics and then provide an overview of x-ray detectors. The later chapters then describe the candidate's developmental and investigative work for: 1) characterization of different x-ray sensor layers assembled on Medipix2 detectors, 2) geometrical assessment of MARS scanner, and 3) quantitative measurements of concentrations of gold nanoparticles in phantoms, mice and excised atheroma.

Chapter 2 will provide an overview of the mechanism of diagnostic x-ray tube, production of x-rays and their interactions with matter. It also describes the photon beam attenuation and its attenuation factors.

Chapter 3 will outline the concept of x-ray detection and charge propagation in the field of medical imaging. After discussing two detection systems by the way of their interaction, detectors with digital output will be reviewed. The concept of hybrid

detectors along with single photon counting Medipix detectors will be discussed after wards. Finally, operating mode of Medipix detector and their energy discrimination capability will be reviewed.

In chapter 4, we will report a summary of the observations presented in (Aamir, Lansley et al. 2010; Aamir, Anderson et al. 2011; R Aamir 2011a). The necessary basics of semiconductor physics will be reviewed in earlier sections. Finally, results from characterization of Si and CdTe sensor layers will be presented.

Chapter 5 is based on the geometrical quality assurance routines for MARS-CT and describes its geometrical assessment. This chapter includes the mechanical and geometrical alignment of the MARS-CT scanner, image assessment with the CdTe Medipix2 detector, spatial resolution, linearity and spectroscopic response, and images of biological samples.

Chapter 6 is based on the feasibility study to demonstrate that MARS CT is a quantitative imaging tool with potential to make major advances in non-invasive assessment of inflammatory diseases. A few results from this chapter were reported in the 27th Image and Vision Computing New Zealand (IVCNZ 2012) held at Dunedin, NZ (26th to 28th Nov). This chapter includes a brief overview of the limitations of current imaging modalities for the assessment of vulnerable plaque and tumour response to treatment. It describes working principle of nanoparticles as radiographic pharmaceuticals. Gold nanoparticles and their advantages over conventional contrast agents and the criteria for their selection into this project will be highlighted. Spectroscopic discrimination and quantitative measurements of concentrations of gold nanoparticles in phantoms, mice and excised atheroma will be shown afterwards. This chapter confirms that the MARS scanner has the ability to discriminate various high atomic number radiographic pharmaceuticals along with the assessment of plaque vulnerability by using functionalized gold nanoparticles.

2 Production and interaction of x-rays

2.1 Overview

This chapter will serve as a refresher for those readers who haven't had prior knowledge of x-rays and their interaction so that the rest of the thesis makes sense to them.

X-rays were discovered by W. C Roentgen in 1895 while studying cathode rays (streams of electrons) in a gas discharge tube. He observed that another type of radiation is also produced during that process due to the interaction of cathode rays which can penetrate opaque substance and effect photographic plate, with the glass surface. These were named x-rays.

Since then, x-rays have been extensively studied and used in many fields like material analysis, baggage inspection, and security check points, and more importantly in medical imaging. In this chapter, we will overview the concept of x-ray tube in section 2.2 and then production of x-rays in section 2.3. Physics of x-ray interaction will be discussed in section 2.4 and finally, photon beam attenuation and its attenuation factors will be reviewed in section 2.5.

2.2 The x-ray tube

Figure 2.1 is a schematic representation of a conventional x-ray tube. The x-ray tube consists of a highly evacuated glass envelope, at one end of which is the cathode (-ve electrode) and at the other end an anode (+ve electrode). The cathode is a tungsten (W) filament which when heated produces electrons via thermionic emission, whereas anode consists of a thick copper rod at the end of which a small piece of tungsten target is attached. Emitted electrons travel towards the anode and are accelerated to high speed due to a voltage applied between cathode and anode. X-rays are produced due to the sudden deflection or acceleration of electrons caused by attractive forces of a tungsten nucleus. The physics of x-rays production will be discussed in section 2.3. The x-ray

beam will come out through the beryllium and glass windows in the tube envelope as shown in Figure 2.1.

The choice of tungsten material as a target is based on the criteria of high atomic number (Z=74), as x-rays efficiency is Z dependent. In addition, tungsten has a high melting point (3370 ºC) providing it an ability to withstand intense heat produced in the target by the electronic bombardment. Removal of heat from target is carried out by the thick copper anode to the outside of tube where it is cooled by oil, water or air. Additionally, some medical imaging systems have rotating anodes to reduce the target temperature at any specific point. It is important to mention that oil not only absorbs heat from the anode but also isolates the tube housing from the high tube voltage.

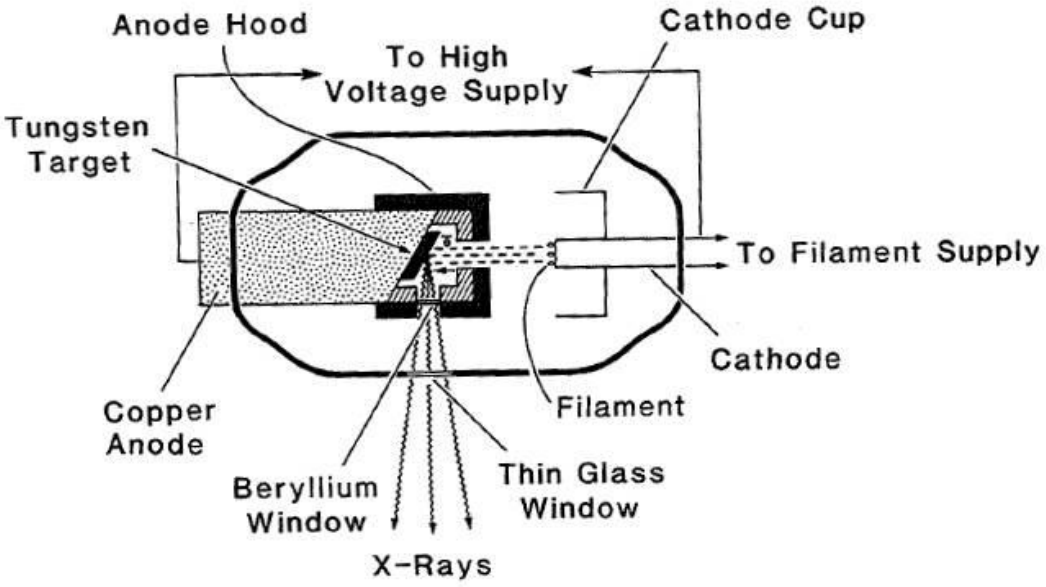

Figure 2.1 Schematic of x-ray tube with fixed anode (Khan 2003).

Some stationary anodes are hooded by copper and tungsten shielding (see Figure 2.1) to prevent stray electrons from striking non-target components of the x-ray tube. These are secondary electrons produced in the target due to the primary electron beam. Copper in the hood absorbs these secondary electrons whereas the tungsten shield surrounding the copper absorbs x-rays produced in the copper.

2.2.1 Focal spot and heel effect

An important requirement of the anode design is choosing the optimum size of the target area from where x-rays will emerge, also known as the "focal spot". This focal spot should be as small as possible to produce sharp images with good spatial resolution, but smaller focal spots produce more heat per unit area of target, therefore, limit current and exposure (J. T. Bushberg 2002). The apparent focal spot size can be reduced by the principle of line focus, as shown in Figure 2.2. This principle allows a fairly large area of the target to be exposed to electrons while retaining a small projected focal spot. The target is attached to the steeply inclined surface of the copper anode as shown in Figure 2.2. The apparent side 'x' is equal to '$x = l \sin\theta$', where 'l' is the side of the actual focal spot at an angle 'θ' with respect to electron beam. Since the other side 'w' of the focal spot is perpendicular to the electron beam, there will be no effect on its apparent length. The dimensions of the actual focal spot are chosen so that the apparent focal spot results in an approximate square. In computed tomography, very small target angles (5º - 7º) are used to reduce 'x' to a desired size. Although this approach has the advantage of increase exposure area, it may have minor problem. The focal spot's size and shape is location dependent which means that away from the iso-line, the focal spot shape is no longer square or rectangular, but is a trapezoid and may affect the CT image quality (Hsieh 2003; Khan 2003; La Riviere and Vargas 2008).

Since the x-rays are produced at various depths in the target material, there will be higher attenuation for x-rays coming from greater depths than those from near the surface of the target. Consequently, the x-ray beam intensity is not entirely uniform and decreases from the cathode to the anode direction of the beam. X-rays are emitted from the target area in a conical shape, resulting in absorption of some photons within the target because they have to travel through more target material than those which are on the cathode side. This variation across the x-ray beam is called the "heel effect". This effect is more pronounced in the diagnostic energy range due to lower energy x-rays and steep target angles. Braun (Braun, Kyriakou et al. 2010) has studied the influence of the heel effect in cone-beam computed tomography.

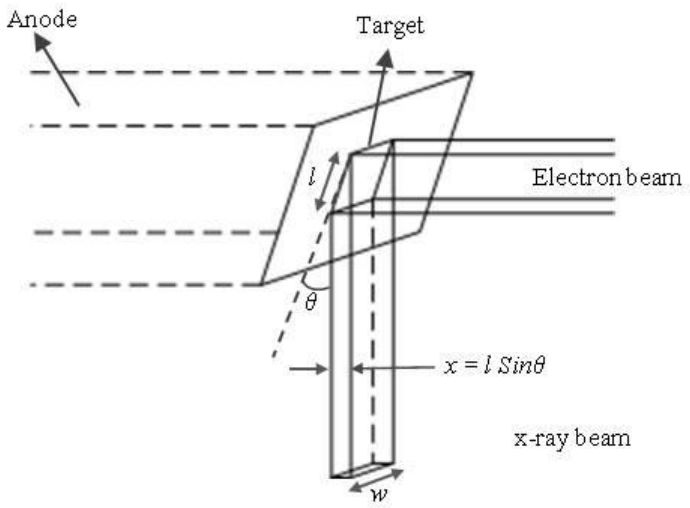

Figure 2.2 Illustration of line focus principle. Side 'l' of actual focal spot is reduced to 'x' in the apparent focal spot. The other dimension 'w' (perpendicular to the electron beam) of the focal spot remains unchanged.

2.3 Physics of x-ray production

Before we proceed to x-ray interaction with matter, we will quickly review the production of x-rays. Two different mechanisms are involved in the production of x-rays. One is bremsstahlung, the other is characteristic x-rays.

2.3.1 Bremsstrahlung

The process of bremsstrahlung (braking radiation) is a result of radiative collision between a high speed electron and a nucleus of the target material. The electron, while passing near the nucleus, experiences a Coulomb force of attraction and deflects from its original path. The sudden deflection reduces its kinetic energy. This loss of kinetic energy of the electron appears as x-rays. Since an electron may interact through one or more bremsstrahlung event and interactions may cause partial or complete loss of energy of the incident electron, the resulting bremsstrahlung radiation may have energy up-to the initial energy of electrons. Also, the direction of bremsstrahlung radiation depends on the initial energy of electrons. At electron energies upto around 100 keV, as shown in Figure 2.3, x-rays are emitted in all directions, while as the energy increases, the direction of x-rays

becomes increasingly forward. Therefore, transmission type targets are used in higher energy x-ray tubes (radiotherapy range).

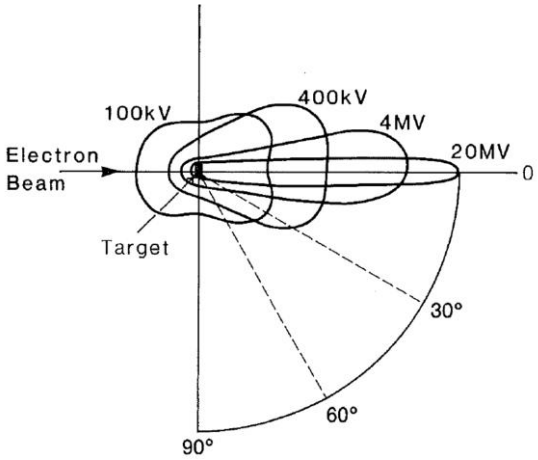

Figure 2.3 Schematic illustration of the spatial distribution of x-rays around a target material due to an incident electron beam (Khan 2003).

2.3.2 Characteristic x-rays

The binding energy of electrons in a particular orbit depends on the magnitude of Coulomb forces of attraction between the nucleus and the orbital electrons. The closer the orbit, the higher the binding energy. Now, if an incident electron with kinetic energy 'E_o' interacts with the target atom, it may ionize it by ejecting one of its orbital electrons. The incident electron will recede from the collision and travel with energy '$E_0 - \Delta E$', where 'ΔE' is the energy given to eject the orbital electron.

A part of the 'ΔE' energy is spent to overcome the binding energy of the electron and the rest is taken as the kinetic energy of the ejected electron (see Eq (2.2)). To fill the vacancy created by the ejected electron, an outer orbital electron falls down and in doing so, the energy is radiated in the form of electromagnetic radiation known as Characteristic radiation. Unlike bremsstrahlung, characteristic x-rays are emitted at discrete energies. If the transition involves inner shells like K, L or M where electrons are tightly bound, then the released energy will be high enough to be considered as part of the x-ray spectrum. A threshold energy (critical absorption energy or work function) is required to eject an electron from its respective orbit, i.e.,

$$hv = E_K - E_L \qquad (2.1)$$

Here h is Plank's constant (h = 6.63× 10^{-34} kgm^2/s), v is the frequency, E_K and E_L are the binding energies of the K and L shell respectively.

Figure 2.4 shows the calculated x-ray spectrum of 120 kV tube voltage having 1.8-mm-Al-filteration. The broad spectrum shows continuous radiations (bremsstrahlung) generated from deceleration of electrons by nucleus; whereas, characteristic x-rays are represented by sharp peaks, produced by the tungsten target material. As seen in the Figure 2.4, bremsstrahlung has a major contribution in diagnostic procedures.

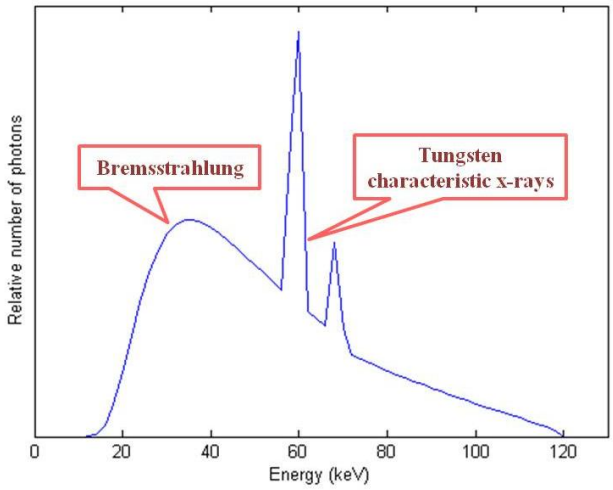

Figure 2.4 A typical x-ray spectrum by 120 kV tube voltage with a 12° tungsten target and 1.8-mm-Al filtration calculated by SpekCalc software (Poludniowski, Landry et al. 2009).

2.4 Interactions of low energy photons with matter

Charged particles (electrons, protons and α particles) interact with matter principally by ionization and excitation. Radiative collisions, where a charged particle interacts by bremsstrahlung are possible but are much more likely with electrons (see section 2.3.1). X-rays/photon beams are attenuated by absorbing material by five major types of interactions, namely: Photoelectric absorption, Rayleigh scattering, Compton scattering, Pair production and Photon disintegration. The last two processes occur at energies 1.02 MeV and >10 MeV respectively, well above the diagnostic energy range (10 keV to 150

keV). Therefore, only the first three processes will be discussed. An illustration of x-rays that are transmitted with and without interaction is shown in Figure 2.5.

2.4.1 Photoelectric absorption

Photoelectric absorption involves the interaction of an incident photon with an inner shell electron. In this process, the orbital electron absorbs the energy of the incident photon and is ejected from its orbit (usually K shell) with a kinetic energy equal to the difference of the binding energy of orbital electron 'E_{BE}' and the incident photon energy 'E_o' as shown in Figure 2.5 (B) i.e.,

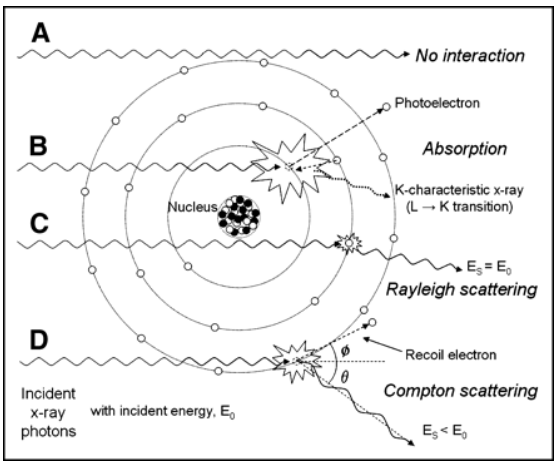

Figure 2.5 Illustration of three x-ray interactions. (A) Unattenuated beam, (B) photoelectric absorption, (C) Rayleigh scattering and (D) Compton scattering (Seibert and Boone 2005).

$$K.E_{electron} = E_o - E_{BE} \qquad (2.2)$$

After the electron has been ejected from the atom, the vacated electron shell is subsequently filled by an outer orbital electron (e.g., from the L or M shell) with the emission of characteristic x-rays. There is also a probability of emission of an 'Auger electron', which are produced by the absorption of characteristic x-rays internally by the atom; they are mono-energetic. The terms K-edge or L-edge are absorption edges corresponding to the binding energies of K and L shells. If the energy of the incident photon is less than the binding energy of the electron, photoelectric interaction cannot occur, but for '$E_o = E_{BE}$', the probability of photoelectric effect is high. With the further

increase in energy beyond this point, the likelihood of the photoelectric absorption is shown in Eq (2.3)

$$\tau \propto Z^3/E^3 \qquad (2.3)$$

Where 'τ' is the probability of photoelectric effect, 'Z' is the atomic number of the target material and 'E' is the incident photon energy. Therefore, the probability of photoelectric effect increases with increasing atomic number and decreasing photon energies.

Eq (2.3) forms the basis for many applications in diagnostic radiology. Tissues (effective Z ≈ 7.5) in the human body are composed of low atomic number elements (e.g., hydrogen, Z = 1; carbon, Z = 6; nitrogen, Z = 7; and oxygen, Z = 8) and therefore the probability of photoelectric absorption for Z < 10 is close to zero since diagnostic x-ray energies are in the 10 – 150 keV. However, for higher atomic number elements (e.g., iodine, Z = 53; gadolinium, Z = 64; and gold, Z = 79; used as biomedical contrast agents), the probability of photoelectric absorption with respect to equal thickness of soft tissue at a specific energy is approximately $(53/7.5)^3 \approx 350$ times greater (Seibert and Boone 2005). Similarly, a 50 keV compared with a 100 keV x-ray photon is $1/(50/100)^3 = 8$ times more likely to interact with photoelectric absorption.

2.4.2 Rayleigh scattering

Rayleigh scattering, also known as classical scattering, coherent scattering or elastic scattering is shown in Figure 2.5 (C). As the name classical scattering suggests, the process can be visualized by considering the wave nature of electromagnetic radiation. This interaction consists of an electromagnetic wave passing through the electrons that result in raising their energy and setting them into oscillations without removing the electron from its orbit. The oscillating electrons reradiate the energy in the form of x-rays. These scattered x-rays have the same wavelength as the incident beam but with a small angular change in direction. The probability of coherent scattering 'σ_{coh}' is increased in high atomic number materials with low energies. In the diagnostic energy

range, the probability of coherent scattering in soft tissue is ~ 5% of all scattering events because of the low effective atomic number of soft tissues ($Z \approx 7.5$).

2.4.3 Compton scattering

In the Compton scattering process, a photon interacts with an atomic electron which is regarded as a free electron. The term free electron means that the incident photon energy is much greater than the binding energy of the electron ($E_o \gg E_{BE}$). The photon transfers part of its energy to the electron and is scattered at an angle 'θ' with '$E_s < E_o$', as shown in Figure 2.5(D). The scattered photon may travel at any angle between 0° and 180°. The recoil electron with absorbed energy is emitted at an angle 'ϕ'. This electron may travel at any angle from > 0° to 90°. Figure 2.6 shows the angular distribution of scattered photon and recoil electron.

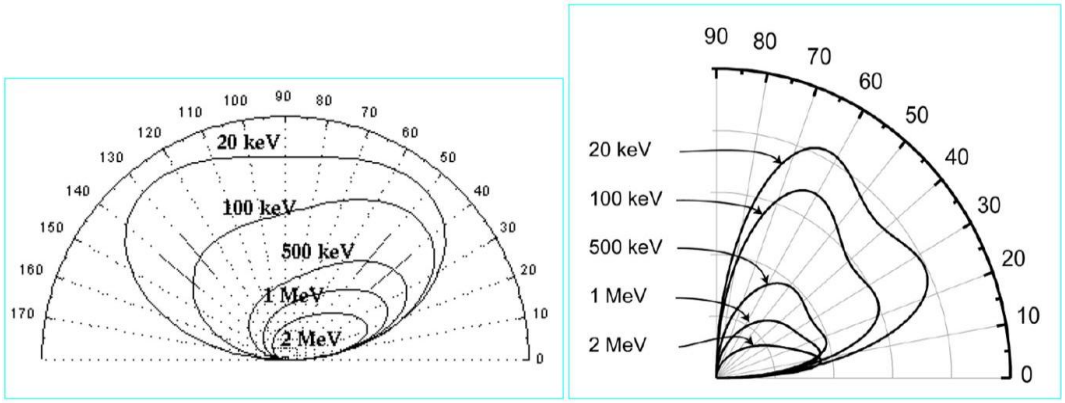

Figure 2.6 Angular distribution of scattered photon (left) and recoil electron (right) for primary photon energies (Mikulec 2000).

Compton scattering can be visualized in terms of a collision between two particles (photon and electron). By applying law of conservation of energy and momentum, the energy of the scattered photon is given by the Klein Nishina equation

$$\frac{E_s}{E_o} = \frac{1}{1 + \frac{E_o}{511\ keV}\ (1 - cos\theta)} \qquad (2.4)$$

Here 'E_o' and 'E_s' are the incident and scattered energies and 511 keV is the rest mass energy of the electron. This equation shows that the scattered x-ray energy becomes smaller with increasing scattered angle.

As Compton interaction involves a so called free electron, it is independent of atomic number 'Z'. Thus, the probability of Compton scattering 'σ_c' is nearly the same for all elements. It is also independent of energy, although at higher energies, the probability of Compton scattering decreases as approximately $1/E_o$ (Alvarez and Macovski 1976).

2.5 Photon beam attenuation and its attenuation coefficients

While passing through the absorbing material, a photon beam is attenuated due to various interactions corresponding to their energy range, as described in section 2.4, which means that the total attenuation coefficient is the sum of individual interaction mechanisms. The attenuation process represents the number of photons removed from the incident beam and depends on the thickness of the absorber. Therefore, the number of transmitted photons 'dN' are proportional to the number of incident photons 'N' and to the thickness of the absorber 'dx'. Mathematically

$$dN \propto Ndx \tag{2.5}$$

$$dN = -\mu Ndx \tag{2.6}$$

Where 'μ' is a constant of proportionality known as *the attenuation coefficient*. The negative sign indicates that number of photons decreases as the thickness of absorber increases. The above equation can also be written in terms of intensity 'I',i.e.,

$$dI = -\mu Idx \tag{2.7}$$

$$\frac{dI}{I} = -\mu dx \tag{2.8}$$

If thickness 'x' is expressed in terms of length (e.g., in centimetres), then 'μ' is called the *linear attenuation coefficient* and its unit is cm^{-1}.

The linear attenuation co-efficient can be different/vary for the same material if it has differences in density. Since the attenuation produced by a thickness 'x' of the absorber depends on the number of electrons present in that thickness, 'μ' is density dependent. Therefore by dividing 'μ' by density 'ρ', the resulting co-efficient will be independent of density and is known as the mass attenuation co-efficient. Its units are cm^2/g. Figure 2.7 shows x-ray interactions and mass attenuation co-efficient for soft tissues as a function of energy. Just like the linear attenuation co-efficient for any specific material, total mass attenuation co-efficient is the sum of all interaction probabilities:

$$\frac{\mu}{\rho} = \frac{\tau}{\rho} + \frac{\sigma_{coh}}{\rho} + \frac{\sigma_c}{\rho} + \frac{\pi}{\rho} \qquad (2.9)$$

Here 'π' is the probability of pair production.

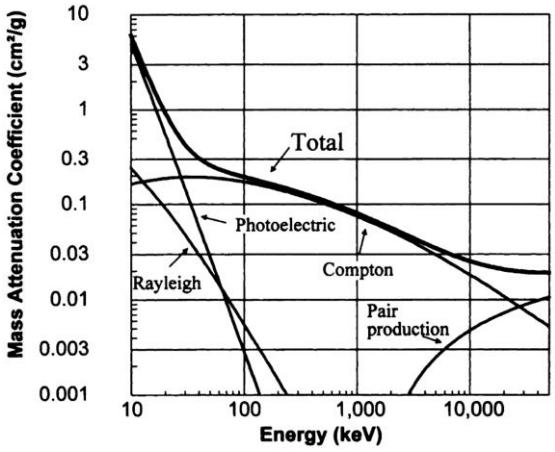

Figure 2.7 Rayleigh scattering, photoelectric absorption, Compton scattering, pair production and mass attenuation co-efficient for soft tissues (Z ≈ 7.5) are plotted as a function of energy (Bushberg 1998).

2.6 Summary

In this chapter, we have reviewed the mechanism of diagnostic x-ray tube, production of x-rays and their interactions with matter and photon beam attenuation.

All photon beams produced by x-ray tubes are heterogeneous in energy due to continuous energy spectra that depends on tube voltage and tube target material. These heterogeneous photons are attenuated while passing through the absorbing material. In the diagnostic energy range (10 keV – 150 keV), the probability of Rayleigh scattering is less than 5%, whereas photoelectric absorption can be approximated by $\tau \propto Z^3/E^3$. Compton scattering is independent of atomic number 'Z' and incident energy 'E_o', which means that it predominate in diagnostic radiology but that at higher energies it decreases with increase in energy, $\sigma_c \propto 1/E_o$.

3 Detectors in x-ray imaging

3.1 Overview

This chapter will outline the concept of x-ray detection and propagation of electrons and holes in the semiconductor used in the field of medical imaging. In section 3.2, the detection systems are categorized by the way they interact with x-rays. Section 3.3 describes two main approaches to detectors with digital output. The concept of hybrid detectors along with single photon counting Medipix detectors will be discussed in sections 3.4 and 3.5. In section 3.6, a short description of single carrier board for multi Medipix chips will be mentioned and finally, operating mode of Medipix detector will be discussed.

Detector technology has passed through various improvements since the discovery of x-rays by W.C. Roentgen in 1895, but modern systems are still based on the same basic concepts of charge generation. Overall, all detection systems are categorized by the way they interact with x-rays (direct and indirect) and by how they transfer charge (photon counting and charge integrating) to readout.

3.2 Direct and indirect detection systems

In medical imaging, x-rays interact with detector material by the photoelectric effect or Compton scattering (section 2.4). Depending on the type and energy of x-rays, charge is produced by direct or indirect x-ray conversion.

In direct detection systems, x-rays produce charge (electron hole pairs) in the sensor material by the photoelectric effect. If this induced charge is transferred directly to the nearest electrode by the help of an externally applied bias voltage to the detector surface, then these systems are known as direct detection systems. Direct detectors offer high spatial and energy resolution (Jurgen 2005; Fujita, Matsue et al. 2011). These detection systems are further categorized by their charge propagation and will be discussed in more detail in section 3.3.

Indirect detection systems (scintillators) typically have an intermediate layer (scintillation layer) to convert x-rays into visible light (fluorescence). These focus visible photons (sometimes also amplified) that are detected by photodiodes. Photodiodes convert the light signal into an electrical signal and transfer the generated charges to the charge sensitive amplifier. The most commonly used scintillation crystals are made of bismuth germinate (Bi_4GeO_{12}) and cadmium tungstate ($CdWO_4$). Indirect detection systems are much less efficient than direct detection in terms of overall conversion of x-rays into electron-hole pairs. Their spatial resolution and sensitivity is also affected by optical diffusion. More detailed consideration of scintillator materials and their conversion mechanism can be found in the scientific literature (Brixner 1987; Weber 2002; Wojtowicz 2002; Martin 2006).

3.3 Digital imaging detectors

In x-ray imaging, there are two main approaches to information transmission with digital output:

a. Charge integrating detectors

Ionizing radiation interacts with detector material and produces charge which is collected by the readout pixels (CCD, flat panel detectors etc).

b. Photon counting detector

Ionizing radiation interacts with detector material and produce charge which is amplified and compared to an applied threshold. The readout counter will only be incremented if the incoming signal lies above that threshold.

3.3.1 Charge integrating detector

In charge integrating systems, induced charge is directly transferred to the potential well or capacitor without further processing, which means that any other currents originating from other sources like leakage current will also add to the final accumulated signal. Especially in low count rate applications, where long acquisition

times are required, the contribution of integrated noise becomes more pronounced (Tlustos 2005).

When photons (x-rays) interact with detector material, charge generated in the sensor is directly proportional to the incident photon energy which means that the contribution of the converted photons is weighted by their energy. Image contrast is generated by the absorption of photons in the object. As low energy photons have higher attenuation, they carry more information. By weighting a photon by its energy, image contrast has a weaker weight at lower energies and the Poisson noise contributions from high energy photons are enhanced. The result is a decrease in image signal to noise ratio (SNR), contrast, and the system's spatial resolution (Frallicciardi, Jakubek et al. 2009).

3.3.2 Photon counting detectors

In the case of photon counting x-ray detectors (PCXDs), induced charge is compared to a threshold. The effect of having a threshold eliminates or reduces the contribution of detector leakage current and low rate imaging can then be performed.

Since the development of Medipix1 back in 90's (Campbell. M 1990), photon counting detectors have been investigated by a number of theoretical (Niederlohner, Karg et al. 2005; Frey, X. et al. 2007; Roessl and Proksa 2007; Schmidt 2009; Taguchi, Frey et al. 2010) and experimental (Schlomka, Roessl et al. 2008; Shikhaliev 2008; Shikhaliev and Fritz 2011) studies. These studies have shown several advantages of photon counting over conventional charge integrating detectors. For instance, readout of single events, efficient rejection of electronic noise, and high signal to noise ratio, are distinctive properties. Charge integrating devices weight photons according to their energy; thus a photon with higher energy will be assigned more weight comparatively to a lower energy photon, whereas photon counting detectors allocate equal weighting factor 1 to all photons. Therefore, data collected by photon counting and charge integrating detectors represent photon beams passed through the same object differently (Shikhaliev 2005). Spectral imaging by using multiple detector thresholds appears to be a most attractive method, as it allows the material separation. This has been done by using appropriate energy ranges to identify the unique imprint of K absorption peaks for different materials.

However, PCXDs are still limited for clinical applications due to their low count rates, complex readout electronics and cross talk among neighbouring pixels. For clinical computed tomography, detector count rates depend on the application. But the required count rate is sometime claimed to be more than 10^9 counts per second per square millimetre (cps/mm^2) for the open beam (Taguchi, Srivastava et al. 2009). Barber et al (Barber, Nygard et al. 2009) claimed that the highest published maximum count rate for PCXDs is ~6×10^6 cps/mm^2 for a pixel size of 1×1 mm^2. However, the Medipix2 chip counts upwards of 10^6 cps/pixel with 55 μm^2 pixels (10^8 cps/mm^2). Certain degradation in image quality may arise (ring artefacts) due to effects associated with complex electronics in individual pixel (Anas, Lee et al. 2010). For full clinical use, detectors have to provide a high count rate by maintaining high energy resolution (which is normally affected by spread of charge cloud due to charge diffusion, charge trapping and leakage current in the detector material), small pixel size without charge sharing and fast readout speed.

A good comparison of advantages and disadvantages between charge integrating devices and Medipix photon counting pixels detectors is summarized below by (Jakubek 2007).

Charge-integrating devices	Photon counting pixel detectors
High spatial resolution (~5 μm)	Good spatial resolution (~50 μm)
Zero dead time	Non zero dead time
Not energy sensitive	Energy discrimination
Dark current	No dark current
Noise	No noise (separated by threshold)
Limited dynamic range	Unlimited dynamic range
Limited linearity	Ideal linearity (counting)

3.4 The hybrid detectors concept

The basic idea of hybrid detectors is to make a structure by sandwiching a sensor material and a pixelated Application Specific Integrated Circuit (ASIC). Each readout cell of the ASIC comprises a preamplifier shaper followed by a comparator and counter. Every pixel of sensor material is connected via a bump-bond to the corresponding pixel of the readout ASIC.

Hybrid detectors provide efficient transmission of information from sensor material to readout where several counting circuits are working in parallel. One of the most attractive feature of hybrid detectors is that both sensor material and readout ASIC can be optimised separately.

3.5 Medipix detectors

The Medipix detectors are single-photon counting detectors which convert x-rays into electron-hole pairs by the help of a semiconductor sensor layer on top of a CMOS readout chip. These detectors are referred to as hybrid detectors because they have two layers connected via bump bonds. Bump bonding is a technique to connect a single pixel of sensor material to the corresponding pixel of a readout ASIC with a bump of solder (Fujita, Matsue et al. 2011; Heikkinen, Gadda et al. 2011). The choice of sensor material is application dependent and will be discussed in detail in Chapter 4. A bias voltage is applied to the sensor to transfer charge to the readout chip.

In Medipix detectors, the sensor and readout chip usually have pixels of the same size. Thus a photon impinging on one pixel of the sensor layer will be counted by the corresponding pixel of the readout chip. Strictly speaking, as the sensor is not pixelated, its pixel size is only defined by the pitch of the metallization on the collecting side of the sensor. Further, due to the phenomenon of charge sharing, very often the photon is registered in several pixels.

3.5.1 Medipix technology from past to future

In late 1980's, physicists at European Organization for Nuclear Research (CERN) decided to tailor the photon counting devices used for high energy physics to medical applications (Campbell. M 1990). Later, the Medipix collaboration was formed to exploit the knowledge gained in the design and fabrication of hybrid pixel detectors to make a single photon counting system for x-ray imaging. University of Canterbury's focus is to contribute and share clinical benefits from spectroscopic imaging (Butler, Bell et al. 2008).

Medipix technology has opened new doors to medical imaging by counting every incident photon on the detector, giving more information regarding image with high contrast between different materials, along with high spatial resolution due to the small pixel size. Two generations of the Medipix chips have been successfully developed. The Medipix1 chip demonstrated the principle of photon counting. The performance of Medipix2 has opened new doors of medical imaging to researchers, scientists, biologists, radiologists and pathologists due to the excellent signal to noise ratio, and dynamic range and inherent properties of the photon counting method (Tlustos 2005; Llopart 2007). A third generation of detector, Medipix3 is already in use and enables several new modes of operation.

3.5.2 Medipix1

The first detector developed under the Medipix collaboration in 1998 was named as Medipix1. It had the ability to count each photon individually. It had 64 x 64 square pixels with each pixel being 170μm^2 (Campbell, Heijne et al. 1998). At the end of the 1990's 17 research institutions started a partnership to improve Medipix and this led to the development of Medipix2.

3.5.3 Medipix2

Medipix2 has 256 x 256 pixels. It was designed using 6 metal 0.25µm CMOS technology making it possible to reduce the pixel size from 170μm^2 to 55μm^2, resulting

in a detection area of 1.98 cm^2 (Llopart, Campbell et al. 2002). Medipix2 has enhanced leakage current compensation at the individual pixel level. The charge sensitive amplifier of Medipix2 was modified to accept both positive and negative polarities as input signals. Each pixel has around 500 transistors, compared to 400 per pixel in Medipix1. In Medipix1 only one threshold could be set. Events are counted only if the incoming signal lies above the applied threshold. Whereas in Medipix2, two threshold values can be set to create an energy window in which photons are counted. These threshold values are known as low threshold THL and high threshold THL (Melzer, Cook et al. 2008). Both are set as values of digital-to-analogue converters (DAC) on the chip. The THH value can be disabled by selecting THH < THL to operate in counting mode. These energy thresholds can be calibrated to correspond to the energy of an incident photon. A photo of the Medipix2 detector can be seen in Figure 3.1. Medipix2 was designed to be buttable from three of its side to increase the detection area by using an array of chips.

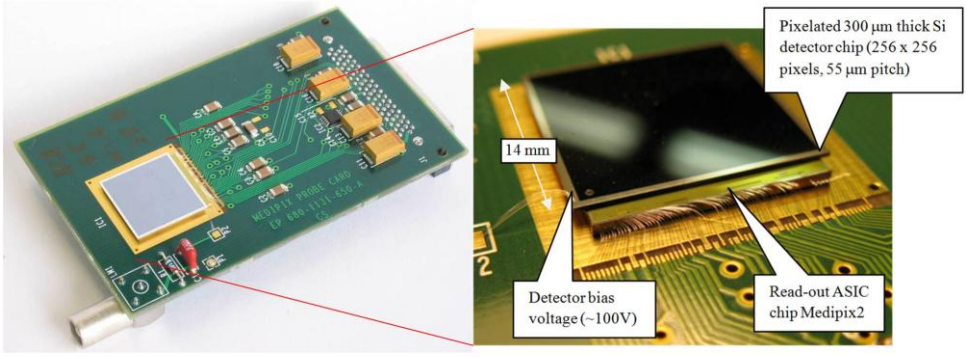

Figure 3.1 *Left:* A photo of Medipix2 detector. *Right:* Magnified view of detector from left. Top and bottom surface shows sensor layer (Si in this figure) and readout ASIC respectively. Bias voltage to the sensor material is supplied via thin wires. Retrieved from http://www.sciencemediacentre.co.nz/2009/12/16/uccern-collaboration-leads-to-colour-x-rays/

Two improved versions of Medipix2 have been released so far under the Medipix2 collaboration and are known as Medipix2-MXR (Llopart 2007) and Medipix2-Timepix (Campbell 2010). In the MXR version, temperature stability and counter depth has been upgraded from 8192 (13 bit) to 11810 while in Timepix, two new modes 'time over threshold' and 'arrival time' can be selected in addition to two modes already existing in Medipix2 'window counting' and 'THH deactivated counting'. In time over threshold mode, time for the event is recorded when the incoming signal lies above the

threshold. Arrival time mode records the time from first event to the closing of shutter (Jakubek 2009).

3.5.4 Need for Medipix3

Within the Medipix3 collaboration, the 3rd generation of the Medipix chip has been designed and tested. Medipix3 has been developed in an 8 metal 0.13µm CMOS technology. The chip has 256 × 256 pixels. Each pixel contains ~1100 transistors. Pixel dimensions are the same as Medipix2. Medipix3 chip has the capability of simultaneous measurement of 8 energy bins and a charge sharing correction (Ballabriga, Campbell et al. 2006).

When using photon counting methods with very small pixel cells (less than about 300µm-side), the phenomenon of charge sharing has to be addressed (Chmeissani and Mikulec 2001). Charge sharing occurs when the charge from a single photon is collected by two or more neighbouring pixels, each recording separate events of lower energy. Thus the overall detector counts an artificially high number of photons with an incorrect energy assignment. This produces artefacts in the acquired images by affecting the spatial and energy resolution (H. Zeller 2009).

Addressing this problem had been one of the key aims in the development of Medipix3. A method called '*Charge Summing*' has been developed in which each pixel communicates with its four neighbours to find the pixel with the highest charge for a co-incident event. The total charge is then allocated to this pixel (see Figure 3.2).

A second aim of Medipix3 is to enable full spectroscopic imaging. This has been achieved by introducing a second low threshold into each pixel enabling two energies per 55 micron pixel. In addition, groups of 4 pixels can communicate to act as a single larger (110 × 110 micron) pixel with 8 low thresholds. This spectroscopic mode is a second key requirement for spectral CT. The charge summing scheme works in both the 55 micron and 110 micron modes.

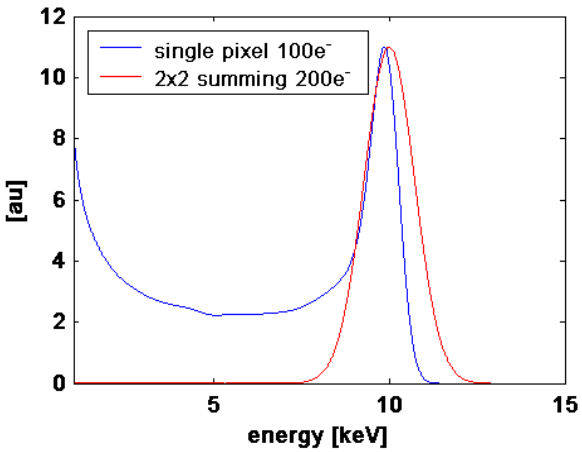

Figure 3.2 The blue line represents the spectrum observed by a single pixel of 55μm^2 which is uniformly exposed to 10 keV photons. In red is the spectrum seen by a pixel operating in charge summing mode where the output of 4 pixels are added. This is a simulation study on 300μm thick Si sensor material for a Medipix3 chip (Ballabriga, Campbell et al. 2006).

3.6 MARS multi-chip camera

The MARS multi-chip carrier board is designed and manufactured to increase the detection area by butting several chips together on a single chip carrier with a gap of few hundred microns between them. The carrier board plugs into the Gigabit Ethernet MARS readout board. The MARS camera consists of these items and a third board that controls high voltage bias and Peltier cooler. The MARS camera can support a variety of Medipix chips including Medipix2 and Medipix3. Currently, up-to six Medipix chips can be installed and read in parallel on the same chip carrier. For this thesis, I used it for single MXR-Si, dual MXR-CdTe and 3.0 quad-Si. The MARS camera has the potential to read as fast as a 50Hz frame rate. More detail can be found in a colleague's PhD thesis (Doesburg 2012).

3.7 Medipix detector in operating mode

When an x-ray interacts with semiconductor sensor material, it creates 'clouds' of electron-hole pairs in it. These clouds of charge drift towards the collection electrodes by the help of externally applied electric field and are transferred to the readout ASIC via

bump bonds. The incoming signal is then amplified by a pre-amplifier and is converted to a measurable voltage. The signal is then passed to discriminator where it is compared to a lower threshold voltage THL. If the incoming signal is found to be above THL, a counter in the digital part of the chip is incremented in this pixel. For the MXR's window mode, the photons are counted between the THL and THH. However, for our measurements, THH has been deactivated throughout. Therefore, we only had to adjust the low threshold. Figure 3.3 shows the processing of charge particles in Medipix detection system.

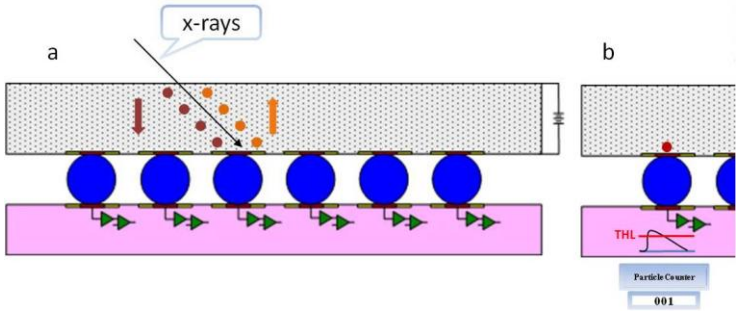

Figure 3.3 a). Creation of electron hole pairs (brown and orange dots) by x-ray interaction in Medipix detection system and (b) single pixel processing of incoming signal. The incoming signal from the sensor layer is amplified and compared with low threshold voltage (represented in red line in (b)). The counter is incremented if the signal is found to be above low energy threshold. The transmission of signal from sensor layer is operated at appropriate bias voltage.

3.8 Summary

In this chapter, the basic concept of direct and indirect detection systems and their charge propagation is briefly discussed. A comparison of advantages and disadvantages between charge integrating devices and particle counting pixels detectors is summarized. Charge integrating devices weight photons according to their energy thus photons with higher energy will be assigned more weight comparatively to lower energy photons. Whereas PCXDs compare charge to an applied threshold and allocate equal weighting factor 1 to all photons. Therefore, data collected by photon counting and charge integrating detectors represents a photon beam passed through the object differently.

The benefits of hybrid design for Medipix PCXDs have been discussed, where every pixel of sensor material is connected via bump-bond to the corresponding pixel of

the readout ASIC. Medipix detectors provide efficient transmission of information from sensor material to readout, where several counting circuits are working in parallel. But when using photon counting methods with very small pixel cells (lees than about 300µm), the phenomenon of charge sharing has to be addressed. Addressing this problem had been one of the key aims of development of the Medipix3. Our group is able to read up-to six Medipix3 chips in parallel on the same chip carrier board with a potential frame rate of 50Hz.

As discussed in section 3.5, Medipix detectors used the latest photon-counting detector technology and allocate equal weighting factor '1' to all photons. This differs from conventional x-ray detectors (charge integrating detectors), which cannot differentiate the energy of individual photons. Spectral imaging by using multiple thresholds of the Medipix detector appears to be a most attractive method, as it allows the material separation. This has been done by using appropriate energy ranges to identify unique imprints of K absorption peaks for different materials as described in section 2.4.1.

4 Characterization of Medipix2 semiconductor sensor layers (Si & CdTe)

4.1 Overview

In this chapter, we will report a summary of the observations presented in three publications in which I am a co-author (Aamir, Lansley et al. 2010; Aamir, Anderson et al. 2011; R Aamir 2011a). Medipix technology is continuously being upgraded; therefore, readout chips with different sensor layers have not yet been understood to their full extent. In this chapter, the characterization of the Medipix2 assemblies with Si and CdTe sensors using poly energetic x-ray source will be discussed. This work reports observations of inhomogeneities within the semiconductor sensors, individual pixel sensitivity responses and their saturation effects at higher photon fluxes over one hundred frames.

Before we come to Medipix2 characterization, the necessary basics of semiconductor physics will be briefly reviewed in section 4.2. In section 4.3, we will quickly go through some digital tests performed on an individual chip before its release for sensor layer characterization. Finally, results from characterization of Si and CdTe sensor layers will be presented in section 4.4.

4.2 Semiconductor physics

All materials are classified as metals, semiconductors or insulators according to their conductivity, resistivity and band structure. Figure 4.1 shows the typical range of conductivity and resistivity for the three categories.

The temperature dependence of the resistivity differs strongly for conductors and semiconductors. For conductors resistivity rises with temperature; the opposite is true for semiconductors. All semiconductor detection systems are based on same basic functions, but their performance varies due to their type. We quickly review the relevant physics of semiconductor before discussing the materials directly. The overview is mostly adopted from (Lutz 1999; Spieler 2006; Del Sordo, Abbene et al. 2009; Koenig 2011).

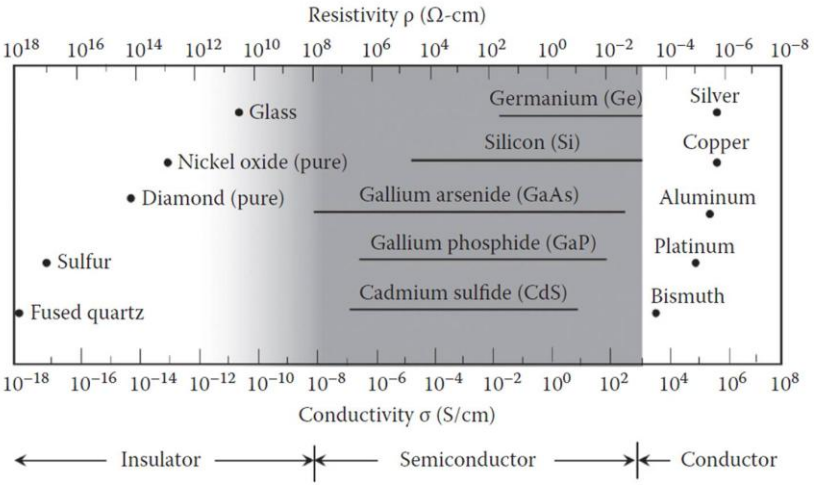

Figure 4.1 Typical range of resistivity/conductivities of insulators, semiconductors and conductors (Owens 2012).

4.2.1 Intrinsic and Extrinsic semiconductors

Semiconductors have unique properties that make them ideal candidates for detection of ionizing radiation. Intrinsic semiconductors (usually single element semiconductors) are devices that contain no impurities (in practice very few impurities). One of the biggest advantages of intrinsic semiconductors is low crystal defects due to no (or minimal) impurities. Silicon (Si) and Germanium (Ge) are the most common elements with semi-conducting properties. Conductivity of a semiconductor depends on the number of free electrons in the conduction bands and the numbers of holes in the valence bands. Higher carrier concentrations results in higher conductivity. The charge carrier densities for electron 'n' and holes 'p' can be calculated as

$$n = 2\left(m_n^* k_B T / 2\pi\hbar^2\right)^{3/2} e^{-(E_C - E_F)/k_B T} \qquad (4.1)$$

$$p = 2\left(m_p^* k_B T / 2\pi\hbar^2\right)^{3/2} e^{(E_V - E_F)/k_B T} \qquad (4.2)$$

Here, m_n^* and m_p^* denotes electron and proton effective masses respectively, k_B denotes Boltzmann constant, T the temperature, E_C the energy at the bottom of the conduction band (minimum energy), E_F the Fermi energy level and E_V the energy at the top of the valence band (maximum energy).

In intrinsic semiconductors, the electron and hole carrier densities in the conduction and valence band respectively are equal ($n = p$). The thermal excitation of an electron from the valence band to the conduction band yields both a hole in the valence band and a free electron in the conduction band and hence has very low conductivity.

The highly developed technology of '*band gap engineering*' for extrinsic semiconductors (also known as compound semiconductors) has opened up new possibilities to control the width, E_G, of the band gap.

$$E_G = E_C - E_V \qquad (4.3)$$

This can be altered by adding a tiny fraction of foreign atom into a uniform crystal structure by a process known as *doping*, during crystal growth or later, in a specific crystal region (one atom per 10^8 semiconductor atoms). In this way, it is possible to change the conduction type and create *n-type* (with excess electrons) or *p-type* (with excess holes) materials. The replacement of a host crystal atom by a foreign atom not only introduces extra energy levels in the band gap, but also shifts Fermi energy levels close to one or other band edge (conduction or valence band). If donor energy levels (E_D) are close to the conduction band (E_C), ($E_C - E_D$) becomes smaller and the Fermi level may move closer to the bottom of the conduction band at room temperature. Similarly, if acceptor energy level (E_A) is close to valence band, ($E_A - E_V$) becomes small and the Fermi level moves towards the top of the valence band (Lutz 1999).

Among several compound semiconductors, CdTe and CdZnTe are considered as attractive materials for clinical imaging due to their high atomic number, high density, wide band gap, high detection efficiency and good room temperature performance. In our experiments, we will limit our discussion to Si and CdTe semiconductor materials.

4.2.2 Depletion region and reverse biased operation

A p-n junction diode is created by joining opposite doped (p-type and n-type) extrinsic semiconductors. Once the bodies are brought into contact, electrons from the n-type material diffuse into the p-type and holes from p-type material diffuse into the n-type material. Consequently a surplus will be created of negative charge in the p region and of positive charges in the n region. This creates an electric field that stops further diffusion of charges; the region under this field is known as a '*depletion region'*. As a result, every diode starts off with a non-zero potential difference between the p and n type materials and a built-in potential (V_{bi}) has to be considered. By applying an external field, the width of the depletion region can be reduced or extended. The basic idea of the ionizing radiation detectors is to extend the depletion region to the full detector thickness. This has been achieved by reverse biasing the diode and applying an external bias voltage (V_b) in the same polarity as 'V_{bi}'. A reverse bias voltage yields the depletion width demonstrated by Spieler (Spieler 2006).

$$w_d = \sqrt{2\varepsilon(V_b + V_{bi})/Ne} \qquad (4.4)$$

Here N is the number of charge carriers depends on dopant concentration and ε is the dielectric constant that depends on the type of material (11.9 ε_o for Si). The typical V_{bi} in detector diodes is about 0.5V. When the depletion width is less than the detector thickness, the diode is '*partially depleted'.* When w_d extends to the full detector thickness, the diode is *'fully depleted'*.

Ideally, in fully depleted region, all mobile charge carriers should be removed from the junction, so no current can flow. However, thermal excitation can promote electrons across the bandgap and results in current flow even in the absence of radiation. This is known as *'dark current'* or *'leakage current'* and may increase with the presence of impurities in the lattice, as they introduce intermediate energy states in the bandgap. The Medipix detectors have the capability to eliminate or reduce the contribution of detector leakage current by the application of low threshold values (see section 3.5.3).

4.2.3 Carrier transport and charge collection efficiency

The charge transport properties of a semiconductor are one of the key parameters in the development of radiation detectors. As the charge carriers move through medium, they scatter and after a very short time (of order ps in Si), carrier transport becomes non-ballistic and their velocity doesn't depend on the duration of acceleration, but only on the magnitude of the local electric field, i.e.,

$$v(x) = -\mu E(x) \qquad (4.5)$$

Here μ is the proportionality constant known as carrier mobility. Eq (4.5) shows that the velocity of charge carriers at point x depends only on the electric field at that region, irrespective of where they originated and how long they have moved (the negative sign changes to positive for holes).

The second important quantity τ is known as the mean life time of the charge carrier and can be determined from mean drift length λ, i.e.,

$$\lambda = \mu\tau E(x) \qquad (4.6)$$

Here, λ depends on $\mu\tau$, which is called the mobility life time product or simply $\mu\tau$-product. Small $\mu\tau$-products result in short drift lengths of electrons ($\lambda_e = \mu_e\tau_e E$) and holes ($\lambda_e = \mu_h\tau_h E$), which limits the maximum thickness and energy range of the detector. Compound semiconductors (for example CdTe, CdZnTe and GaAs) generally have poor carrier transport properties due to charge trapping. The main causes of charge trapping are impurities, structural defects (due to intermediate energy levels) or irregularities (dislocations, inclusions). But more importantly, compound semiconductors are suitable for almost any application due to their wide range of physical properties i.e., band gap, atomic number and density etc. Some physical properties including those of electrons and holes for elemental semiconductor (Si) and compound semiconductor (CdTe) are shown in Table 4.1.

.

Table 4.1 Physical properties of semiconductor materials at 25°C (Del Sordo, Abbene et al. 2009).

Material	Si	CdTe
Crystal structure	Cubic	Cubic (ZB)
Atomic number	14	48, 52
Density (g/cm^3)	2.33	6.20
Band gap (eV)	1.12	1.44
Pair creation energy (eV)	3.62	4.43
Resistivity (Ω cm)	10^4	10^9
$\mu_e\tau_e$ (cm^2/V)	> 1	10^{-3}
$\mu_h\tau_h$ (cm^2/V)	~ 1	10^{-4}

4.2.4 Drift and diffusion

Semiconductors are electrically neutral in the absence of external voltage. In this section, we will consider the phenomenon that occurs after the generation of charges (see 2.4) in the semiconductor under the influence of an externally applied bias voltage. The charge cloud generated in the semiconductor sensor layer is separated through the application of an externally applied electric field and moves towards the collection electrodes by drift. Diffusion is caused by a gradient in charge carrier concentration (distribution of charges from higher concentration to lower concentrated regions) and affects the size of the charge cloud. So, charges in the sensor move towards the contact between sensor layer and the readout chip with the drift velocity and in the meanwhile, the charge cloud spreads across the sensor region due to diffusion. Due to this effect charge sharing occurs among pixels in the sensor layer leads a low energy tail in the detected spectrum.

Following Spieler (Spieler 2006), the diffusion that occurs perpendicular to the drift direction can be calculated as

$$\sigma = \sqrt{2Dt} \qquad (4.7)$$

Here σ is lateral diffusion, *t* represents drift time and *D* is the diffusion constant. According to the Einstein relation

$$D = \frac{k_B T}{e} \tag{4.8}$$

Here 'k_B' is the Boltzmann constant, 'T' the temperature and 'e' is the elementary charge

Also, drift time t is inversely proportional to the electric field 'E'

$$t = \frac{d}{E} \tag{4.9}$$

Similarly for a uniform electric field,

$$E = \frac{V}{d} \tag{4.10}$$

So, by combining Eq (4.9) and Eq (4.10), we can write

$$t = \frac{d^2}{V} \tag{4.11}$$

Here 'd' is the drift length. Now by putting values of 'D' and 't' in Eq (4.7), diffusion length can be expressed in terms of drift length and bias voltage. i.e,

$$\sigma = d\sqrt{\frac{2k_B \mathrm{T}}{eV}} \tag{4.12}$$

This means that when the detector bias voltage 'V' is increased, it increases the drift speed of the charges due to the stronger electric field, and at the same time diffusion of charges is reduced. The diffusion is independent of charge mobility 'μ' and thus same for both electrons and holes. For the CdTe detector (discussed later in section 4.4), d = 1mm, T = 298K (room temperature) and V = 350V; lateral diffusion is calculated as σ ≈ 12μm while for V = 200V, lateral diffusion is increased to about σ ≈ 16μm. The distance of the generated charge cloud from the top of the sensor layer is another factor in charge sharing. This distance is energy dependent. Lower energy photons tend to be stopped

nearer the top surface, and therefore their charge clouds travel further, so experience more lateral diffusion.

4.3 Digital characterization

Due to the electronics in Medipix ASICs, these chips are not ideal detectors. It is normal to have zero response from several pixels, but it is important to determine which pixel has non-functional electronics and which one has sensor layer issues. This section will provide a quick overview of various digital tests performed on individual chip before its release for sensor layer characterization or any MARS CT application. Overall, all chips are carefully tested to check their readout performance, quality of the detector, bump-bonding and the response to x-rays.

A series of tests via Matlab™ routines have been designed to assess the electronic response of every Medipix2 ASIC employed by the MARS group. Four Medipix2 chips (Si MXR, dual CdTe MXR & single CdTe Timepix) were tested by the author and found working. Most images obtained under this procedure were similar; therefore, results from the Si Medipix2-MXR will be presented.

4.3.1 Digital response test

The Medipix2 chip has various voltage and current levels to bias the front end (CSA and discriminators) that can be set by means of digital to analogue converters (DACs) (Llopart 2007). The digital response of pixels is tested by dividing them into two categories: good pixels which read 1; and bad pixels which don't read. The non-functioning pixels or "digitally dead" pixels are shown as black. It is common to have a few dead pixels scattered across the detector which are mostly due to the non-functional electronics of an individual pixel; read out issue; bad bump bond connections, or it could be due to surface damage of the sensor layer. The first two reasons belong to the ASIC (electronic readout) and the latter two belong to sensor layer. Figure 4.2 shows the digital response of the ASIC of a Si assembled Medipix2-MXR chip. No pixel is observed to be digitally dead.

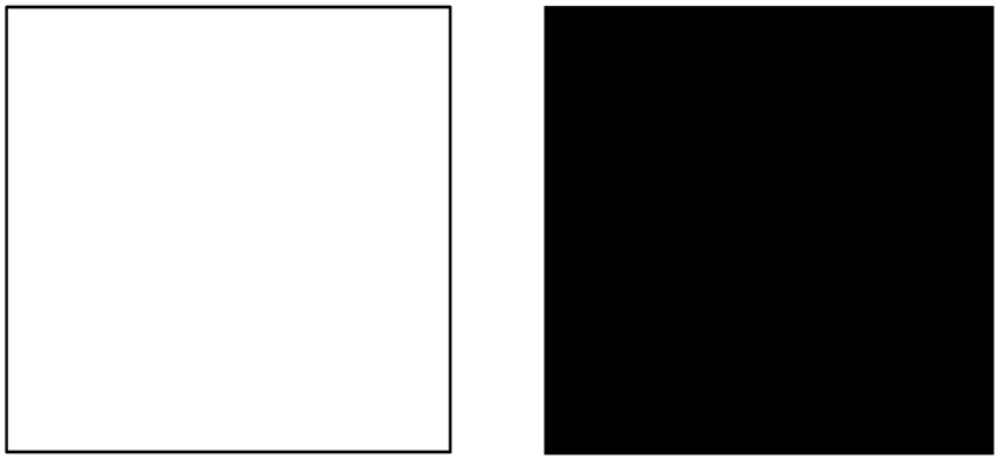

Figure 4.2 *Left*: An image of Si Medipix2-MXR by masking all ASIC pixels to read 1. Digitally dead pixels are shown as black (0). No pixel is observed to be digitally dead. *Right:* Same chip now reading 0.

4.3.2 Noise edge detection

A noise edge scan means to scan through the THL (see section 3.5.3) range and note threshold variations across the ASIC matrix i.e., the THL values for each pixels start counting. Without input particles (no visible, UV light, x-rays or test pulse input), each pixel starts counting when it enters into the electronic noise. Electronic noise is a random fluctuation of electrical signal due to different electronic components in the readout. The noise edge detection is useful for determining noise level in the chip and later can be used for equalizing each pixel's response.

For this calibration test, the high energy threshold (THH) was disabled (THH = 0), and the low energy threshold (THL) was scanned through the entire range. The detector recorded the charge "above" each THL value. By doing so, the most sensitive pixel will count first while the least sensitive will detect noise at the end and produces an approximately Gaussian curve. Figure 4.3 shows the Gaussian peak at the noise floor determined at THL ≈ 745 for a Si Medipix2-MXR. The noise edge can be affected by bright light and by DAC values.

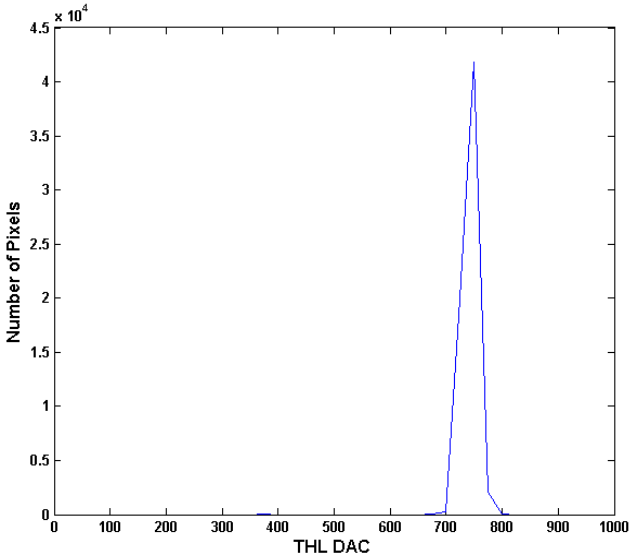

Figure 4.3 A peak at the noise floor. The typical noise floor for Silicon MXR is at THL of 650, but this varies +/-200 from chip to chip. It also rises if the chip is in bright light.

4.3.3 Entire matrix readout test

The goal is to check the readout capability of entire matrix by using MARS readout software: that both the rows and columns are being read and processed in the correct order. This has been done by switching off half the chip (half the rows off) and then takes a digital image. To do this, first the THL is shifted in to the middle of noise, i.e. approximately the centre of the noise (THL ≈ 745) as shown in Figure 4.3. We then make a mask with half zeros (off pixels) and half ones (on pixels).

The top half of the frame should be mostly noisy because it is measuring electronic noise. The bottom half of the frame should always be black because these pixels are switched off as shown in Figure 4.4. The same masking technique also been applied diagonally and can be seen in Figure 4.5.

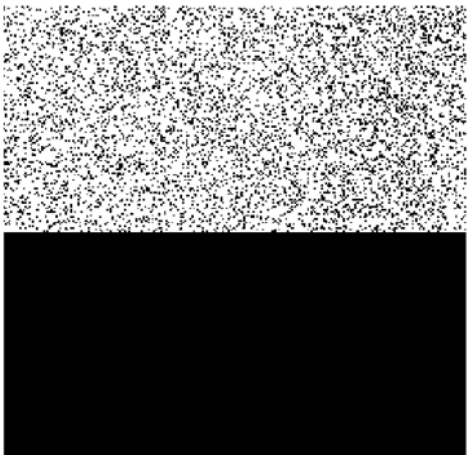

Figure 4.4 A digital image made by switching off the half chip (bottom rows) and half the chip measuring noise (top rows).

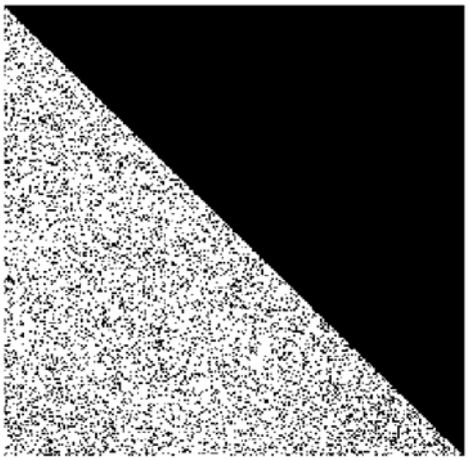

Figure 4.5 A digital image made by switching off half the chip (diagonally) and half the chip measuring noise.

4.3.4 Threshold equalization

Due to the variation in electronic performance of each pixel, the responses of individual pixels need to be equalized. Equalization minimizes the spread of the threshold distribution over the detection area. Threshold equalization is an ongoing topic of research which is outside the scope of this work but due to its relevancy here, we will discuss it briefly.

To find the correct settings of each pixel, the first step is to optimise the threshold adjustment DAC (THS). The THS value is a global value of the threshold, common to all pixels in the chip. This is achieved by using a dedicated 8-bit THS across the matrix which determines the maximal offset to the unadjusted threshold position. In the individual pixel, this offset is scaled by the 3-bit fine tuning DAC. For each THS value, each pixel's 3-bit current DAC is set to 000 (low) and to 111 (high). The algorithm then measures the distance between the two noise floors and chooses the THS for which the overlap is optimal. More detailed consideration of threshold equalization can be found in the scientific literature (Pfeiffer 2004; Tlustos, Ballabriga et al. 2006; Melzer, Cook et al. 2008; Koenig, M Zuber et al. 2011).

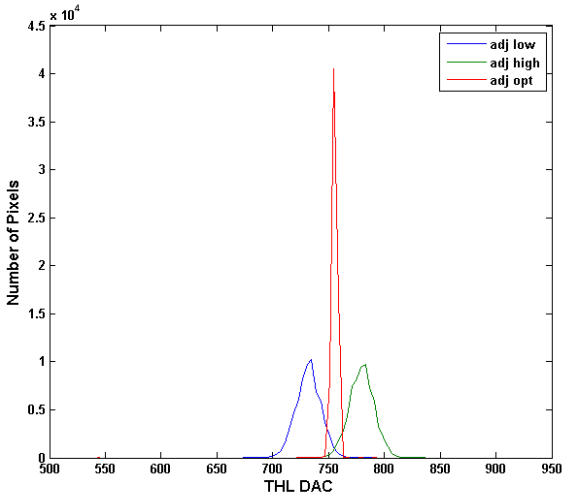

Figure 4.6 Si assembled Medipix2-MXR threshold adjustment. The blue distribution corresponds to the equalization DAC bits set to low (000) for all pixels and green shows high bits setting (111), both before the threshold adjustment. The narrow distribution in the middle (red) is the result of fine tuning the equalization DACs.

4.3.5 Energy calibration

The author used a number of ways to measure the conversion of THL (DAC) values to energy (keV), while keeping the detector inside the scanner. One needs to be identify known points from different spectra. The most common method is to measure the photo-electric peak of gamma-emitters in the range between 5 keV to 100 keV with reasonable half life. ^{241}Am with a photoelectric peak of 59.6 keV is a preferable radiation source for this purpose. Another technique uses monoenergetic fluorescence radiation of

different metal foils when they irradiated by x-rays, molybdenum ($K\alpha_1$ = 17.18 keV), gadolinium ($K\alpha_1$ = 43 keV) and gold ($K\alpha_1$ = 81 keV). Other high Z elements can be used depending upon the detection efficiency (discussed in section 4.4) of the detector. A third method was used (Raja Panta's unpublished data) to increment THL for different tube voltages. The idea is to determine the THL value at which the detector elements stop counting for a particular tube voltage, as there should be no photons above any kVp value. However, due to charge sharing and pulse pileup, blurring of the highest possible energy is observed (Frey, X. et al. 2007). While writing this, a detailed study comparing the three methods is being done by several of the MARS group members, led by Dr. Stephen Bell.

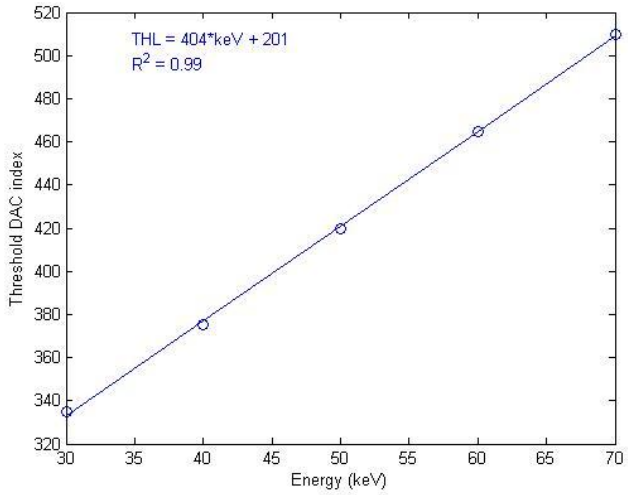

Figure 4.7 Linearity of the response between THL (DAC) and energy by tube voltage adjustment method for a single CdTe Medipix2-MXR detector.

4.4 Characterization of semiconductor sensor layer (Si & CdTe)

An understanding of the detection characteristics of the sensor layers is vital to high-quality imaging. Here we will discuss the inhomogeneities within the sensors; individual pixel sensitivity response; and their saturation effects at higher photon fluxes over one hundred frames.

The choice of semiconductor material as a sensor layer depends upon the absorption probability required by the user. Silicon (Si) is traditionally used due to the availability of good quality homogeneous material, and high transport properties of the charge carriers (the mobility-lifetime product is around 1 cm^2/V) which leads to excellent energy resolution (see Table 4.1). However, due to its low atomic number (Z = 14), the detection efficiency of Si is low at higher energies. Detection efficiency (sometimes referred to as absorption probability or as stopping power) is the energy loss of the particle per unit path length (eV/cm). CdTe (Z = 48, 52) offers high detection efficiency in the diagnostic energy range (10 keV to 150 keV). The detection efficiency for a 300-µm-thick Si sensor is less than 10 % at energies above 30 keV. Whereas, 1-mm-thick CdTe offers absorption probabilities of more than 60% at energies up-to 107 keV as shown in Figure 4.8.

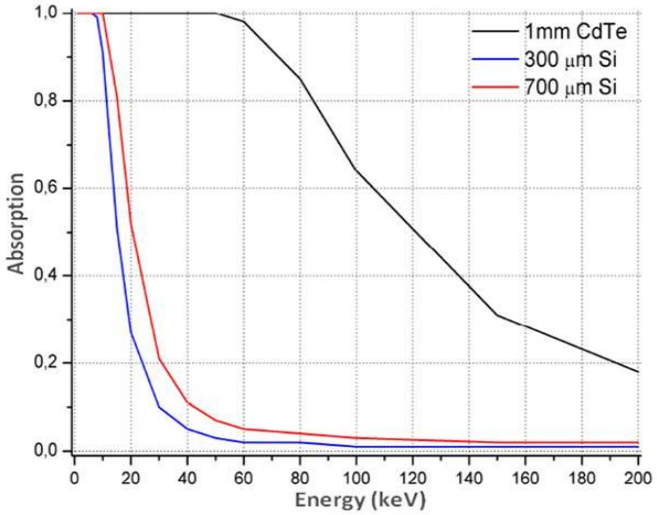

Figure 4.8 Photon absorption probability of 1-mm-thick CdTe and 300-µm-thick Si sensor material as a function of energy (Greiffenberg 2011).

In these experiments, we use 1-mm-thick dual CdTe and 300-µm-thick single Si sensors bump-bonded to individual Medipix2 MXR readout chips. The silicon material was produced by Canberra and bump-bonded at VTT, Sweden; Si material is commonly grown by the Czochralski method (Abrosimov, Rossolenko et al. 1997). Acrorad, Japan, made the CdTe sensors, which were bump-bonded at FMF, Germany; the temperature was kept below 130°C to maintain good sensor properties. The CdTe material was grown

by the Travelling Heater Method (THM) (Acrorad ; Shiraki, Funaki et al. 2007; Shiraki, Funaki et al. 2010)

The bias voltage applied to the sensor was −438 V for CdTe and +100 V for Si. One hundred open-beam images were acquired (i.e. without an attenuating specimen between the x-ray source and the detector) using the MARS-CT scanner system. The detectors were flood irradiated using a 1.8-mm-Al-filtered poly-energetic x-ray source with a W target, Source-Ray SB-80-1K. The tube was operated at 80 kVp with a tube current of 200 µA; the focal spot of the x-rays was ~45 µm. The source to detector distance was ~190 mm. The low threshold was set to 13 keV and the exposure time was 25 ms. The total scanning time was less than a minute, over which time, the x-ray output is found to be stable. The readout was done using the MARS readout system. Before the measurements, threshold equalization with respect to the noise edge, and energy calibration of the detectors, was performed using customized software.

4.5 Results

4.5.1 Flood frames

In order to measure the uniformity of Si and CdTe sensors, one hundred flood images were obtained using the parameters previously described. The mean count rate of the detectors was 117.85 ± 22.13 and 1056 ± 81.43 counts/pixel respectively across the hundred frames. A region with increased sensitivity was observed at the edges of the two CdTe detectors, as shown in Figure 4.9 (b). High counts at the detector edges could be due to a volume effect, where the distance between the outermost pixel bump bonds and the edge of the sensor is greater than the pixel pitch (metallization of collecting side of sensor). Complete / partial rings of pixels with higher photon counts were observed around small areas of low sensitivity pixels. This could be due to lateral diffusion of charge, especially in those regions where conduction through the sensor is less then normal. A network of arbitrary lines across whole CdTe sensor with increased count rate to a few % can also be seen in Figure 4.9 (b). We refer to them as "*wrinkle pattern*". By the time of reporting these results, the crystal structure of CdTe was not fully identified however, Buis (Buis, Gros d'aillon et al. 2011) investigated these microstructural defects

in CdTe crystal and reported similar findings in the flood images. Small grain boundary angles / dislocation of grain boundaries could be the major cause of this texture. There were clusters / blobs of pixels with low / zero response shown by blue color map. These irregularities could be attributed to tellurium inclusions within the sensor material and are assumed to be one of the major causes of charge trapping. Ruat (Ruat and Ponchut 2011) indicated that these defects are high leakage current sources. Another reason could be due to bad connection between the CdTe sensor layer and the Medipix chip. ie., failure of the bump bonds, suspected for zero responsive pixels.

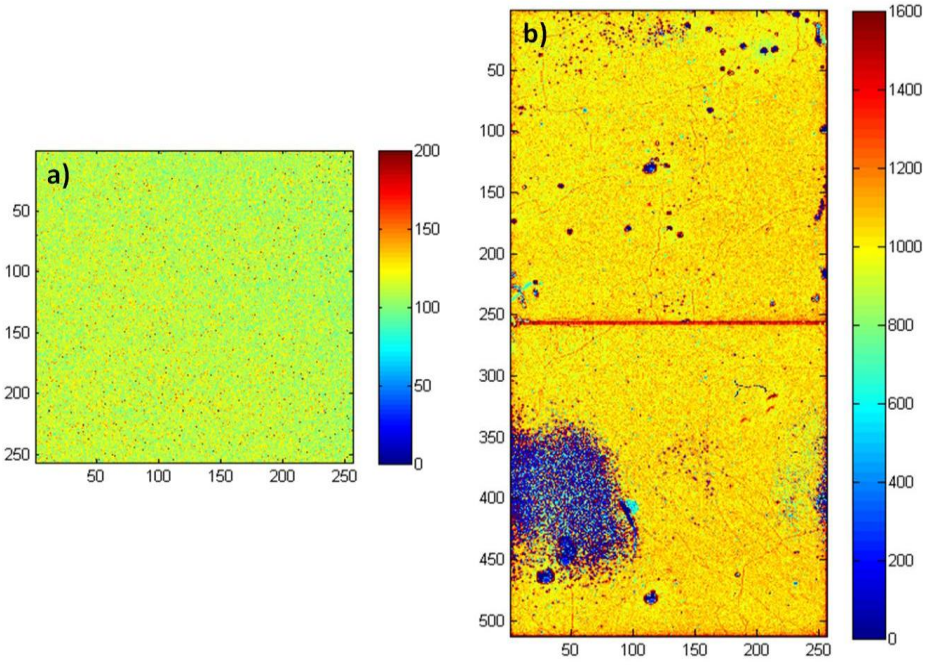

Figure 4.9 Mean of one hundred frames of (a) Si sensor and (b) CdTe sensor. The color map shows the mean count of all pixels across the hundred frames.

When comparing the CdTe sensors with the Si sensor, none of the previously discussed inhomogeneities are observed (see Figure 4.9 (a)) but individually several pixels give more sensitive response and some are observed as less sensitive. About 0.02 % pixels in Si and about 0.7 % pixels in dual CdTe are observed as zero sensitive (dead pixels).

4.5.2 Individual pixel sensitivity

To clearly demonstrate differences in the sensitivity response, pixels have been divided into three categories: high sensitivity pixels (HSPs), with counts ≥ 110% of median counts across the one hundred frames; low sensitivity pixels (LSPs), with counts ≤ 90% of the median, and average or normal pixels, with counts between 90% and 110% of the median. Figure 4.10 shows all pixels by masking them according to these three categories.

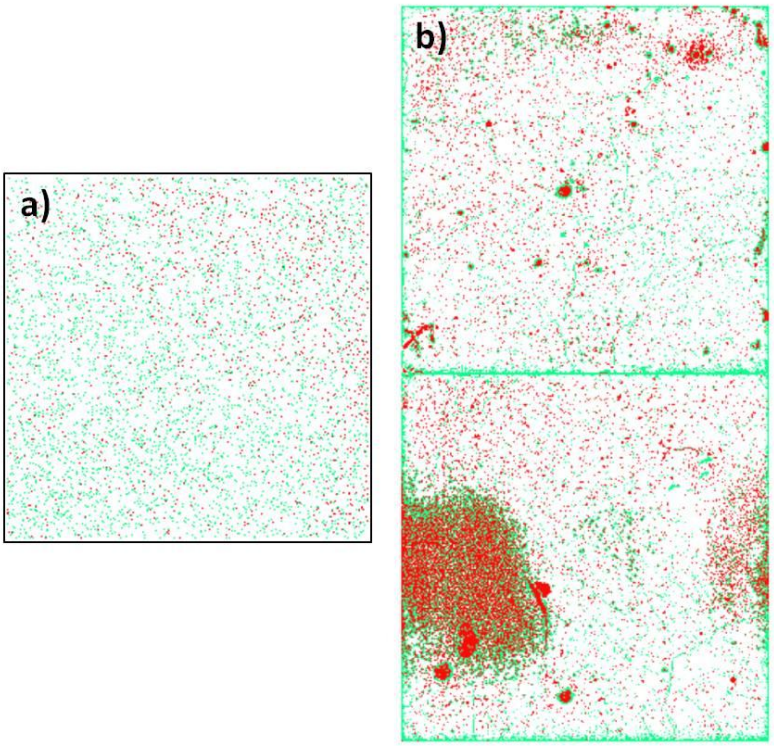

Figure 4.10 Normal, high and low sensitive pixels are shown by white, green and red regions respectively for (a) Si and (b) CdTe sensor. The inhomogeneities across CdTe detector are more prominent.

Also, according to the previously defined sensitivity criteria, the ratio of measured noise to Poisson noise (expected noise) of Si and CdTe sensor layer for normal pixels, HSPs and LSPs is shown in Figure 4.11 and Figure 4.12 respectively. For a purely Poisson distribution with no additional noise, the standard deviation is the square root of the number of counts. All three categories of the pixels of Si measure the photon beam

with Poisson-distributed counts. Whereas for CdTe, the ratio decreased to 90% for HSPs but LSPs are close to poisson distribution but some of them are noisier.

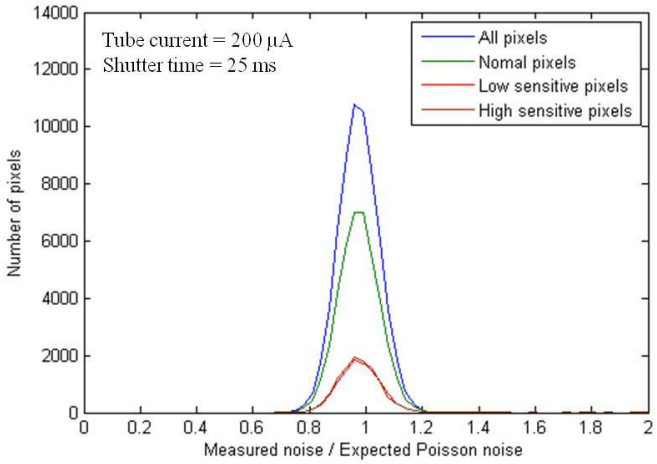

Figure 4.11 Ratio of measured noise to expected noise of Si sensor layer for normal, HSPs and LSPs. Here blue line shows the combine response of all pixels (which includes normal and sensitive pixels). All three categories of pixels in Si measure the photon beam with Poisson-distributed counts.

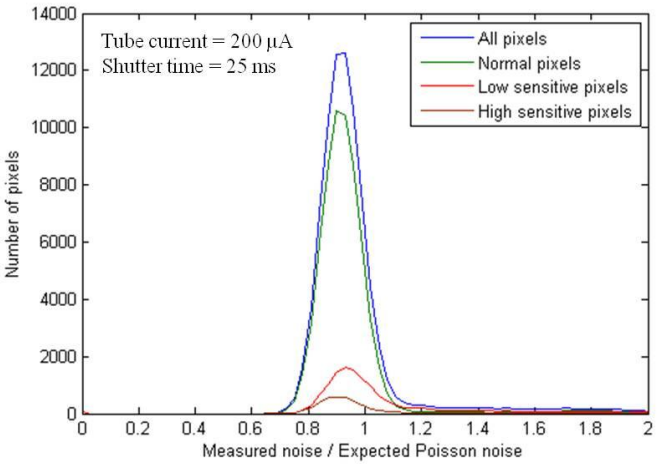

Figure 4.12 Ratio of measured noise to expected noise of CdTe sensor layer for normal, HSPs and LSPs. Here blue line shows the combine response of all pixels (which includes normal and sensitive pixels). Most of the LSPs are close to Poisson distribution but some of them are noisier (see width of histogram) due to low photon count detection by these pixels, whereas, the ratio decreased to 90% for HSPs. The reason for this response will be discussed in a later section.

4.5.3 Pixel sensitivity response of neighbouring pixel

Using the same one hundred flood exposures, several rows and columns of pixels have been analyzed across all frames to understand the sensitivity response of an individual pixel with respect to its neighbouring pixel. Figure 4.13 and Figure 4.14 show the profile of 256 pixels of Si and 512 pixels of CdTe from column 105 (highlighted by red line in inner window) across one hundred frames respectively.

From Figure 4.13, the quasi-periodic oscillations in counts of the Si detector are observed around the 4 pixels (220 µm) scale whereas for CdTe (see Figure 4.14), it is around 6 pixels (330 µm). Pixels from column 105 of CdTe go through a zero counting pixels at rows 7 and 249 but LSPs near rows 356 and 431 do not have a zero counting pixel nearby. Overall both detectors show a high degree of repeatability across one hundred frames which is considered as one of the key requirement for CT imaging.

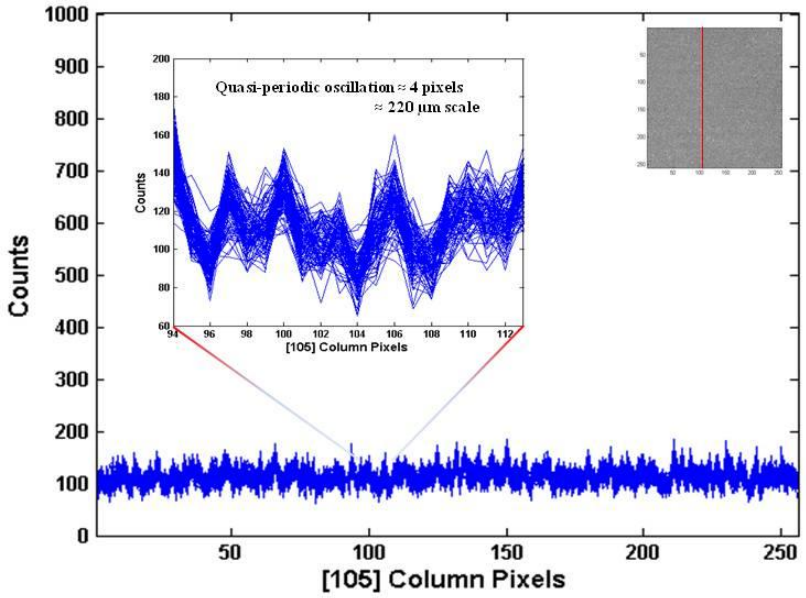

Figure 4.13 Profile of 256 pixels of column 105, with 100 exposures superimposed. Inner window shows zoom in view of a few pixels. Each line indicates the measured counts for individual pixel in a single frame.

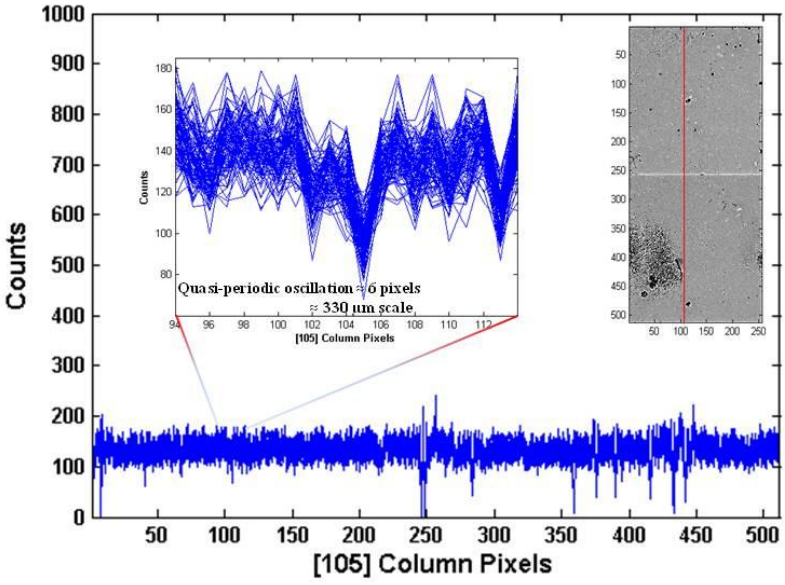

Figure 4.14 Profile of 512 pixels of column 105, with 100 exposures superimposed. Inner window shows zoom in view of a few pixels. Each line indicates the measured counts for individual pixels in a single frame.

4.5.4 Saturation effect

When a detector is unable to identify individual incoming pulses due to the near coincidence of pulses (under high flux) then the phenomena refers as saturation effect. This means that the analogue circuits in the pixels are going faster than the digital counters. To analyze this response for both detectors, a series of a hundred flood images were acquired at different x-ray tube currents by keeping the shutter time constant and then at different shutter times by keeping x-ray tube current constant. All other parameters were kept the same but because stopping power of Si is less than CdTe, count rates are lower.

As a simple test, the mean count of all pixels across 100 frames is plotted for Si and CdTe sensor layers in Figure 4.15 and Figure 4.16 respectively. The linear fitted lines indicate no saturation in Si detector for both conditions (see Figure 4.15). However, a saturation of the CdTe detector has been observed with increasing tube currents (Figure 4.16).

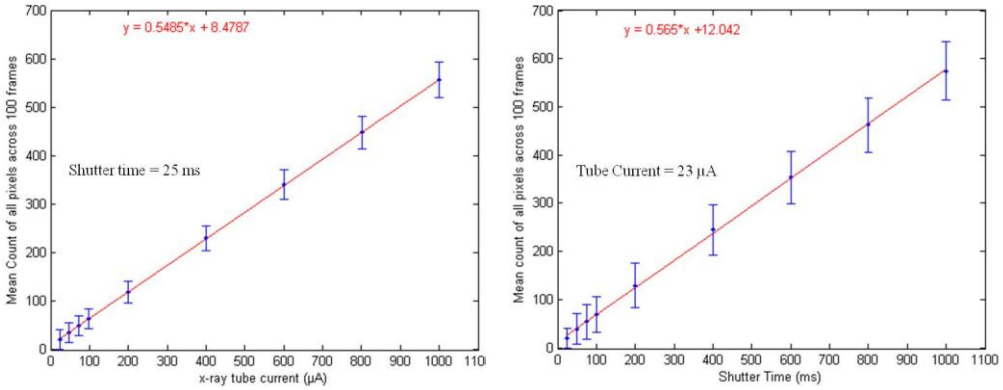

Figure 4.15 Saturation analysis of Si detector. *Left:* Mean count of all pixels across 100 frames as a function of tube current by keeping shutter time constant at 25ms. *Right:* Mean count as a function of shutter time at fixed tube current 23 μA. The linear response indicates no saturation in both conditions.

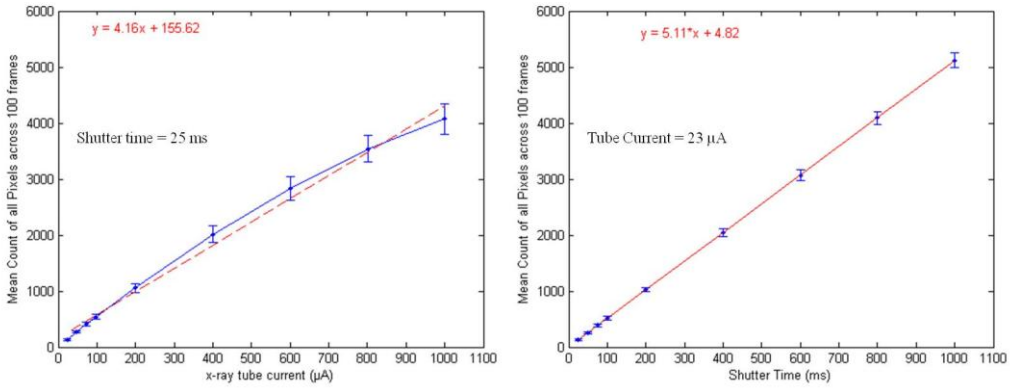

Figure 4.16 Saturation analysis of CdTe detector *Left:* Mean count of all pixels across 100 frames as a function of tube current by keeping shutter time constant at 25ms. *Right:* Mean count as a function of shutter time at fixed tube current 23 μA. A saturation of the CdTe detector can be seen at higher tube currents however, detector behaves linearly with increasing shutter time.

To demonstrate individual pixel response over one hundred frames, variance of each pixel count is plotted as a function of mean count of that pixel. Because for a purely Poisson distribution and with no additional noise, the variance of the pixel count equals the mean count of that pixel.

Figure 4.17 and Figure 4.18 demonstrate the saturation analysis of each pixel of Si detector, at higher x-ray flux. A diagonal line is superimposed to demonstrate the Poisson distribution trend of pixels. At higher shutter time, no saturation of pixels is seen (Figure 4.17). However, it was observed that at higher tube current, only a few pixels of Si detector (~ 0.4%) were saturating (pixels under trend line), as shown in Figure 4.18.

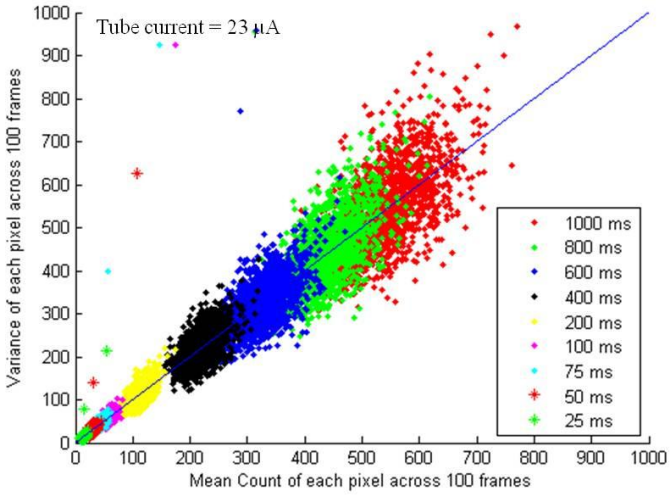

Figure 4.17 Response of Si detector with increasing shutter time and constant tube current. Each dot represents an individual pixel at specific shutter time. Almost all pixels follow the trend line (diagonal line) for Poisson distribution.

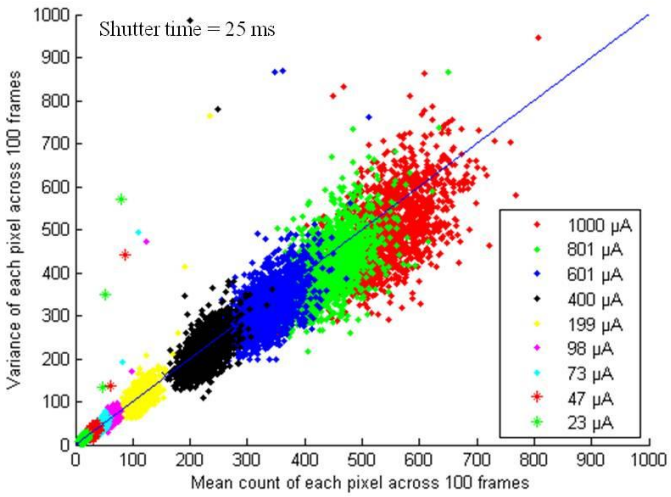

Figure 4.18 Saturation effect of Si detector with increasing tube current and constant shutter time. Most of the pixels follow trend line but some pixels (< 0.1%) show saturation at higher tube currents.

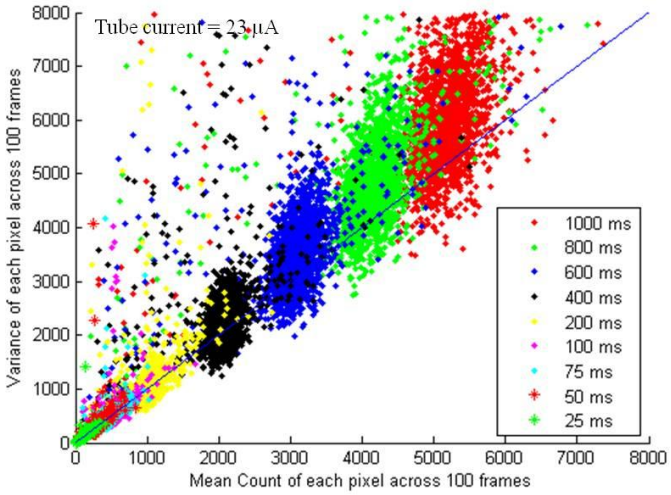

Figure 4.19 Response of CdTe detector at 23 µA with increasing shutter time. Each dot represents an individual pixel at specific shutter time.

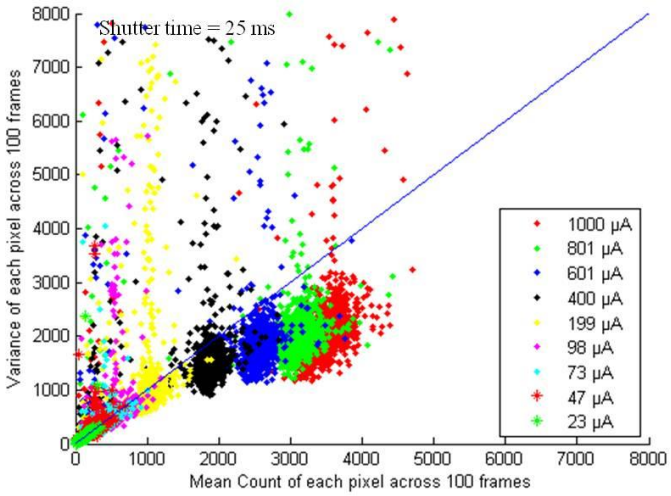

Figure 4.20 Saturation effect of CdTe detector with increasing tube current and constant shutter time. Each dot represents an individual pixel at specific tube current. A clear saturation of pixels from CdTe detector is observed after 200 µA (yellow color map).

Figure 4.19 and Figure 4.20 indicate the response of CdTe detector, at higher shutter time and tube current respectively. For CdTe, most of the pixels were saturating for tube currents beyond 200 µA, as shown in Figure 4.20. The reason for saturation of the sensors at high photon fluxes could be due to sensor pulse pileup. A pulse is only counted as a photon if the pulse is above our applied threshold of 13 keV, but with charge sharing, many pulses below threshold can combine to give a pulse over 13 keV. Another direct explanation could be the effect of charge sharing, which results in higher deviations of the count-rates between the pixels. As the charge sharing is dominated by diffusion, and the diffusion time is proportional to the drift length^2 divided by the bias voltage (see section 4.2.4). But it is evident that both reasons co-relates with each other.

While comparing the saturation results from both detectors, it is observed that at higher shutter times, there is almost no saturation in Si counts (see Figure 4.21) but the ratio of measured noise to expected noise increase upto 10 % for CdTe (Figure 4.23). The reason for increase in measured noise is found to be readout counter limit due to 'race conditions' in MXR chips. It happens when two or more photons arrive within the same detector region in the same integration time (dead time) of the readout then these quasi-coincident photons results in false count (equal to counter limit i.e., 11810 counts) (private communication with Lucas Tlustoos in 2010). Figure 4.22 and Figure 4.24 show that at the lower tube currents, the detector measures the photon beam with Poisson-distributed counts. As the photon flux (tube current) is increased, the ratio of measured noise to expected noise decreases to 95 % for Si and 70 % for the CdTe detector respectively.

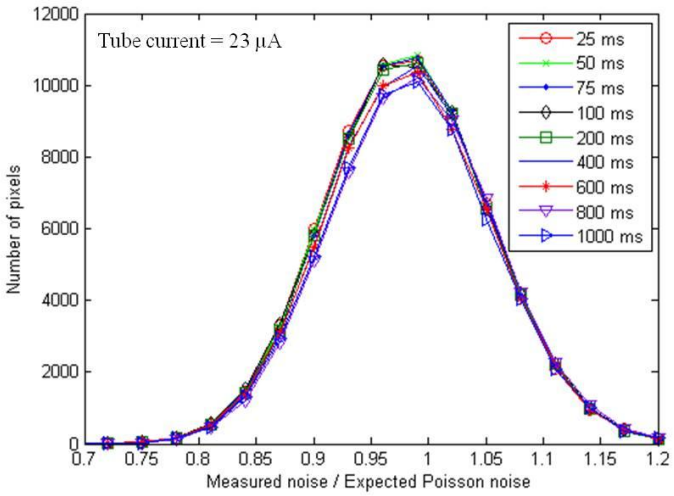

Figure 4.21 Ratio of measured noise to expected noise of Si detector. The ratio is almost 100% which means no saturation of sensor.

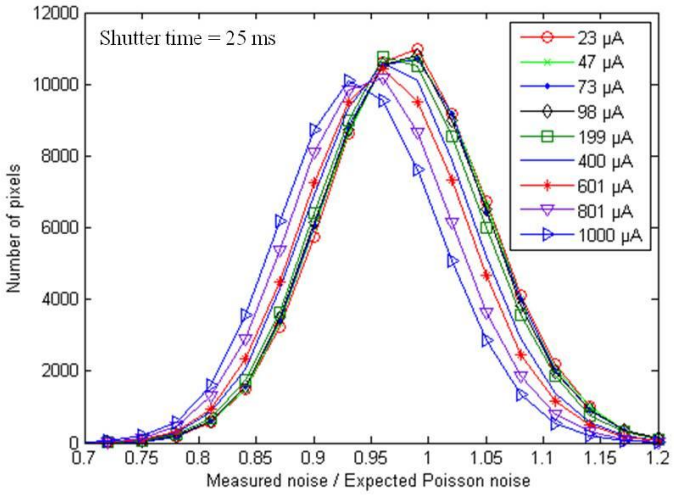

Figure 4.22 Ratio of measured noise to expected noise of Si detector. The ratio decreases slightly to around 95 % with increasing tube current.

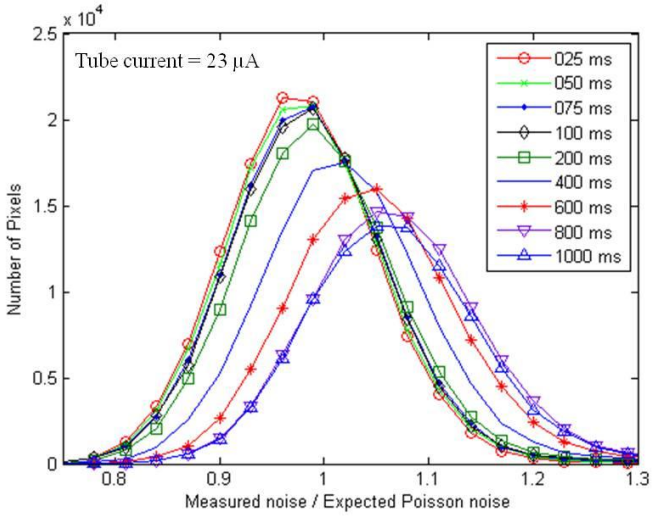

Figure 4.23 Ratio of measured noise to expected noise. The ratio increases with increasing shutter time, to 110 % due to counter saturation.

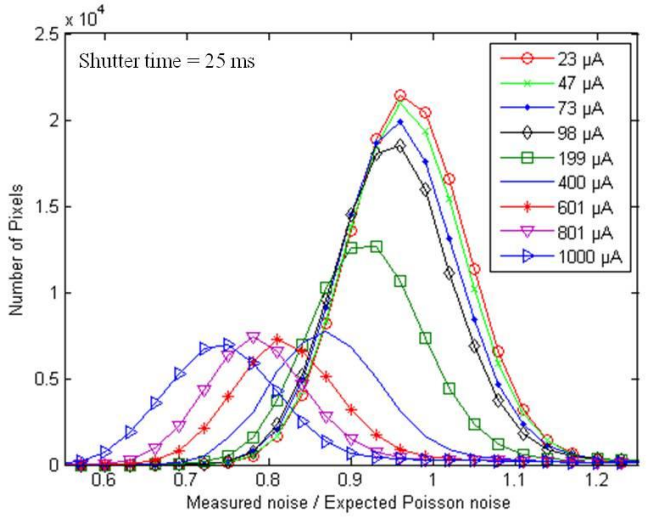

Figure 4.24 Ratio of measured noise to expected noise. The ratio decreases with increasing tube current, to 70 % due to detector saturation.

4.5.5 Flatfield correction

Having measured sensor layer inhomogeneties, individual pixel sensitivity response and saturation effect of both sensor materials, we have corrected for them by applying the flat field correction method. Two hundred images of a mobile phone SIM card (for Si detector) and USB device (for CdTe detector) were acquired by placing the

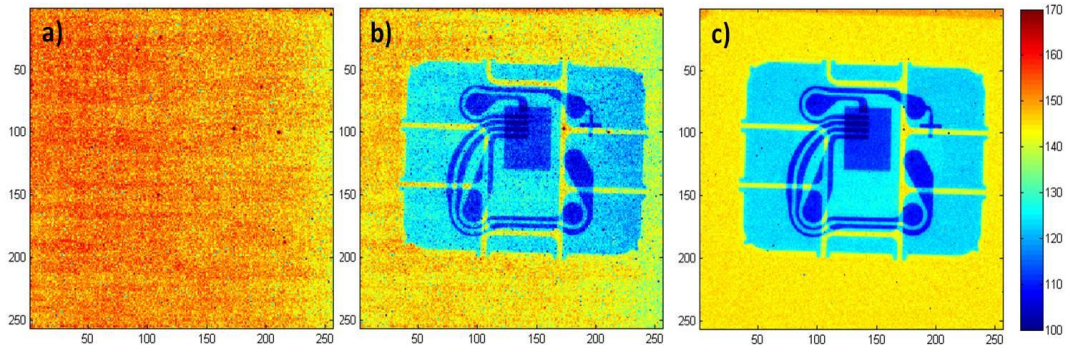

Figure 4.25 One Si sensor: (a) Average of two hundred open beam frames, (b) average of two hundred frames of SIM card and (c) corrected image. The tube current and shutter time was set to 200 µA and 40 ms respectively; other settings remain constant as explained in the experimental setup. The corrected image is the pure flat field image. The colour map has been set so that the image region can be differentiated well. The flood frames were acquired immediately after the SIM card image.

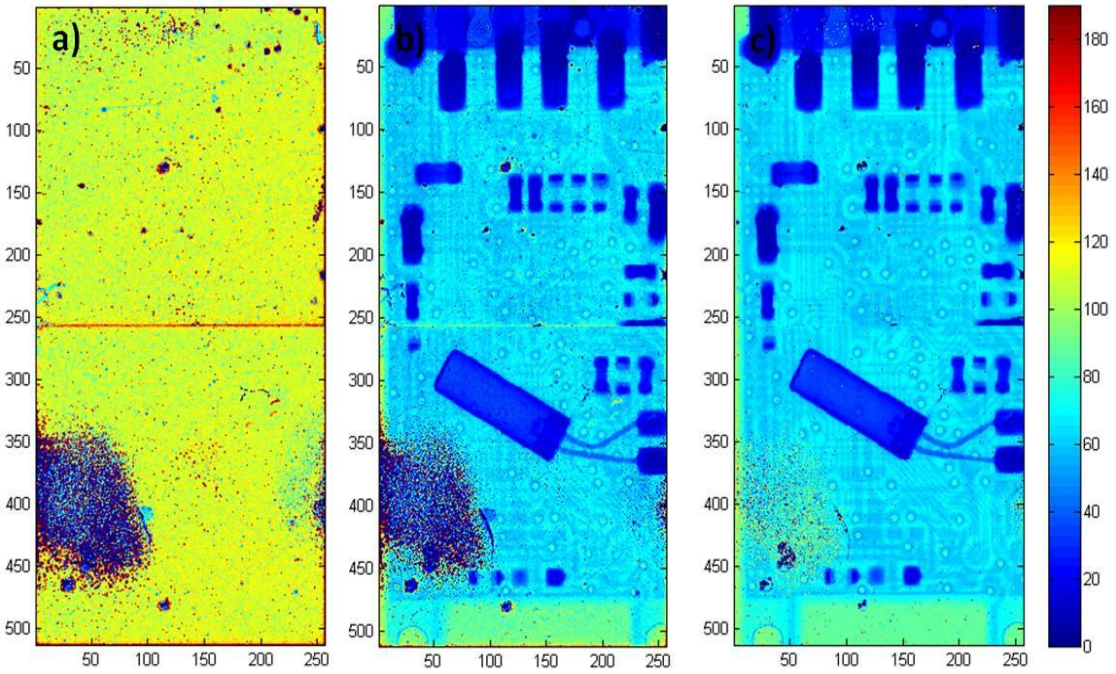

Figure 4.26 Two CdTe sensors: (a) Average of two hundred open beam frames, (b) average of two hundred frames of USB device and (c) corrected image. The tube current was set to 23 µA and the shutter time 30 ms; other settings remain constant as explained in the experimental setup. The corrected image is the pure flat field image without further data processing (masking or interpolation on dead pixels). The colour map has been set so that the image region can be differentiated well. The flood frames were acquired immediately after the USB image.

x-ray source and the detector. The average image was corrected by generating a correction map from an average of two hundred open beam images. A lower photon flux (23 µA) was used for the CdTe detector than for the Si detector (200 µA), based on our understanding from the saturation results. Figure 4.25 and Figure 4.26 show (a) the average open beam image, (b) the average image of an object, and (c) the corrected image. The corrected images show a clear improvement in image quality and reduced inhomogeneities, especially in the CdTe detector.

The correction map is obtained by taking the ratio of the median counts, over two hundred frames for each pixel, to the median counts averaged over the whole detector. There are some regions in Figure 4.26 where pixel sensitivity is so low that flat-fielding alone is insufficient and further data processing is required before CT reconstruction.

4.6 Summary

In the first part of this chapter, we have discussed the basic semiconductor physics. Charge propagation properties under external bias voltages like drift and diffusion and their effect on charge collection efficiency has been reviewed.

A digital testing routine for checking every Medipix2 detector before its release for sensor layer characterization has been discussed. Four Medipix2 chips were analyzed by the author and results from one of the detector was shown. Threshold equalization and energy calibration are considered as the most important features of Medipix chips and need to be done time to time for good image quality. Our current energy calibration routine is in development phase and few group members are comparing different methods for energy calibration and by the time of writing this, experiments are still under way.

In the last section, observations from sensor layer characterization have been discussed. In the experimental study, we have characterized a 300-µm-thick Si and 1-mm-thick CdTe sensor bump bonded to a Medipix2 chip. We have analyzed the sensitivity of 65,536 pixels in Si and 131,072 pixels in CdTe over a hundred frames. We have shown a high degree of repeatability across one hundred consecutive exposures. With the detectors tested, about 0.02 % pixels in Si and ~ 0.7 % pixels in dual CdTe are found to be dead (giving zero counts). We have observed a saturation effect from both

detectors at higher tube currents. We have performed a flat field correction and have demonstrated the improvement this has on image quality.

5 Medipix All Resolution System CT Scanner

This chapter evaluates the geometrical assessment of MARS-CT to deal with system related artefacts and their calibration. The mechanical and geometrical alignment of the MARS-CT scanner is conducted in stages by fabricating customized phantoms.

5.1 Overview

Since the advent of computed tomography in 1970, CT technology continues to advance. In 2008, our team in New Zealand developed the first MARS scanner, a world leading spectral (colour) CT scanner (Butzer 2009). It creates 3D images which depict the distribution and activity of major human diseases. It is designed to be a test-bed or demonstration unit for spectral CT investigations of human pathology and diagnosis of human trauma (Butler, Bell et al. 2008). For this goal, it needs to give excellent spectral CT images of animal models of disease and drug behaviours, both in their own right, and demonstrate on that the technology is ready for full-size human CT.

The geometrical quality assurance routines for MARS-CT have been established by a MARS commissioning team (Dr. Nick Cook, Dr. Judy Mohr, Rafidah Zainon, and Paul Ronaldson and myself). Most of this work has already been documented in the Quality Assurance Manual of MARS scanners for all users (Mohr 2011).

We will start this chapter by reviewing the geometrical assessment of MARS-CT in section 5.2. This section includes the mechanical and geometrical alignment of the MARS-CT scanner. Section 5.3 is about MARS-CT image assessment with the CdTe Medipix2 detector, where we will evaluate spatial resolution, linearity and spectroscopic response, and images of biological samples.

5.2 Geometrical assessment of MARS-CT

The MARS-CT scanner is designed to be highly modular for manufacturing, maintenance, service and upgrade reasons. It consists of a rotating gantry, MARS-Camera (multi-chip board + Medipix detector + readout), cabinet controller, x-ray source, computer hardware and software. The camera, with its software, is designed so it can be used in a stand-alone mode. In principle, the scanner could be used with other x-ray cameras. We have built several versions of the MARS-CT system, now operational in the University of Canterbury (NZ), Mayo Clinic (USA), Virgina Polytechnique Institute (Virginia), Karlsruhe Institute of Technology (Germany), Czech Technical University, and Charles University jointly (Prague) and University of Otago (NZ). The scanner has the ability to operate single, dual, quad and hexa Medipix chips with different sensor layers e.g, Si, CdTe and GaAs, depending upon the application.

To ensure good image quality, it is vital that the MARS-CT scanner is calibrated correctly. The mechanical and geometrical alignment of the scanner sets on the orientation and motion parameters of the gantry, sensor and x-ray source and determines key parameters such as the source-to-detector and source-to-object distances. With advancements in CT technology, several methods have been proposed in the scientific literature to deal with system related artefacts and their calibration (Hsieh 2003; Barrett and Keat 2004; Yang K 2006; Kachelrieß, Semmler et al. 2008; Zhu, Tian et al. 2009; Anas, Lee et al. 2010). This section will provide information on the functioning and operation of various components of a MARS-CT scanner (version 3.4) and its calibration routine.

5.2.1 Cabinet control calibration

Scanner functions are controlled by using raw values (index values), mm or degrees in the text fields. Motor driven movement as a function of the motor index values were tested at the time of machine commissioning. Figure 5.1 shows the optical axis of the MARS-CT scanner in Cartesian coordinates *(x, y, z)*. There are five stepper motors within a MARS scanner, used for the following operations:

- The sample motor controls the translation drive where the sample sits. It moves the sample along the axis of rotation, in and out of the central area i.e., *x-axis*.
- The camera translation motor moves the MARS camera unit in the axis perpendicular to the axis of the sample i.e., *y-axis*.
- The rotation motor rotates the unit about the axis where the sample resides.
- The camera magnification motor moves the MARS camera unit with respect to the sample; moving it closer or further away i.e., z-*axis*.
- The x-ray magnification motor moves the x-ray tube with respect to the sample; moving it closer or further away i.e., z-*axis*.

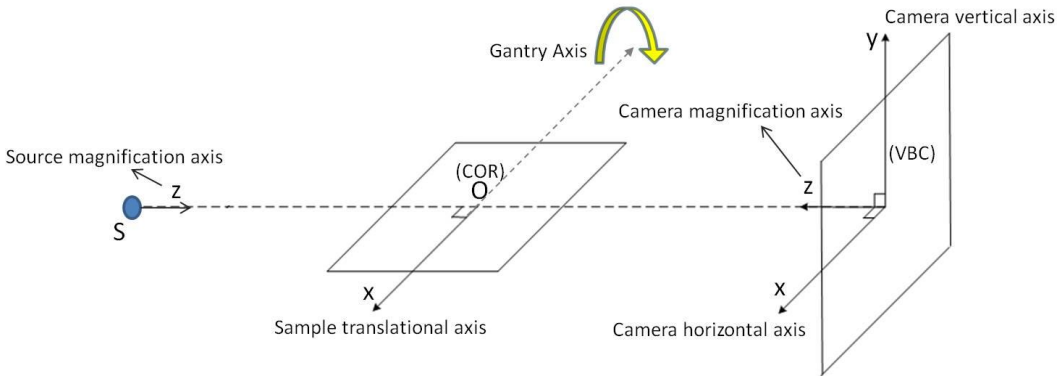

Figure 5.1 The mechanical geometry of MARS-CT system. Here x-ray source '*S*' can move along magnification axis '*z-axis*' and sample can move along translational axis '*x-axis*', whereas, camera can move along magnification axis as well as vertical axis '*y-axis*'. X-ray source and camera rotate around the centre of rotation '*COR*'. '*VBC*' is the vertical beam centre.

With the current mechanical setup, sample translation motion is not an important parameter in MARS-CT scanner as the position of the sample during the entire scan remains fixed for one particular circular scan. All parameters will be discussed according to the geometry explained in Figure 5.1.

5.2.2 Motor driven movements of camera and x-ray source

The camera and x-ray source movements along the magnification axis have been plotted to check the measured displacement against corresponding index values. It is done by rotating the gantry to expose the motor drives, as shown in Figure 5.2, and then

moving the camera and x-ray sources by increments, of ~4000 and ~2000 index values respectively, along the magnification axis as shown in the diagram of mechanical geometry (see Figure 5.1). Both graphs should be straight as shown in Figure 5.3 and Figure 5.4. From the graphs, the measured camera and x-ray source displacement rates are both 2×10^{-4} cm/index.

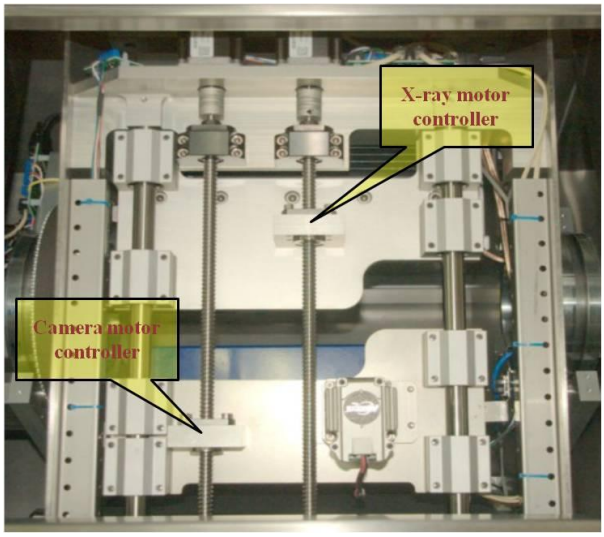

Figure 5.2 Gantry motor drives for the camera and x-ray movements.

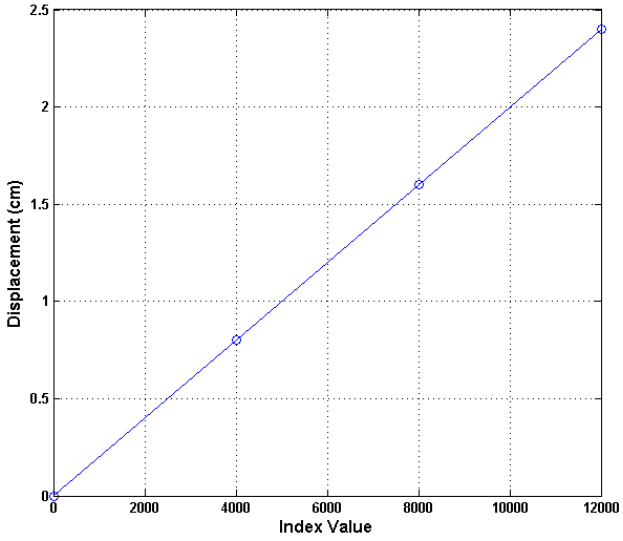

Figure 5.3 Camera displacement plotted as a function of index value.

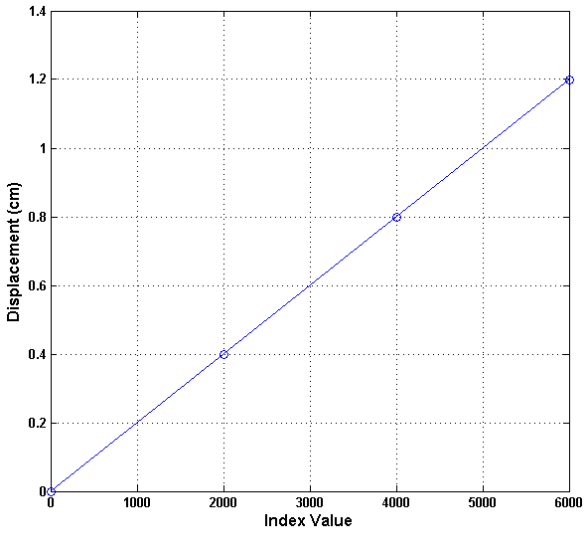

Figure 5.4 X-ray source displacement as a function of index value.

5.2.3 Centre of rotation

The centre of rotation of the scanner (COR) is defined by the projection from the source beam through the axis of rotation onto the camera surface along the x-axis (see Figure 5.1). One of the row numbers in the projection image is the centre of rotation. This number depends on the camera translation parameter for the first (top-most) frame in the stitched image and is used in the reconstruction of CT slices.

The phantom used for these measurements is a straight wire mounted diagonally. An example phantom and an image of the phantom as captured by a MARS scanner are shown in Figure 5.5.

To find the centre of rotation, the phantom is placed in the scanner such that the projection of the wire falls on the camera. The sample translation, gantry rotation and camera translation indices may need to be adjusted and the camera index number noted. Projection images of the phantom are taken from gantry angles 180 degrees apart. The diagonal intersection in the superimposed projections is the horizontal centre of rotation as shown in Figure 5.6.

The measured COR is row number 131 for the camera in its default index position of 28400. This is also sufficiently close to the centre of the frame i.e. row number 128.

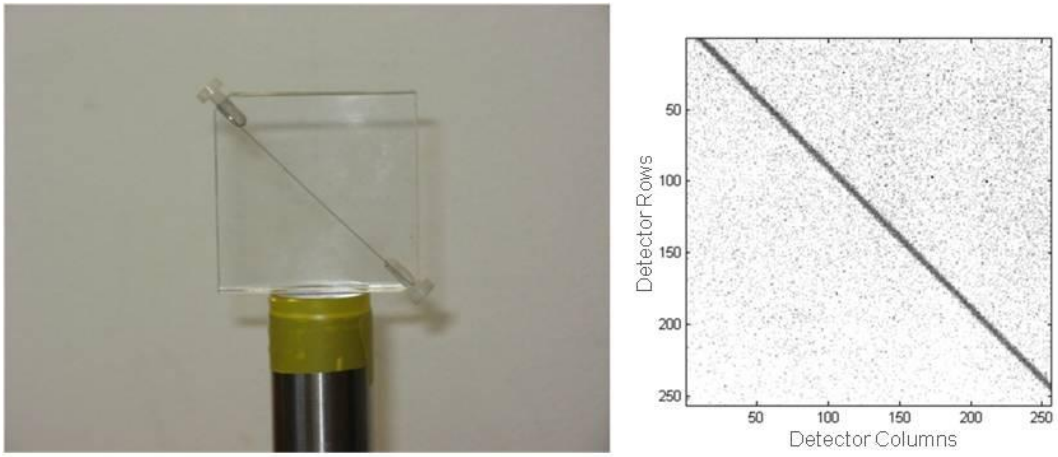

Figure 5.5 *Left:* Phantom used to determine the centre of rotation (COR). *Right:* Projection image taken with MARS-CT using 1.8 mm Al filtered x-ray source, Source-Ray SB-80-1K.

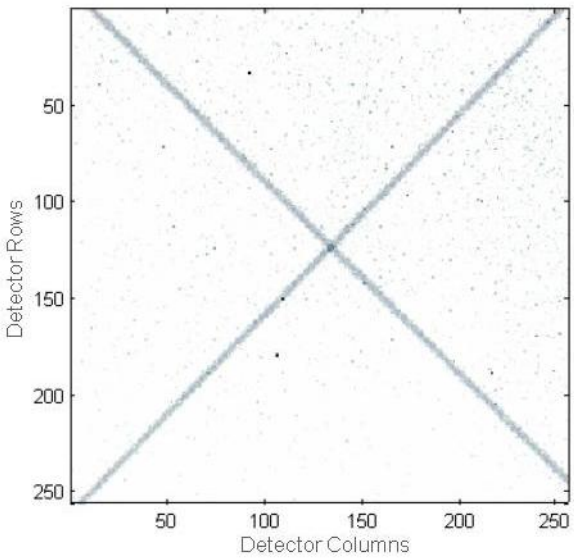

Figure 5.6 Superimposed images of wire phantom taken at gantry angles of 180° to each other. The point of intersection defines the centre of rotation. In this case the centre of rotation is observed at row 131.

5.2.4 Camera translational skew

Medipix detectors have a detection area of ~196 mm^2. This detection area can be increased by butting several chips together (see MARS multi-chip camera) or by using a single camera at multiple vertical axis position i.e., y-axis (see Figure 5.1). This creates a virtual detector of greater area than the individual sensor. However, these individual captured images need to be stitched together appropriately before CT reconstruction. The skew of the virtual detector depends upon the real direction of sensor travel with respect to the image axes.

The camera translational skew measurements use a small single ball bearing phantom as shown in Figure 5.7. For camera skew measurements, the phantom was placed in the scanner such that the projection of the high contrast ball bearing lies at one edge of the frame. Scanning the object in this position, the camera is moved along its vertical translational axis with increments of ~100 index values and then the object is scanned at each position.

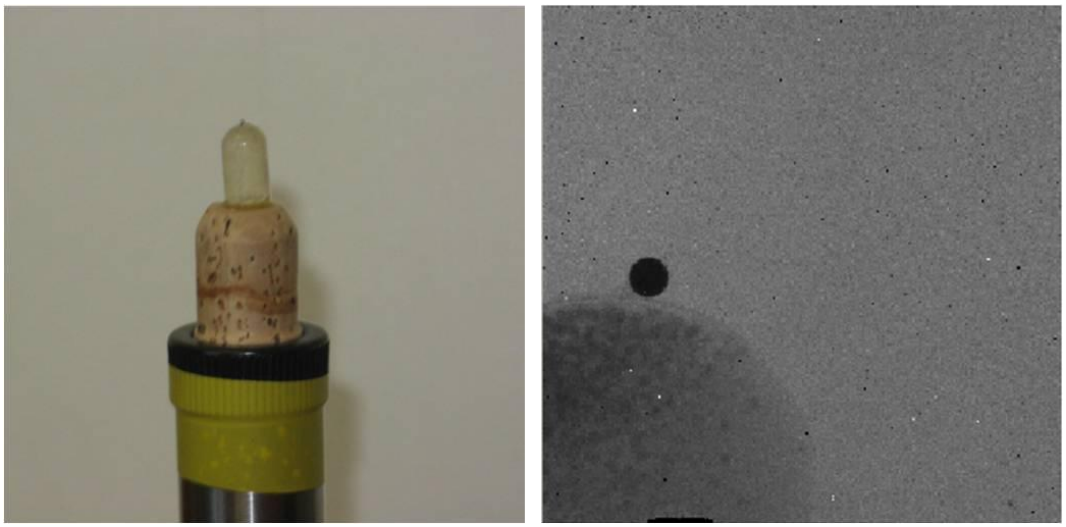

Figure 5.7 *Left:* Camera skew phantom. *Right:* projection image at one of the camera positions. The image acquired using 1.8 mm Al filtered x-ray source, Source-Ray SB-80-1K.

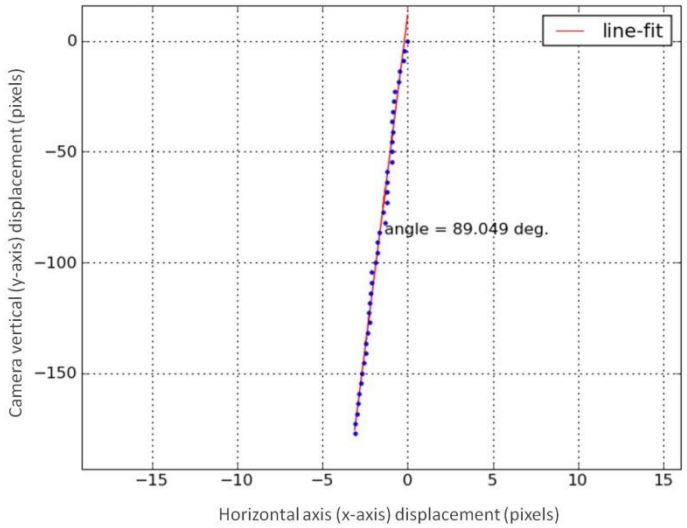

Figure 5.8 Tracking of the ball bearing position through a range of sensor translation position indices.

By plotting the location of ball bearing against the camera index values, the gradient angle can be determined. Ideally, it should be a vertical straight line but practically a certain amount of camera skew angle will contribute to camera translational motion as shown in Figure 5.8. Here, the sensor skew for multiple camera positions is $\theta = 89.05°$. The skew angle is used in stitching algorithms of combined captured images before CT reconstruction.

5.2.5 Vertical beam centre and gantry rotation

The vertical beam centre (VBC) is the column number of the optical axis point of incidence, as shown in the mechanical geometry of MARS-CT in Figure 5.1. It is perpendicular to the rotation axis, and it remains constant for the camera translational motion. It is dependent on the camera translation skew angle 'θ' for the stitched image. The vertical beam centre and gantry rotation measurements use the same small single ball bearing phantom used for the camera translational skew, as shown in Figure 5.7. Placing the phantom inside the scanner, the object is scanned while rotating the gantry over 360°.

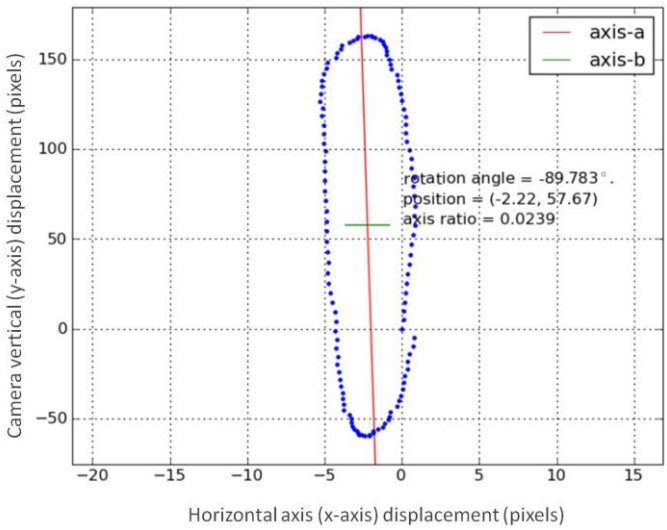

Figure 5.9 Ball bearing position displacement through a 360° rotation. The gantry tile angle and the VBC are determined from the fitted ellipse.

The positions of the ball bearing in all projections are plotted in Figure 5.9. The path that the phantom ball projects onto the imaging plane as the gantry rotates is approximated by an ellipse. The centre of the ellipse is measured by column location (C_y), and the sizes of the major and minor axes, a and b respectively, are used to determine the column displacement of the VBC. When the ball is exactly positioned at the VBC, the minor axis of the ellipse vanishes.

Assuming the gantry rotation tracking ellipse is perpendicular to the horizontal axis and the size of the orbit is much less than SDD, we have:

$$\Delta y = \mathrm{SDD}\frac{b}{a} \tag{5.1}$$

$$VBC = \mathrm{C_y} \pm \Delta y \tag{5.2}$$

Here SDD is the source-to-detector distance in pixels and the selection of $\pm\Delta y$ is determined by the direction of the elliptical plot (clockwise or anticlockwise).

The path of the phantom ball can also be analysed separately for smoothness of gantry rotation and to verify that the 0º and 360º gantry positions align. The angle that the

major axis of the gantry rotation tracking ellipse makes with the pixel rows is known as the *gantry tilt*. It is possible to have an unclosed loop where the final tracking point fails to close the loop with the initial tracking point by an error of ~1 pixel. This is because the gantry can "Walk" on its bearings as it rotates. Latest version (version4) of the gantry hardware has been modified to reduce this effect. Nevertheless this degree of error is unlikely to cause a significant problem with most image reconstructions.

5.2.6 Camera and x-ray source magnification

This protocol evaluates the magnification of a scanned sample, source-to-object distance (SOD) and the source-to-detector distance (SDD). Four different gantry angles (0°, 90°, 180° and 270°) are analyzed and averaged for object magnification, therefore reducing errors caused by gantry rotation misalignments.

The "Magnification phantom" used for these measurements consists of a steel ball bearing having a diameter of 3.88 mm, as shown in Figure 5.10. As a first step, the camera and x-ray source are adjusted to be at their extreme positions (i.e. furthest away from the sample axis), then by using Eq (5.3), the magnification of the ball bearing image as a function of camera index for four gantry angles (90° apart) has been plotted in Figure 5.11.

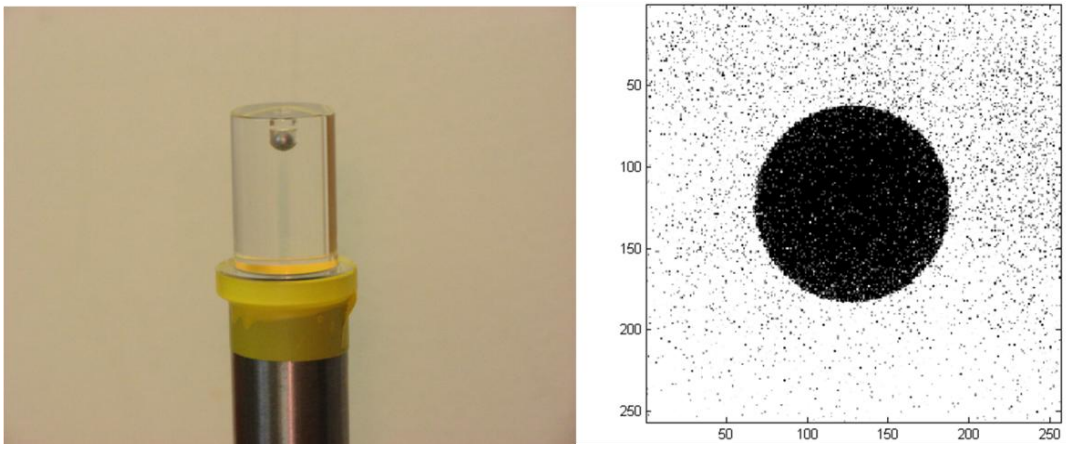

Figure 5.10 *Left:* Magnification phantom. *Right:* projection image of magnification phantom at 0° gantry angle.

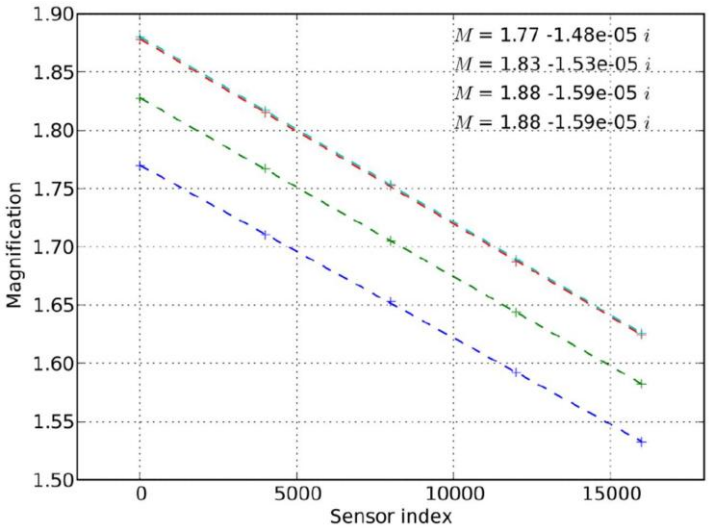

Figure 5.11 Magnification of the ball bearing as a function of sensor index at different gantry angles (90° apart). Here, SOD is the inverse of the gradient (see Eq (5.4)).

$$M = \frac{\mathrm{S_{image}}}{\mathrm{S_{object}}} \tag{5.3}$$

Here 'S' is the size and 'M' shows the magnification of the object. SOD has been determined from the gradients of the fitted lines

$$SOD = -\frac{SDD}{M} \tag{5.4}$$

Substitute SOD for M_o (Magnification at 0 camera index) to find the SDD from

$$M = \frac{SDD}{SOD} \tag{5.5}$$

At zero camera index value, the average SOD and average SDD are 64516 index and 118777 index units respectively. By multiplying these index values with the camera and x-ray displacement rate i.e., 2×10^{-4} cm/index (from section 5.2.2), SOD and SDD can be determined.

5.2.7 Gap determination between two chips

The detection area of the chip at one camera position can be increased by butting several chips together on a single chip carrier board with a gap of few hundred microns between them. For silicon quads, the gap between each chip is known accurately i.e., ~165 μm (~3 pixels) because they are made from a single wafer. The CdTe detectors for MXR are made with several single ASIC chips attached to separate pieces of CdTe so separation is variable and always needs measuring. It is necessary, due to the fact that large inter-chip separation produces reconstruction artefacts and, therefore, needs interpolation. Here, we will determine the gap between two CdTe chips, whose flood frame is already shown in the sensor layer characterization section (see Figure 4.9 (b)).

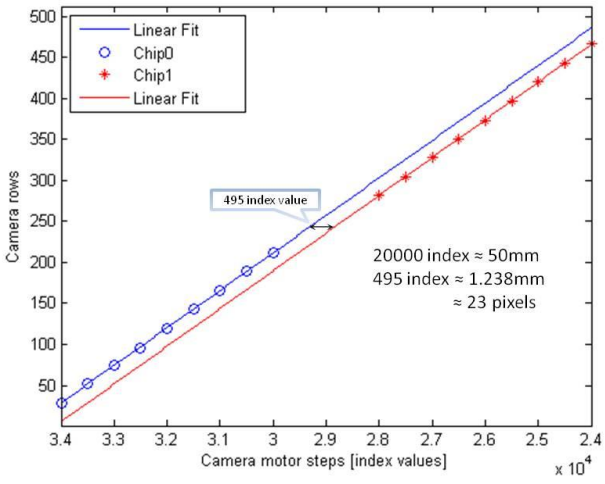

Figure 5.12 Determination of the dead region between two CdTe chips. A separation of ~23 pixels is observed.

Measurement of the gap between two chips, or dead region determination, uses the same single ball bearing phantom used for magnification measurements, as shown in Figure 5.10. Place the phantom inside the scanner so that the projection of the ball bearing lies at one edge of the chip. Scanning the object in this position, move the camera along its vertical translational axis with increments of ~500 index values and record data for the chips. By plotting the detector rows as a function of camera steps for two chips, the gap between them was determined as shown in Figure 5.12. We found a dead region

of ~1.238 mm (~23 pixels) between dual CdTe chips. If there were no gap between chips, then both lines would lie on-top of each other.

5.3 MARS-CT performance with CdTe-Medipix2

This section will address the system performance in terms of spatial resolution, linearity response, spectroscopic response and imaging of a quality biological sample, e.g., mouse. Geometrical unsharpness and random noise are two major factors affecting the quality of a CT image. Geometrical unsharpness limits the spatial resolution whereas; random noise limits the contrast sensitivity to the presence or absence of any material of the CT system. After characterization of the CdTe detector and geometrical assessment of MARS-CT, it is essential to test the performance of MARS Spectral CT by using the dual CdTe Medipix2 detector. For that purpose, all phantoms and biological samples were scanned with the dual CdTe-Medipix2 detector (512×256 pixels). 360 circular projections (1 projection/degree) were acquired using a Source-Ray SB-120-350 x-ray tube (Source-Ray Inc, Ronkonkoma, NY) with a tungsten anode having 1.4 mm of aluminium (equivalent) intrinsic filtration. The focal spot size was ~40 µm. Depending upon the height of the sample, various vertical positions of CdTe camera may be required to have enough overlapping to ensure that each pixel location has been sampled by a good pixel.

The raw data from the scanner was pre-processed using the *MARS-CT builder* software. The pre-processing performs flat-field corrections, stitching of corrected frames to generate the complete projection, and then its conversion into sinograms. Ring filtration is applied on sinograms to reduce ring artefacts. Finally, the filtered sinograms were used to create 3-D CT images by using the commercial CT reconstruction software *Octopus* (Dierick, Masschaele et al. 2004). Other parameters like threshold energies, kVp settings and vertical camera positions will be mentioned accordingly.

5.3.1 Spatial resolution

Sometimes simply referred to as resolution, it is actually the smallest distance between two adjacent points that can be resolved in the image. The closer together they are with the image still showing them apart, the better the resolution of the system (J. T.

Bushberg 2002). We measured it by determining the modulation transfer function (MTF) at the edge of a 10 mm cylindrical perspex phantom. 14 keV low threshold energy was used to scan the phantom while setting the tube voltage at 120 kVp with 6 vertical camera positions (1.5mm / stop). CT slices corresponding to a thickness of ~1 mm were stacked, averaged and then analyzed.

MTF was generated according to the protocols described by the American Society for Testing and Materials report (E1695 2006). The edge response function (ERF), obtained by analyzing the perspex-air boundary profile and by differentiating, results in the line spread function (LSF). The Fourier transformation of the LSF generates the MTF. Figure 5.13 shows the spatial resolution corresponding to 10% MTF.

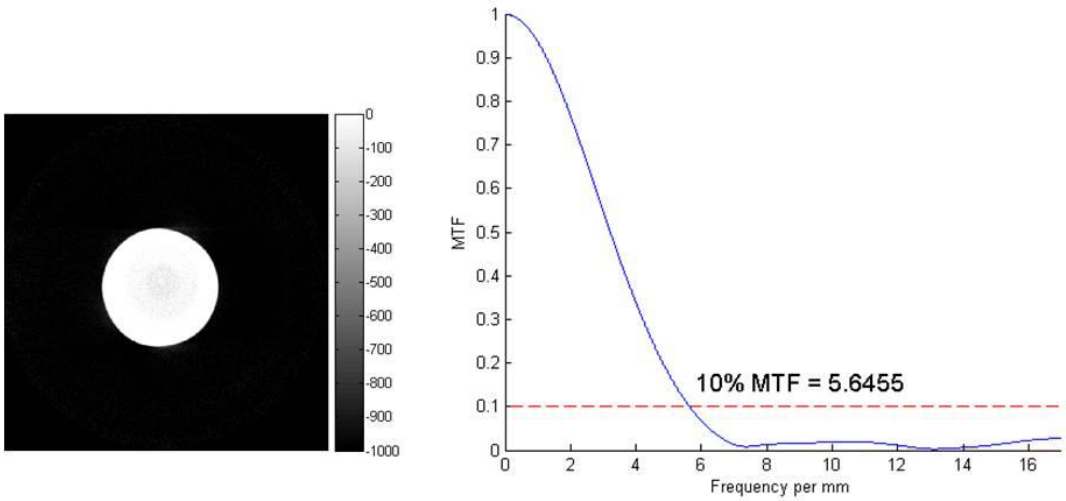

Figure 5.13 *Left*: CT slices corresponding to a thickness of ~1 mm used for MTF evaluation. *Right:* The MTF falls at a spatial frequency of 5.6 mm^{-1}.

Paul Ronaldson (Ronaldson, Butler et al. 2011) has reported a resolution of ~110µm for MARS-CT with a Medipix3-Si detector. Spatial resolution is affected by a number of factors, such as the focal spot of x-ray tube, the pixel size, the charge sharing among pixels, and the CT reconstruction algorithm (Bartling, Stiller et al. 2007). For this system, 10% MTF falls to spatial frequency of 5.65 mm^{-1} as shown in Figure 5.13, which is equivalent to a resolution of ~165µm.

5.3.2 Linearity response over diagnostic range

The aim of this test was to assess the linearity response of MARS-CT at higher energy ranges.

Eight different concentrations (0, 0.78, 1.562, 3.125, 6.25, 12.5, 25 and 50 mg/ml) of 30nm gold nanoparticles (AuNPs) were scanned at 120 kVp by setting a low threshold energy at 81 keV (Au K-edge = 80.7 keV) along with 10 vertical camera positions. By selecting ROI from the 3-D CT image over each concentration, the relationship between gold attenuation and its concentration was analysed. This was achieved by plotting Hounsfield Units (HU or CT number) as a function of concentration. The HU for each concentration was calculated by using air and water references (Hounsfield 1973) in the Eq (5.6):

$$HU = \frac{\mu_{\text{sample}} - \mu_{\text{water}}}{\mu_{\text{water}} - \mu_{\text{air}}} \times 1000 \qquad (5.6)$$

Here μ is the *linear attenuation coefficient*.

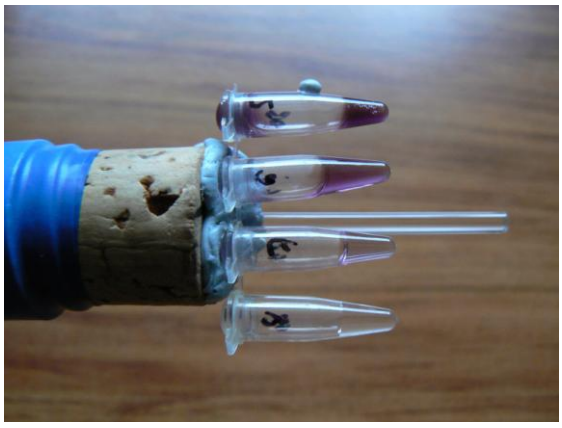

Figure 5.14 Four out of eight vials of different concentrations of gold nanoparticles were scanned at a time with multiple camera positions to cover the complete sample height.

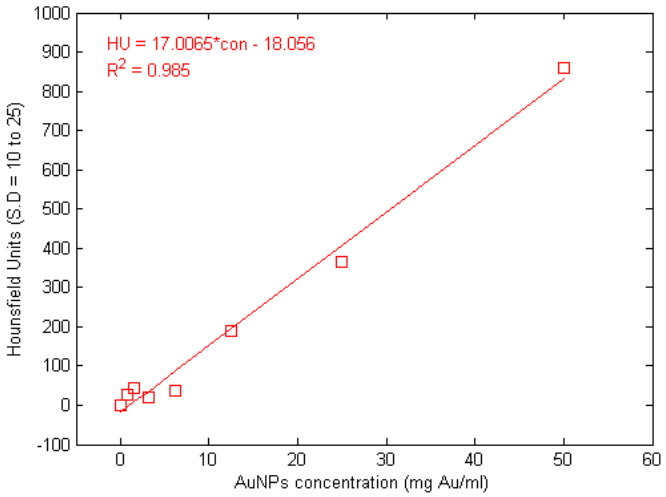

Figure 5.15 Hounsfield Unit as a function of AuNPs concentrations (V = 120 kVp; E_{THL} = 81 keV).

Linearity determines the ability of a system to detect the presence or absence of any material. It can be affected by random noise, beam hardening and photon starvation (Barrett and Keat 2004). The response in HU to different concentrations of AuNPs is shown in Figure 5.15. The linear fitted line indicates the system's linearity response over a range of concentration (R^2 = 0.985) at E_{THL} = 81 keV.

5.3.3 Spectroscopic response

The aim of this test was to analyze the ability of MARS-CT to distinguish low and high Z materials together in the low energy to high energy range.

A 9.5 mm multi-contrast phantom was scanned with ten E_{THL}. The phantom has four vials of 2mm having high concentrations of gold (196.97 mg/ml) and iodine (126.90 mg/ml) along with vegetable oil (referred to as fat) and water. The combination of threshold energies and their corresponding shutter times are given in Table 5.1. Different tube voltages are used to optimise the energy bins for reduced noise and less charge sharing.

Table 5.1 Experimental setup for spectroscopic response of AuNPs, Iodine & oil.

Threshold Energy (keV)	Tube Voltage (kVp)	Tube Current (μA)	Exposure time (s)
11, 14, 20	42	60	1.2, 1.6, 3.2
30, 33, 50	80	60	1, 1.3, 4
75, 81, 85, 90	120	60	2.5, 3.5, 4.5, 8.5

8 vertical movements of the dual CdTe camera were acquired to cover a sample height of ~9.5 mm (including margins) by moving the camera ~1.5 mm for each vertical position. CT slices corresponding to a thickness of ~0.5 mm were stacked, averaged and then analyzed. The spectral response in transverse slices is shown in Figure 5.16. The attenuation profile of the materials has been analyzed by plotting HU as a function of energy in Figure 5.17.

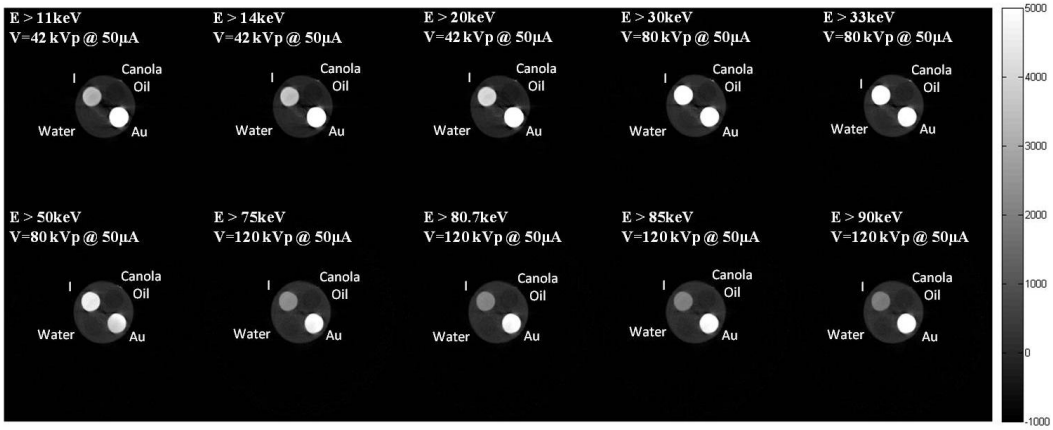

Figure 5.16 Transverse slices of 9.5mm phantom with four vials individually filled with AuNPs, iodine, oil and water. The colour-map represents HU ranging from -1000 to 5000.

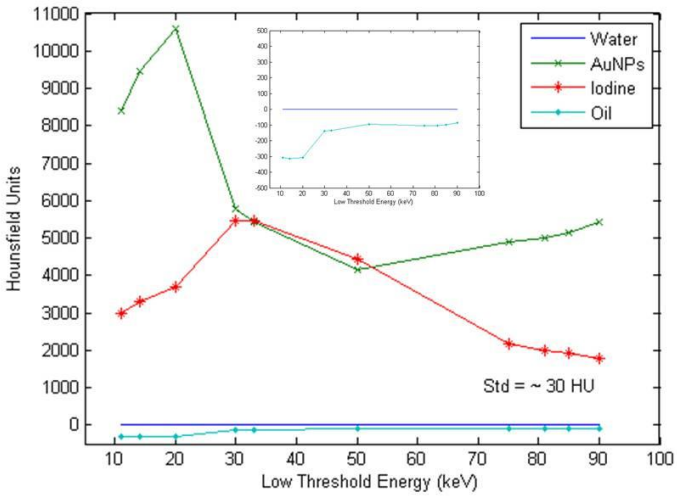

Figure 5.17 Attenuation profile of gold, iodine and oil as a function of energy. The inset is a zoom in profile of oil.

Biomarkers are indicators of diagnosis, disease burden or treatment effect. As already mentioned, our aim is to use spectral CT non-invasively to directly measure multiple biomarkers simultaneously in the target tissue to quantify the disease as it happens, where it happens. Figure 5.16 and Figure 5.17 show the HU for gold contrast agents, which initially increases with threshold energy due to influence of L-edge at 14 keV, then decreases with energy, but increases again due to the influence of its K-edge at 80.7 keV. The same is the case for iodine which has its K-edge at 33.2 keV. On the other side, the HU of the low Z material (oil) increases uniformly with energy (inset Figure 5.17).

5.3.4 CT images of biological sample

To demonstrate the performance of MARS-CT with a CdTe-Medipix2 assembly, a lower abdominal region of a resin fixed plain mouse (without any contrast agent) was imaged by computed tomography. The tube voltage was set at 50 kVp and the low threshold set at 15 keV with 7 vertical stops (1.5 mm/stop). Volumetric reconstruction, from filtered back projection data, has been done after acquiring a large number of partially overlapping projection frames. Figure 5.18 shows one of the 3-D CT images (slice number 77) of a mouse along with the 3-D volumetric view of the vertebral bone +

tail. A clear discrimination between soft tissue, fat, resin (used to preserve mouse for long term) and bone can be seen in Figure 5.18.

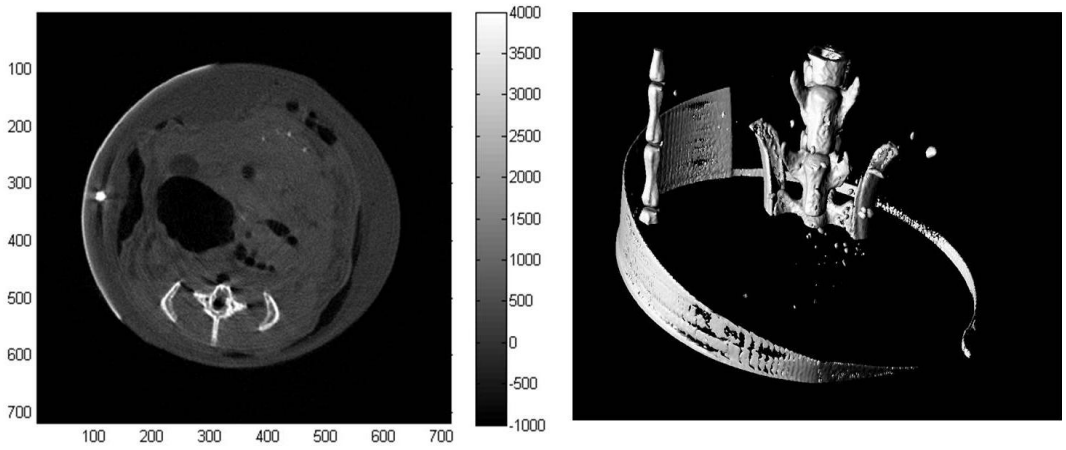

Figure 5.18 *Left:* CT image of lower abdominal region of mouse showing clear discrimination between tissue, fat, resin and bone. The image is rescaled into HU. *Right:* 3-D volumetric view of whole lower abdomen of mouse showing bone. (V = 50 kVp; E_{THL} = 15 keV)

5.4 Summary

To ensure good image quality, a geometrical assessment of every scanner is necessary before its release for pre-clinical use. Simple customized phantoms have been used for the determination of the centre of rotation, camera translational skew, vertical beam centre, gantry rotation, gap between two chips and various other parameters.

After geometrical calibration, performance of MARS-CT with the CdTe Medipix2 detector in terms of spatial resolution, linearity response, spectroscopic response and imaging of biological sample was discussed. A spatial resolution of ~165µm with good linearity response and spectroscopic discrimination has been shown. The section is concluded by the demonstration of good image quality in a biological sample.

From the mechanical aspect, the dead region of ~1.238 mm (~23 pixels) between dual CdTe chips is considered to be one of the important causes of undesirably longer scans. Another reason is the saturation of the CdTe semiconductor material at high fluxes which limits the detector operation at high tube currents. Ring artefacts were observed in

almost all data sets. The major cause of these artefacts is the pixel variations, which were not fully compensated by the flat-field protocol.

6 Imaging of gold nano-particles with MARS-CT

This chapter presents the experimental evaluation of gold nanoparticles imaging. The molecular imaging feature of the MARS-Spectral CT is investigated, using the spectroscopic ability of the Medipix detector. The study aims to demonstrate the feasibility of using functionalized gold nanoparticles for spectral CT imaging that selectively target thrombotic events to advance individualised medicine and diagnosis of major diseases.

6.1 Overview

In this pilot study I demonstrate that spectral CT is a quantitative imaging tool with the potential to make major advances in non-invasive assessment of vulnerable plaque. Gold nanoparticles are ideal new macromolecular imaging agents. Our group is leading the development of spectral CT, an imaging technology which allows specific identification and quantification of high Z materials (such as gold) at high spatial resolution. For this study unless otherwise stated, my role was to prepare samples, gather the required data and performed all the statistical analysis.

Some results from this chapter have been reported in the 27th Image and Vision Computing New Zealand (IVCNZ 2012) held at Dunedin, NZ (26th to 28th Nov). We start this chapter by a brief overview of the limitations of current imaging modalities for the assessment of vulnerable plaque and tumour response to treatment in section 6.2 and 6.3 respectively. Section 6.4 describes the working principle of nanoparticles as radiographic pharmaceuticals. Gold nanoparticles, their advantages over conventional contrast agents, and their selection criteria into this project will be reviewed in section 6.5. Finally, in section 6.6 experimental work related to the identification of biomedical nanoparticles in MARS-CT will be discussed.

6.2 Vulnerable plaque and limitations in current diagnostics

Cardiovascular disease is one of the leading causes of death and a major cause of hospitalization in New Zealand (Hay 2004; Crooke 2007). Fatal events such as myocardial infarction (heart attack) and stroke are typically precipitated by the rupture of vulnerable atherosclerotic plaques and consequent vascular blockage (Writing Group, Roger et al. 2012). The detection of plaque vulnerability (a soft lipid pool covered by a thin layer of fibrous cap) is critical for preventing the severe downstream effects of heart disease. Atherosclerotic plaques can rupture as a result of the breakdown of the fibrous cap that covers the lipid core via inflammatory processes. It accounts for ~70% of fatal acute myocardial infarction or sudden coronary deaths (Lobatto, Fuster et al. 2011). Figure 6.1 shows the growth mechanism of vulnerable plaque in the coronary artery and the breakdown of fibrous cap with histology.

Atherosclerosis (progressive narrowing and hardening of arteries) and thrombosis (rupture of vulnerable plaque) are commonly diagnosed by angiography (invasive coronary imaging) or by intravascular ultrasound. Positron emission tomography (PET) is sensitive but non-specific with limited spatial resolution and they only allow for the identification of the most severely obstructive plaque (Vancraeynest, Pasquet et al. 2011). It is also limited due to low uptake of the radioisotope by atherosclerotic plaque.

The detection of unstable (vulnerable) atherosclerotic plaque is limited due to the lack of sensitive imaging modalities and invasive procedures. Also they may not determine the inflammatory status of plaque (Pavlo, Yahya et al. 2012). The angiography procedure is invasive and associated with risk and may cause infection, pain or bleeding at the site where the catheter was inserted. Catheters which are made of plastic can cause trauma or damage to the blood vessels. Although the inflammatory status of the atherosclerotic plaque may be determined by the combination of the above methods, it would be best to have a single imaging modality with improved diagnostic ability and lower risk.

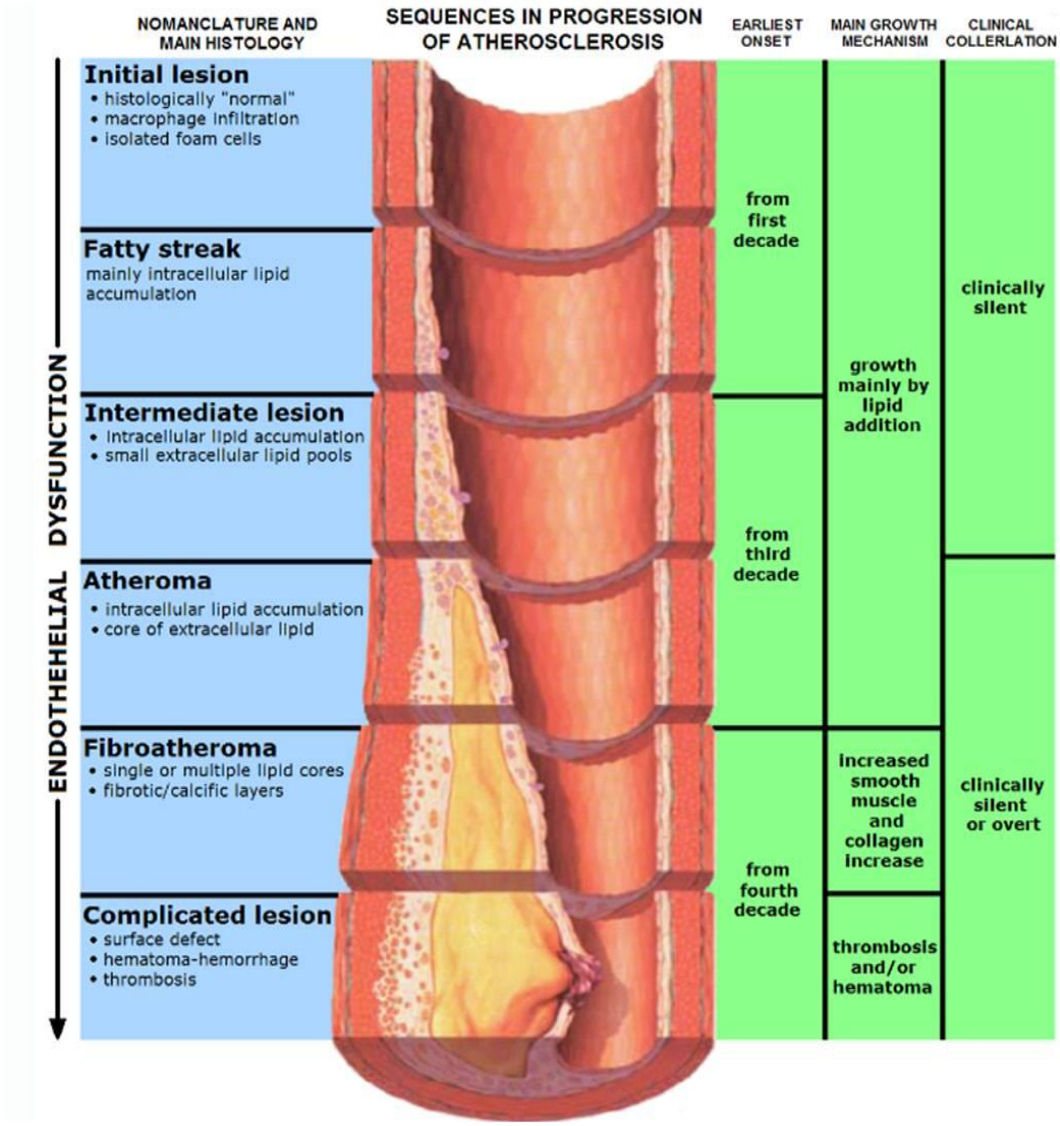

Figure 6.1 Growth mechanism of vulnerable plaque. The rupture in the innermost layer (intima) of the artery (bottom slice) can be seen. The rupture usually occurs along the margins of the plaque and triggers blood clotting, causing partial or complete obstruction to blood flow. The blood clot can further grow and cause sudden occlusion of the artery and known as arterial thrombosis. Image is taken from http://almostadoctor.co.uk/.

6.3 Assessment of tumour response to treatment and current limitations

Cancer is another leading cause of death in NZ (Health 2011). It can be diagnosed by number of ways but its treatment is mostly by surgery, radiotherapy,

chemotherapy or combination of all three. Chemotherapy kills the cancer cells, but the size of the chemotherapy agents is a major determinant of its toxicity. Conventional chemotherapy agents usually have low molecular weight (< 1 kDa or < 1 mg/mole). This small molecular size allows systemic distribution, but exposes both the normal tissue and tumour to the drug. If drugs are incorporated in macromolecules (> 40 kDa or > 40 mg/mole), selective drug delivery to tumour is enabled, reducing toxicity to the normal tissue (Daruwalla, Nikfarjam et al. 2010). This is also referred to as anticancer nanomedicine. Nanomedicine is a rapidly growing field that specially focuses on tumour targeting for the purpose of diagnosis and treatment (Kedar, Phutane et al. 2010). Unlike small molecular weight conventional chemotherapy, macromolecules enter cells by endocytosis, not through diffusion (Maeda, Fang et al. 2003). They are designed to accumulate through the leaky blood vessels, with fenestrated endothelium, that is found in tumours. The ideal macromolecular drug would remain bound in circulation and only release the drug inside the tumour (Greish, Fang et al. 2003; Gormley, Greish et al. 2011). This process of tumour accumulation through leaky vessels varies from one patient to another, depending on the nature, size, and site of the tumour tissues (Grossman and McNeil 2012). In vivo measurements of these processes are required if we are to assess the effectiveness of drug delivery, the response of tumour to treatment and the toxicity to adjacent normal tissue.

All these challenges require what is now called molecular imaging, currently performed by PET, PET-CT and PET-MRI (Weissleder 2006; Weber, Czernin et al. 2008). These modalities need radioactive pharmaceuticals to be made on site shortly before imaging and require an expensive cyclotron on site. Bioluminescence and fluorescence molecular imaging, mainstays of current cancer molecular imaging in small animals, are very sensitive but not translatable to human imaging due to their poor penetration. Therefore, these imaging modalities do not allow tumour response to treatment to be assessed non-invasively.

MARS spectral CT is a quantitative imaging tool with potential to make major advances in non-invasive spectral molecular imaging by utilizing nanoparticles at high spatial resolution.

6.4 Nanoparticles

Nanoparticles can be engineered as nanoplatforms for effective and targeted delivery of drugs, diagnosis, treatment and control of biological systems. These nanosize delivery systems can also be used simultaneously with imaging labels, enabling them to concentrate selectively in targeted tissues, overcoming many biological, biophysical, and anatomical barriers (Cai, Gao et al. 2008; Ulbrich and Lamprecht 2010). The use of nanoscaled carriers in drug delivery is expected to increase drug specificity, thus reducing side effects and decreasing the dose of the administered drugs (Barreto, O'Malley et al. 2011; Lobatto, Fuster et al. 2011).

The primary application of nanoparticles in medicine was initially in cancer. Angiogenesis – the growth of new blood vessels is one of cancer's hallmarks. Angiogenic blood vessels supply nutrients (oxygen & glucose) to the tumour, but because of their own rapid growth, they are irregular in architecture and leaky (Grossman and McNeil 2012). They also have larger gap sizes in their walls than healthy blood vessel. The pore size of a healthy blood vessel is between 2–6 nm, whereas, angiogenic blood vessels have a pore size that generally ranges from a few hundred nanometres to a few microns. The nanoparticles between 10 to 300 nm are just the right size to penetrate into these angiogenic blood vessels without significantly penetrating into healthy tissues (Zhang, Gu et al. 2007). By loading anticancer drugs, selective drug delivery to the tumour is enabled. Generally, the targeting principle of nanoparticles in cancer can be divided into non-specific targeting (via enhanced permeability and retention effect (EPR)) (Maeda 2010), specific targeting, or tumour cell targeting (using functionalized nanoparticles) (Ferrari 2005).

Nanoparticles also have a substantial role in the management of coronary artery disease in general – atherosclerosis in particular. By attaching antibodies, proteins or other ligands, nanoparticles can be targeted to atherosclerotic plaque (similar to tumour cell targeting). However, there are several factors which should be taken into account to enable efficient targeting of nanoparticles: 1) rapid renal clearance of nanoparticles occurs if their size is less than ~ 5nm, 2) large diameters of nanoparticles (>100 nm) can look like a virus to phagocyte system (body defensive immune system) and cause them to be shuttled to the liver and spleen, preventing them to target desired sites and 3) surface

charge of nanoparticles may bind them to non-desired areas (most cell membrane have -ve charge). Most of these factors can be prevented by using an appropriate size of nanoparticles and by increasing the circulation time in the blood. Coating of nanoparticles with polyethylene glycol (PEG), a charge neutral molecule, also helps in neutralising the particle and results in higher circulation time. For more detail, reader is referred to scientific literature (Moghimi, Hunter et al. 2005; Kirpotin, Drummond et al. 2006; Wickline, Neubauer et al. 2007).

This project tests gold nanoparticles in MARS spectral CT for the non-invasive detection and quantification of thrombotic events in excised human atheroma, and cancer in mouse models.

6.5 Gold nanoparticles

Contrast agents are commonly used to improve the visibility of internal body structures in medical imaging modalities (CT, x-ray projection or MRI), particularly for the early detection of anatomical and functional abnormalities. In the last few decades, several varieties of nanoparticles for use in medical imaging have been discussed in various literature reviews, e.g., (Rabin, Manuel Perez et al. 2006; Thurn, Brown et al. 2007; Gao, Gu et al. 2009). For this project we are interested in gold nanoparticles (AuNPs) as a contrast agent due to the following resons: 1) Au has its L-edge (14 keV) and K-edge (80.7 keV) in the diagnostic energy range, which emphasizes its unique linear attenuation curve. Thus with the MARS spectral scanner it should be possible to separate gold from any other background structure. 2) To overcome the limitations of diminished image contrast between small vessels and tissue surrounding the vessels at higher energies. 3) To test AuNPs with the molecular imaging feature of MARS spectral scanner that selectively target thrombotic events and cancerous cells. 4) They are proven to have little or no toxic effects.

Hainfield et al (Hainfeld, Slatkin et al. 2006) were the first to describe AuNPs with no evidence of toxicity, even on histologic examination. Cai et al and Boote et al (Cai, Kim et al. 2007; Boote, Fent et al. 2010) also reported increased circulation time with no toxicity. Gold has several advantages over conventional iodinated radiopharmaceuticals. Several investigators (Jackson, Rahman et al. 2010; Badea, Johnston et al. 2011) have

shown superior x-ray attenuation of gold over iodine. Gold achieves a contrast up to 3 times greater than iodine per unit mass at ~100 keV. Furthermore, gold concentrations up to 5 times those of iodine can be achieved, providing a total contrast gain of up to ten times or more (Hainfeld, Slatkin et al. 2006). Unlike iodine, gold has very low viscosity and osmolality (number of moles of solute per kilogram of solvent), delivers more gold atoms per molecule than iodine (250 atoms of Au compared to 3-6 atoms of iodine), and therefore may be used in small blood vessels without risk of vascular damage. The high atomic number of gold (Z = 79) results in higher contrast. Therefore, AuNPs might enable non-invasive detection of small tumours (< 1cm), and allow for discrimination between stable and unstable plaque (which is currently not detectable). AuNPs also provide a high degree of flexibility in terms of functional groups for coating and targeting. That is, they can be bound to drugs, targeted to tumour biomarkers, or added to antibodies to attach at desired sites.

6.6 MARS-CT: Spectral imaging to molecular imaging

Spectral CT is specific, non-invasive, and quantitative. It can simultaneously measure several biomarkers of biological processes at molecular and cellular level (scanning with multiple energy bins allows multiple markers to be measured). This molecule specific imaging is known as molecular imaging or functional imaging. Spectral CT has the potential to non-invasively quantify drug delivery to tumours and identify thrombotic events (Popovtzer, Agrawal et al. 2008; Pavlo, Yahya et al. 2012). There is very limited published research on spectral CT with AuNPs, and its molecular imaging feature (mainly because spectral CT is so novel).

The outcome obtained from this study has provided proof of concept for further development of this approach. The scanning of human and animal tissues was approved by the regional ethics committees i.e., Human Ethics (CTY/01/04/036) and Animal Ethics (AEC 11/10, University of Otago).

6.6.1 Materials and methods

In these experiments, we use 1 mm thick dual CdTe sensors (512×256), bump-bonded to individual Medipix2 MXR readout chips and installed in MARS-CT6 (6 referred to scanner number). 720 to 1080 circular projections over 360° have been acquired using a Source-Ray SB-120-350 x-ray tube (Source-Ray Inc, Ronkonkoma, NY) with a tungsten anode having 1.4 mm of aluminium equivalent intrinsic filtration. The focal spot size was ~40 µm. Several vertical positions of CdTe camera were used depending upon the height of the sample to create a virtual detector of greater area than the individual sensor. The bias voltage applied to the sensor was −438 V. A magnification factor of ~1.5 has been calculated for these experiments. The camera readout was performed using the MARS readout system. Before the measurements, threshold equalization with respect to the noise edge, and energy calibration of the detector, were performed. Flat-field measurements were taken before and after specimen scanning to correct for variations in pixel response. Other parameters like threshold energies, kVp settings, and vertical camera positions will be mentioned accordingly.

6.6.1.1 Spectroscopic study with AuNPs

The aim of this experiment was to analyze the ability of MARS-CT to distinguish different low Z materials from various concentrations of high Z materials in the diagnostic energy range. The study will elaborate the potential of the MARS-CT system for simultaneous discrimination among different materials.

Table 6.1 Experimental setup for multi-contrast phantom study

Threshold Energy (keV)	Tube Voltage (kVp)	Tube Current (µA)	Exposure time (s)
10, 15, 20	42	60	0.5, 0.9, 2.2
30, 34, 40, 51	80	60	0.7, 1.1, 1.8, 5
55, 60, 81, 85, 90	120	60	0.8, 1.2, 5.5, 7.5, 12

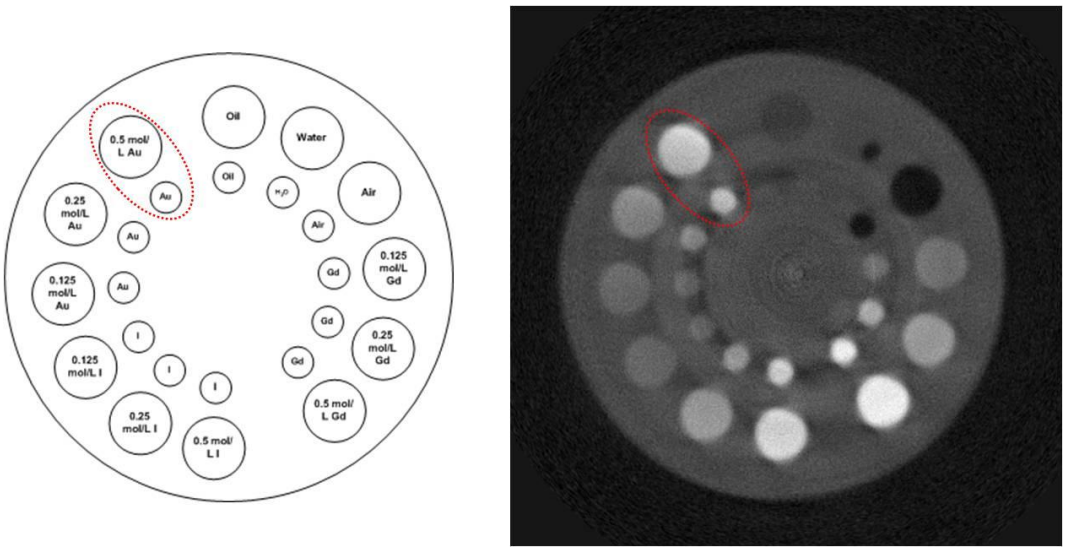

Figure 6.2 *Left:* Schematic of Perspex phantom with 24 vials. One pair (consists of bigger and smaller vial) has same concentration (an example pair is highlighted by red dotted line). *Right:* CT image of the phantom corresponding to schematic on the left. The red dotted line shows one pair having the same concentration of AuNPs as in the phantom schematic.

A 14 mm multi-contrast phantom was scanned with 12 energy thresholds. The description of threshold energies and their corresponding shutter times are given in Table 6.1. Six vertical positions of the dual CdTe camera have been acquired to cover the sample height by moving the camera ~1.5 mm for each vertical position. The phantom has 24 vials (12 pairs of bigger and smaller vials). The bigger vial has a diameter of 1.6 mm, while the smaller one has a diameter of 0.8 mm. The phantom's smaller vials depict an approximate vessel size of a mouse. The concentration selection has been shown in Figure 6.2 (left). Overall, the phantom has three concentrations (0.5, 0.25 and 0.125 molar) of AuNPs, iodine and gadolinium along with oil, water and air. Deliberately high concentrations of contrast elements were used to clarify the printed images. The AuNPs were delivered by Aurovist (Nanoprobes).

6.6.1.2 Mouse study with AuNPs

The aim of this experiment was to develop a technique for the in-vivo scanning of mouse injected with AuNPs. The vision is to translate the study into different mouse

models (tumour induced, high cholesterol) injected with AuNPs so that they can be targeted to tumours or added to antibodies to attach at desired sites.

Two mice, each of weight ~20g, were scanned with the MARS-CT system. The mice were anaesthetised with isofluorane (5%) in oxygen. 200 µl of 1.9 nm AuNPs at a dose of ~1.11 g Au per kilogram of body weight (22.2 mg Au for 20g mouse) was injected using a 1ml syringe and 32 gauge needles. The LD_{50} (lethal dose) for this material is ~3.2 g Au per kilogram and therefore no toxicity is observed by Hainfeld, even at ~2.7 g Au per kilogram for the same type of AuNPs (Hainfeld, Slatkin et al. 2006).

While injecting Mouse1 via its tail vein, the first attempt failed, however it was then successfully injected via the dorsal vein of the penis. It was euthanized by cervical dislocation 2 min after the injection. Mouse2 was first injected via the dorsal vein of the penis but this was unsuccessful; it was then successfully injected via the intra-cardiac route. Mouse2 was also euthanized by cervical dislocation 10 min after the injection. Mice injections were performed by Dr. Bruce Dobbs (Department of Surgery and Gastroenterology, CDHB) at Christchurch School of Medicine. Both animals survived the attempted injections, were euthanized afterwards, radiographed (2-D x-ray projection), fixed in the resin to preserve them by CraftSmart liquid gloss (CraftSmart Australia, Glayton North, Australia) in a 25mm Perspex phantom, and then scanned.

To scan the mouse, 6 vertical positions of the dual CdTe camera were acquired to cover the sample height. This was achieved by moving the camera ~1.5 mm between each vertical position. The tube was operated at 120 kVp with a current of 110 µA and using four low energy thresholds (7, 25, 55, 81 keV). Figure 6.3 shows a plain radiograph (taken at Christchurch Women Hospital) of the two mice with their highlighted regions of interest. Due to the first unsuccessful injection in the dorsal vein of Mouse2, the spreading of the AuNPs can be seen in its knee areas.

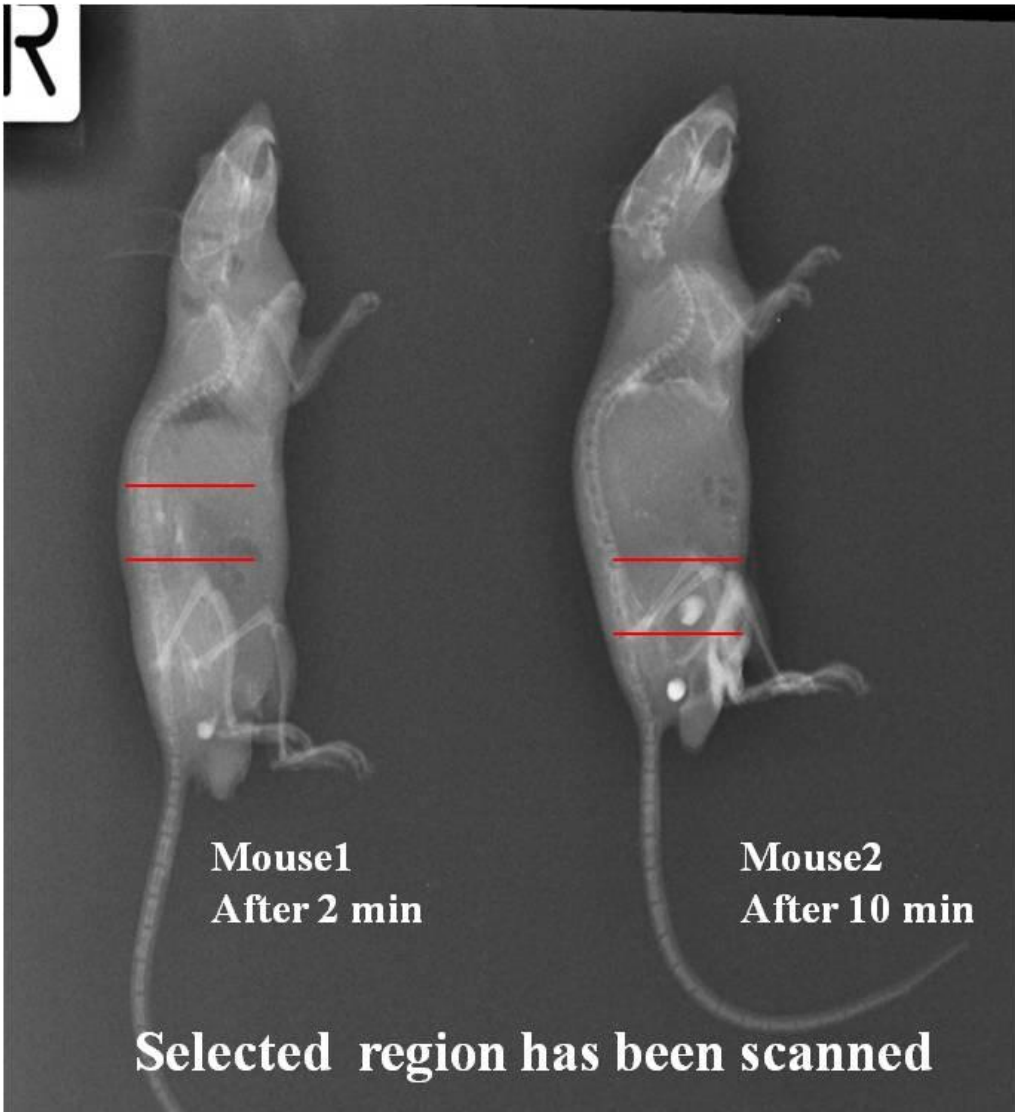

Figure 6.3 X-ray projection of 2 min (left) and 10 min (right) post injection mice. Mouse1 has AuNPs in its kidneys, whereas in Mouse2, AuNPs clear via bladder after 10 min of injection. The selected regions from the mice have been scanned in MARS CT.

6.6.1.3 Imaging of vulnerable plaque

The aim of this experiment is to demonstrate the feasibility of using functionalized gold nanoparticles for visualization and quantification of selectively targeted thrombotic events in available human plaque samples.

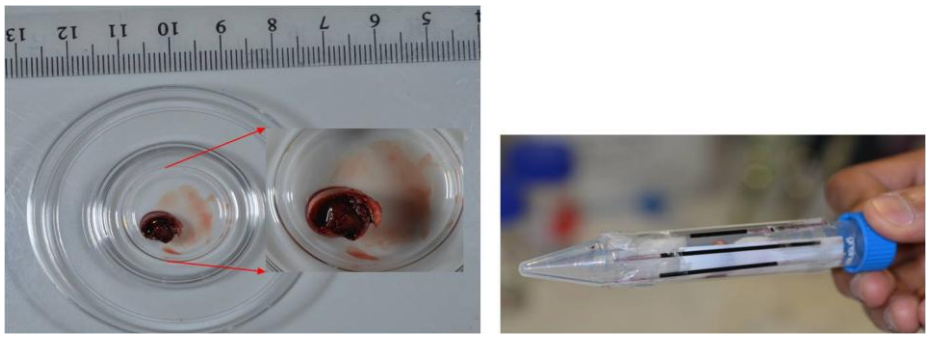

Figure 6.4 *Left:* Incubation of one of the specimens. The inset is a zoomed in view of the incubated specimen. *Right:* Capillary tubes around falcon tube for data calibration can be seen. Here, the tube is loaded with three different concentrations of Au (25, 12.5, 6.25 mg/ml).

This experiment was performed in collaboration with the Atherothrombosis and Vascular Laboratory, Baker IDI Heart and Diabetes Institute, Melbourne, Australia. Three excised carotid atherosclerotic plaques were taken from a -80 °C freezer, where they were stored after surgery a few days prior to the scan. The plaques were sliced by a hand held microtome blade and regions with platelet rich thrombi were selected for scanning. AuNPs with a single chain antibody (AuNP-scFv) were prepared by the Baker group in Australia (Ta, Prabhu et al. 2011) and used for incubation at the Free Radical Biochemistry Laboratory, Canterbury University. Two specimens were individually incubated with 50 mg of Au per millilitre of 30 nm AuNP-scFv for two hours at room temperature, and were then washed with 15 ml of 0.25% PSA in PBS for 10 to 20 min with gentle shaking. Washing removes the AuNPs attached to the undesired site. A third sample, using a negative control (non-binding AuNPs), was also passed through the same protocol. The samples were photographed at high resolution by the Biology photography technician.

The specimens were then scanned individually in an ordinary falcon tube. 5 vertical positions of the dual CdTe camera were used to cover the sample height. The x-ray tube was operated at 120 kVp with a tube current of 110 µA, using four low energy thresholds (10, 25, 55, 83 keV). For data analysis and HU calibration, capillary tubes having different concentrations of Au (25, 12.5 and 6.25 mg/ml) and $CaCl_2$ (500, 250, 125 mg/ml) along with air and water were attached to the falcon tube. The capillary tube data from one specimen was used to calibrate the others since scanning conditions were the same.

6.6.1.4 Imaging of mouse tumour

The aim for these experiments is to visualize biological processes taking place at the molecular and cellular level for non-invasive quantification of macromolecular drug delivery in mouse cancer models by using nanoparticles in the MARS scanner.

B16 Melanoma cells and Lewis Lung carcinoma (LLC) cells were injected subcutaneously into the flank area of three and six female mice respectively. All mice, aged between two and four months and each weighing approximately 20g, were scanned with the MARS-CT system. Three weeks after cell injections, when the tumours were approximately equal or more than 350 mm^3, four mice (two B16 Melanoma and two LLC) were anaesthetised with isofluorane (5%) in oxygen and injected intravenously via tail vein (0.2 ml) with 40.5 nm ± 10.2 AuNPs at a dose of ~0.125 g Au per kilogram of body weight (2.5 mg Au for 20g mouse) using a 1 ml syringe and 29 gauge needles. The remaining five mice (one B16 Melanoma and four LLC) were injected intravenously via tail vein (0.2 ml) with 70 nm ± 9 silver nanoparticles (AgNPs) at a dose of ~0.04 g Ag per kilogram of body weight (0.8 mg Ag for 20g mouse). Silver nanoparticles (AgNPs) were only used due to limited availability of gold nanoparticles. Mice injections were performed by Dr. Katie Saunders (Director Research Facilities, UO) at Christchurch School of Medicine.

All mice survived the attempted injections and were euthanized by CO_2, 24 hrs after the injection. The mice were radiographed, fixed in the resin to preserve them in a 25mm Perspex phantom, and then scanned. For data analysis and HU calibration, capillary tubes having different concentrations of Au (12.5, 6.25 and 3.125 mg/ml) and $CaCl_2$ (500, 250, 125 mg/ml), along with air and water, were attached to one of the mice injected with AuNPs. Different concentrations of Ag (8, 4 and 2 mg/ml) and $CaCl_2$ (500, 250, 125 mg/ml) along with air and water were also attached to one of the mouse injected with AgNPs. The capillary tube data from one specimen was used to calibrate the others since scanning conditions were the same.

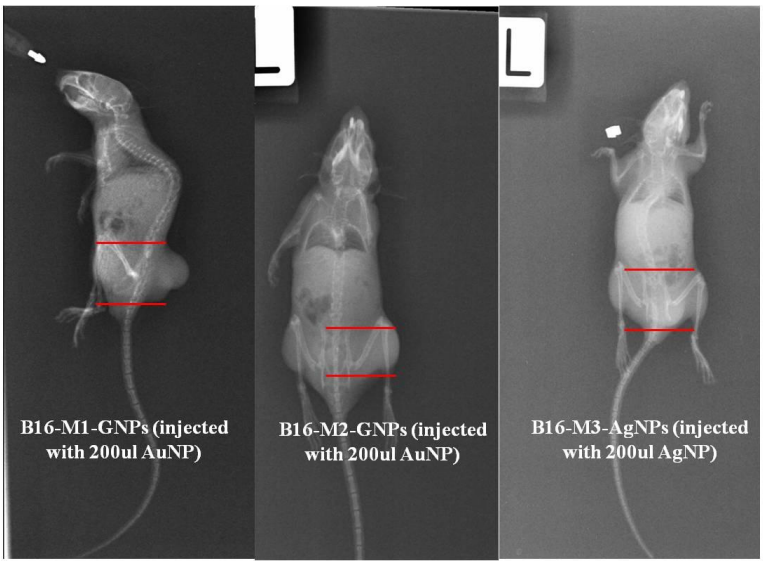

Figure 6.5 Post injection (after 24 hrs) x-ray projection of B16 Melanoma mice, injected with AuNPs. The selected regions from the mice have been scanned in MARS CT.

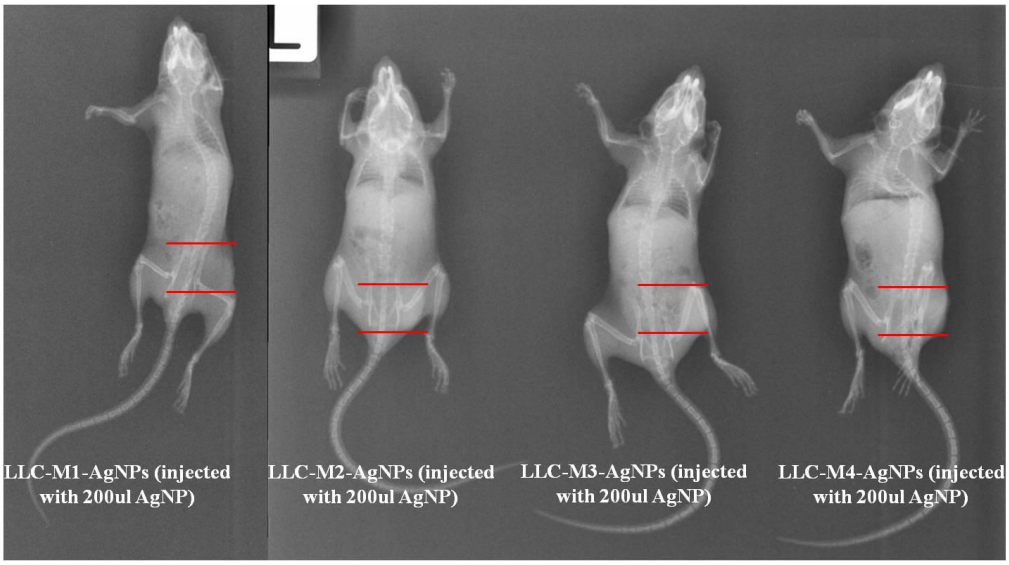

Figure 6.6 Post injection (after 24 hrs) x-ray projection of LLC mice, injected with AgNPs. The selected regions from the mice have been scanned in MARS CT.

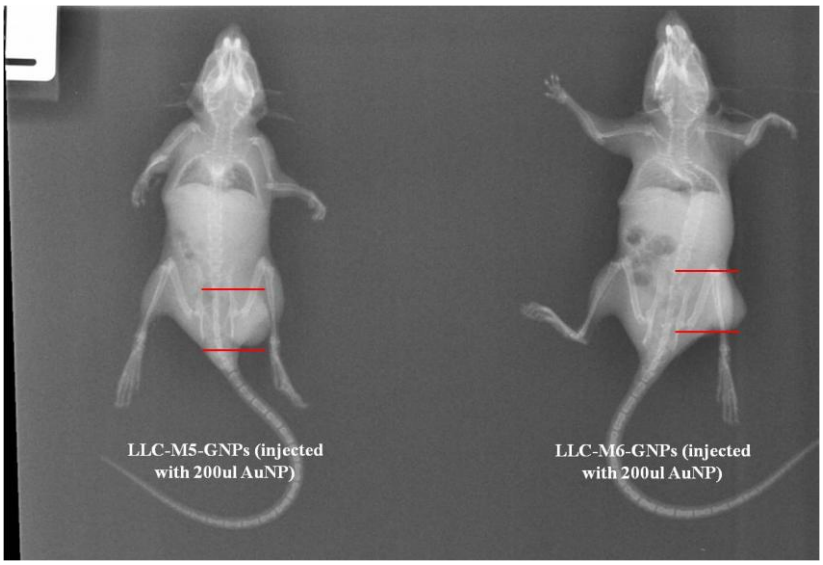

Figure 6.7 Post injection (after 24 hrs) x-ray projection of LLC mice, injected with AuNPs. The selected regions from the mice have been scanned in MARS CT.

To scan the mouse, 6 vertical positions of the dual CdTe camera were acquired to cover the sample height, by moving the camera ~1.5 mm between each vertical position. For AuNPs injected mice, the tube was operated at 120 kVp with a current of 120 µA and five low energy thresholds (12, 18, 55, 81 & 90 keV) were used. Whereas, for the AgNPs injected mice, the tube was operated at 80 kVp with a current of 120 µA, using five low energy thresholds (12, 18, 23, 27 & 40 keV). Figure 6.5, Figure 6.6 and Figure 6.7 show a plain radiograph (taken at Christchurch Women Hospital) of all mice with their highlighted regions of interest.

6.6.2 Results

In this section, we present results of the spectral CT imaging of the in-vitro and in-vivo samples.

6.6.2.1 Spectroscopic study with AuNPs

CT slices corresponding to a thickness of ~0.5 mm were stacked, averaged and then analyzed. Images showing the spectral response of the transverse slices are shown in Figure 6.8. The x-ray attenuation profile was analyzed by plotting Hounsfield units as a

function of energy, as shown in Figure 6.9. Figure 6.10 shows the classification of gold, gadolinium, iodine, fat and water in the phantom data. It has been performed by using a constrained least squares technique developed by one of the MARS group members (Paul 2012).

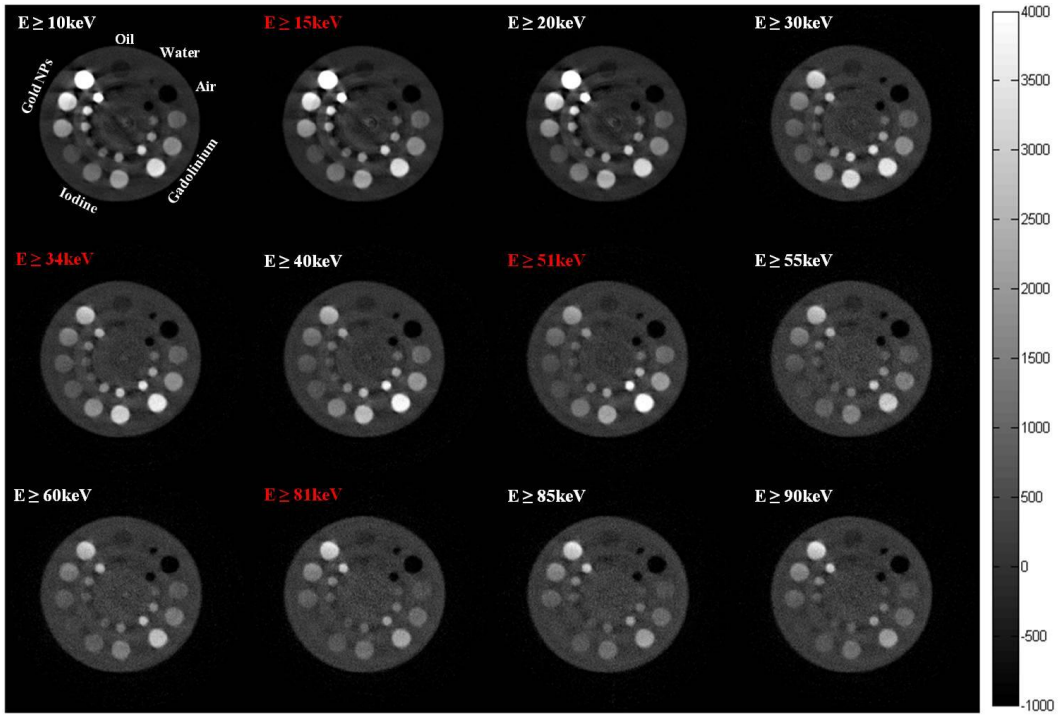

Figure 6.8 Images showing transverse slices of a 14mm phantom with 24 vials individually filled with AuNPs, iodine, gadolinium, oil and water. The colour-map represents HU ranging from -1000 to 4000. The red highlighted text represents the absorption edge range of gold (L-edge = 14 keV), iodine's K-edge (33 keV), gadolinium's K-edge (51 keV) and the K-edge of gold (81 keV) respectively. Higher value for HU can be seen at each element's respective absorption edge.

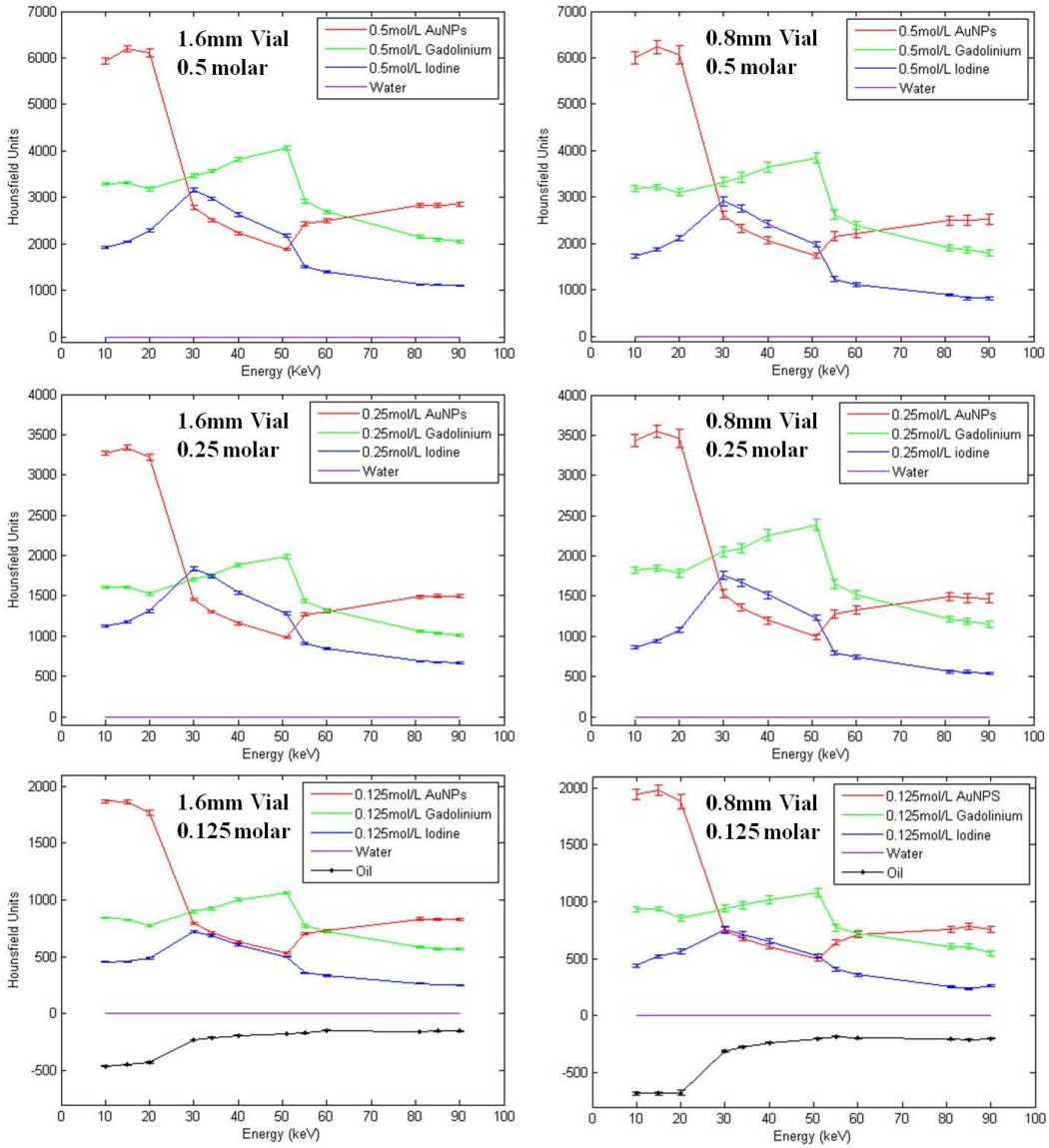

Figure 6.9 Attenuation profile of different concentrations of gold, gadolinium and iodine as a function of energy for big (left) and small vials (right). The bottom graphs with the lowest concentration of contrast elements also include the response of fat (oil). An increase in HU is observed at each element's respective absorption edges. The error bars represent the standard deviations.

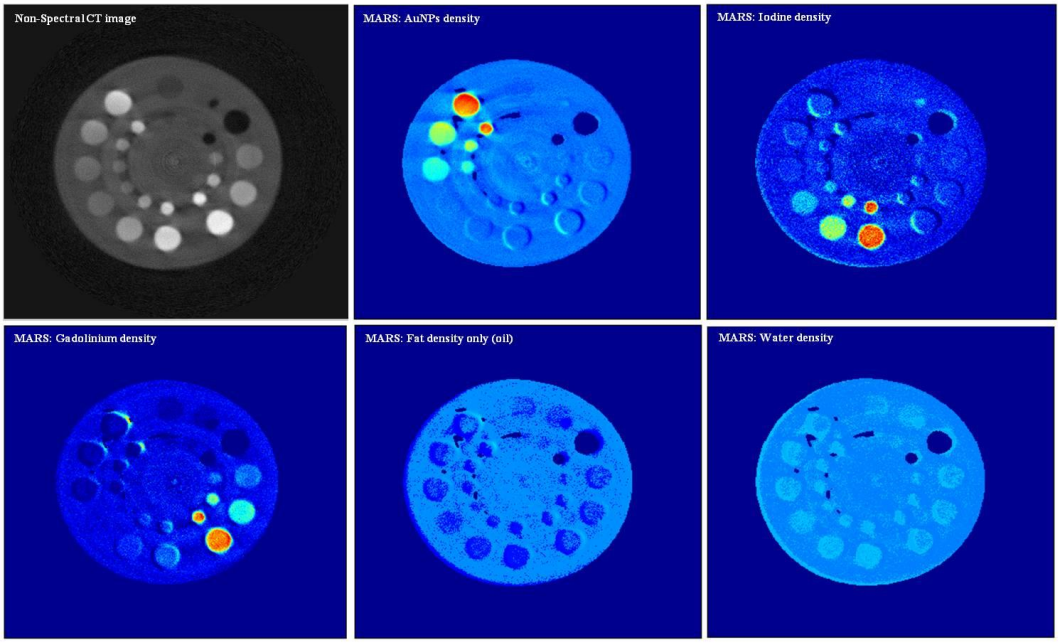

Figure 6.10 Classification of non-spectral CT image into individual element by different color codes. *Top (left to right)*: non-spectral CT image, image with only AuNPs and image with only iodine density. *Bottom (left to right)*: image with gadolinium density, only fat and image with water density.

6.6.2.2 Mouse study with AuNPs

The volumetric reconstruction from filtered back projections has been done by acquiring a large number of partially overlapping 720 circular projections. Although the presence of AuNPs can be seen in grey scale images of the kidneys, principal component analysis (PCA) has been applied for more clear discrimination. PCA is a statistical technique used for multi-dimensional data. Here different threshold energies, considered as different dimensions, were used to separate base data into different materials. More detailed consideration of PCA and its mechanisms can be found in the scientific literature (Anderson, Butler et al. 2010; Butler, Butzer et al. 2011). Figure 6.11 and Figure 6.13 display broad spectrum CT images of a mouse kidney and mouse bladder respectively, and their corresponding colour coded images with PCA. Figure 6.12 and Figure 6.14 show the 3-D volume visualization of the mouse kidneys and the mouse bladder with AuNPs.

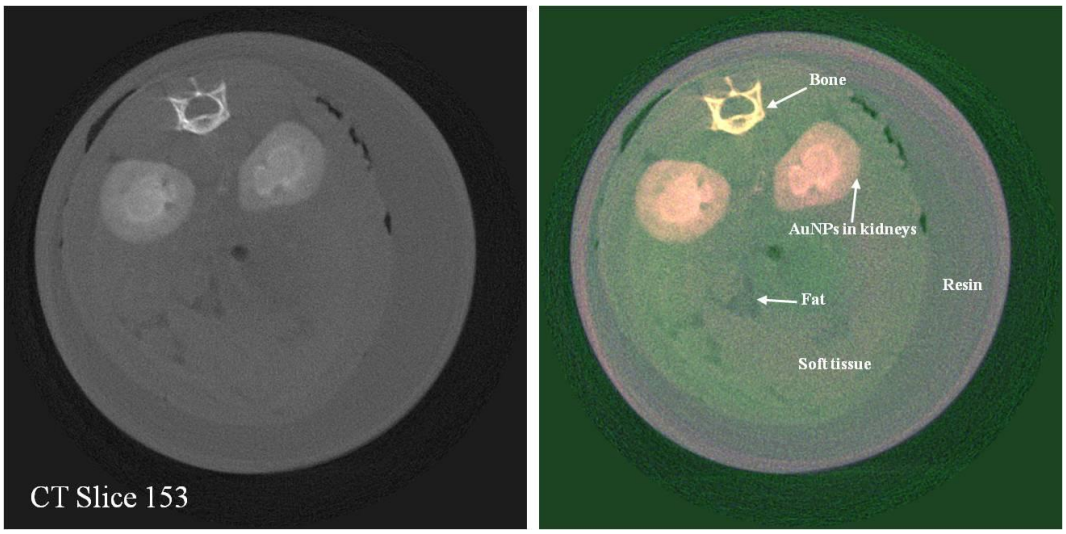

Figure 6.11 Spectral CT (using MARS scanner with CdTe Medipix2-MXR photon-processing detector) of mouse kidneys showing calcium in bone (yellow) differentiated from gold (pink) in mouse kidneys. *Left*: broad spectrum gray-scale image of mouse kidneys containing gold nanoparticles. *Right:* colour spectral CT image using PCA showing bone (yellow), and gold (pink) nanoparticles within mouse kidneys. Also clear discrimination can be observed between fat, soft tissue and resin.

Figure 6.12 3D volume visualization of mouse kidneys using MARS Spectral CT. A clear separation within the kidney structure between renal cortex and pyramids can be seen.

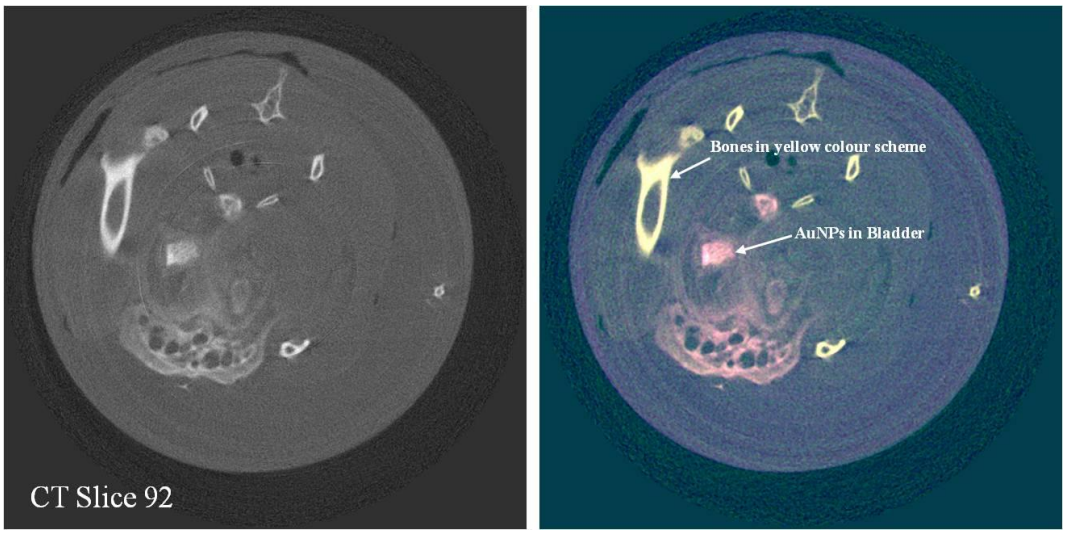

Figure 6.13 Spectral CT of mouse bladder showing calcium in bone (yellow) differentiated from gold (pink) in mouse bladder. *Left*: broad spectrum gray-scale image of mouse lower abdominal region containing AuNPs. *Right:* colour spectral CT image using PCA showing bone (yellow), and gold (pink) nanoparticles within mouse bladder.

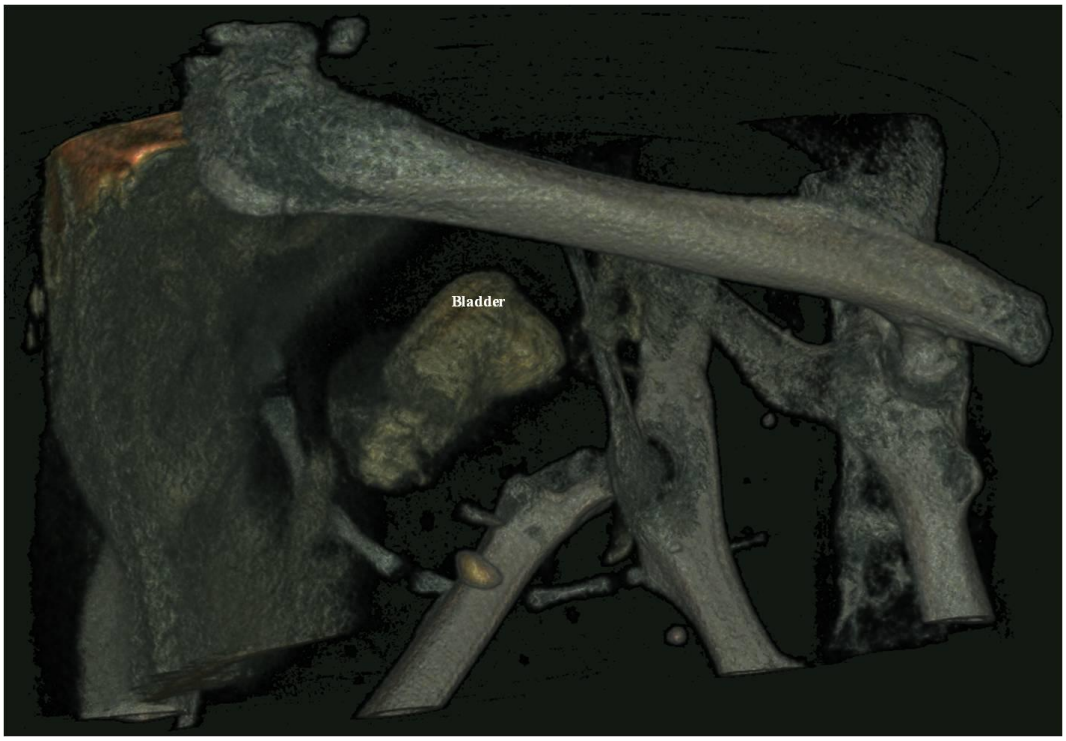

Figure 6.14 3-D volume visualization of lower abdominal region of mouse using MARS Spectral CT. Bladder in the centre can be seen clearly.

6.6.2.3 Imaging of vulnerable plaque

For data analysis and HU calibration, capillary tubes having different concentrations of Au and $CaCl_2$ were assessed for all four threshold energies, as shown in Figure 6.15. This information will be used to correlate between the known (contrast material) and unknowns (suspected regions).

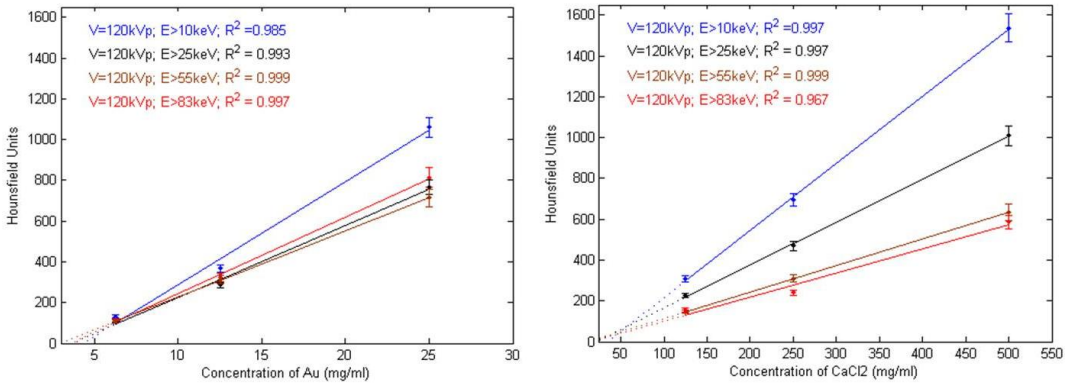

Figure 6.15 HU as a function of concentration. *Left:* linearity response of AuNPs over different concentrations. The linear fitted lines indicate correlation R^2 = 0.985 to 0.999 for all four threshold energies. *Right:* linearity profile of $CaCl_2$ is R^2 = 0.97 to 0.999.

Almost all CT slices have been analyzed for the three specimens. First the suspected regions have been identified and their attenuation profiles assessed. It was unfortunate that no single slice from the binding data set was found having AuNPs and calcification in the same image. Therefore, different CT slices with suspected regions in them have been compared.

The spectral response of CT slice 122 and CT slice 164 from specimen1 (incubated with non-binding AuNPs) having suspected regions A1 and B1 respectively (1 corresponds to specimen number) is shown in Figure 6.16. The attenuation profiles of these suspected regions was analyzed and compared with the known data set by plotting Hounsfield units as a function of energy, as shown in Figure 6.17. The solid lines correspond to known materials, whereas dashed lines represent the profile of suspected regions.

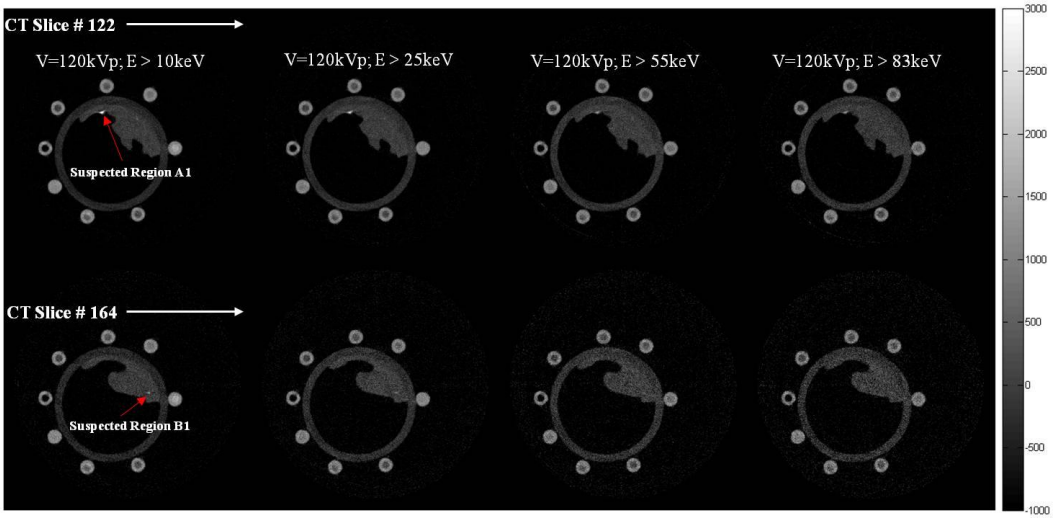

Figure 6.16 Two transverse slices (CT slice 122 and 164) of specimen1 with increasing threshold energies. Region A1 and B1 (1 corresponds to specimen number) from CT slice 122 and CT slice 164 respectively are observed as suspected regions (red arrow). The colour-map represents HU ranging from -1000 to 3000.

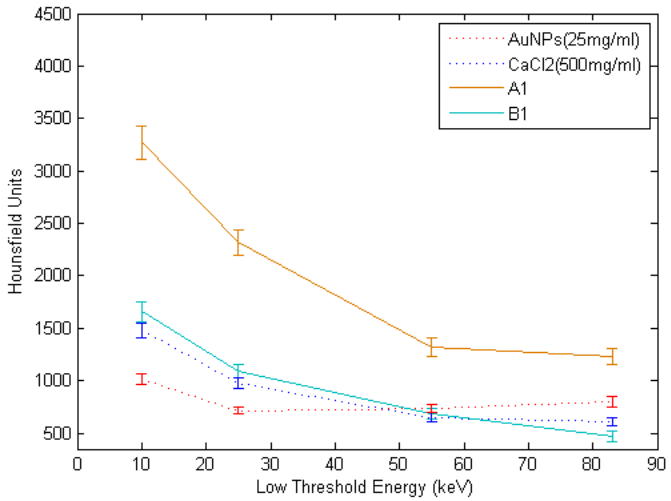

Figure 6.17 Attenuation profile of AuNPs (capillary tube), $CaCl_2$ (capillary tube) and two suspected regions. Both suspected regions A1 and B1 follow the trend of $CaCl_2$ which shows decreasing attenuation with increase in energy. Whereas, the HUs for AuNPs are high initially due to the influence of its L-edge, then decrease with energy, but increase again due to the influence of its K-edge at 80.7 keV.

For specimen2 (incubated with binding AuNPs), only one CT slice 101 was found to have suspected regions A2 and B2. Figure 6.18 and Figure 6.19 show the spectral and attenuation profiles of the suspected regions, respectively.

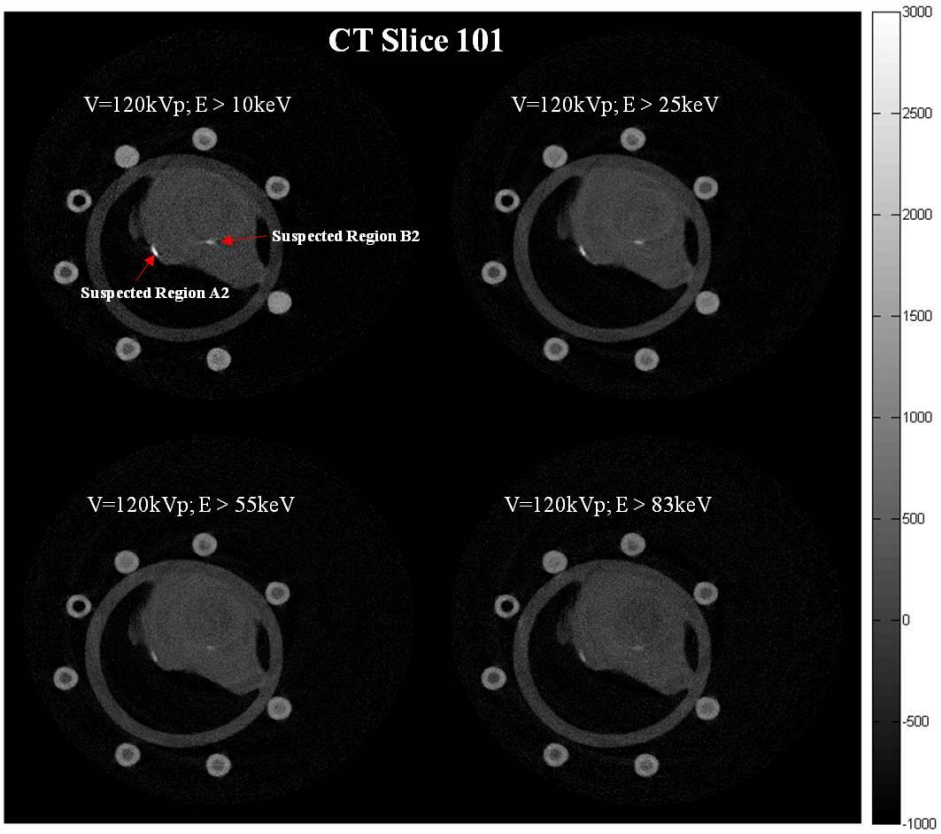

Figure 6.18 Transverse slice 101 of specimen2 with increasing threshold energies. Region A2 and B2 are observed as suspected regions. The colour-map represents HU ranging from -1000 to 3000.

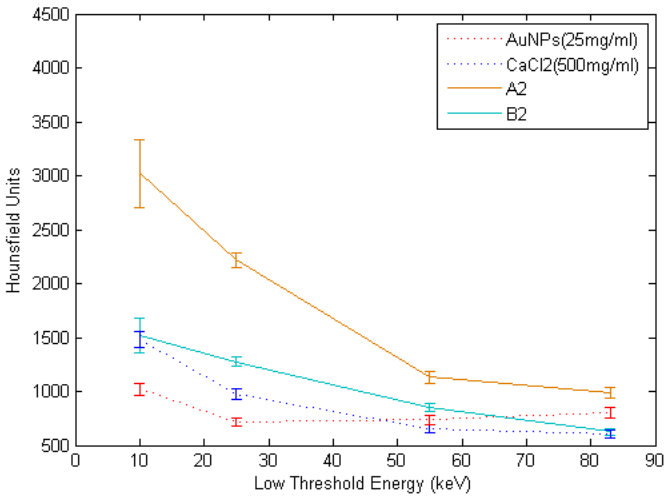

Figure 6.19 Attenuation comparison of suspected regions with known data set. Both suspected regions A2 and B2 are follow trend of $CaCl_2$ which shows decreasing attenuation with increase in energy. No gold is observed.

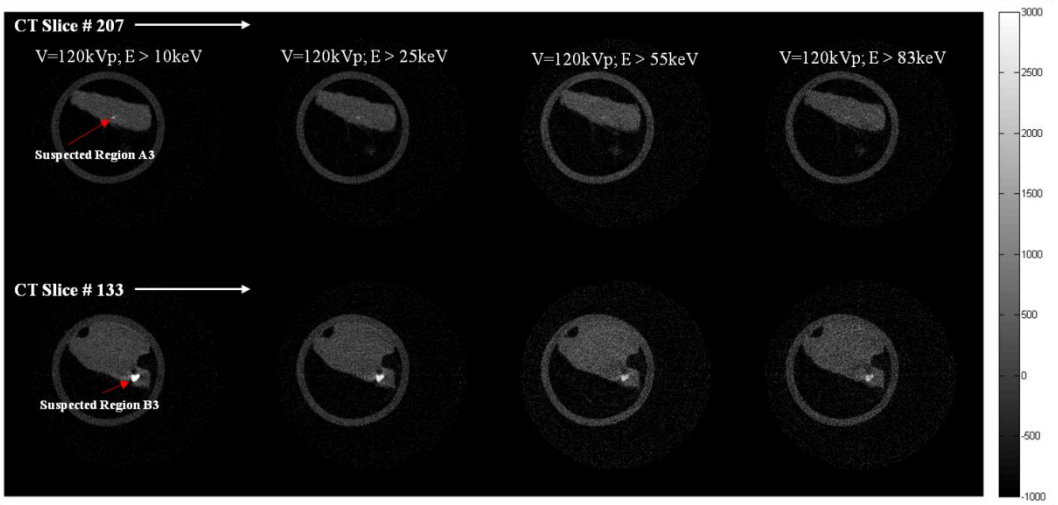

Figure 6.20 Region A3 and B3 from CT slice 207 and CT slice 133 respectively are observed as suspected regions. The colour-map represents HU ranging from -1000 to 3000.

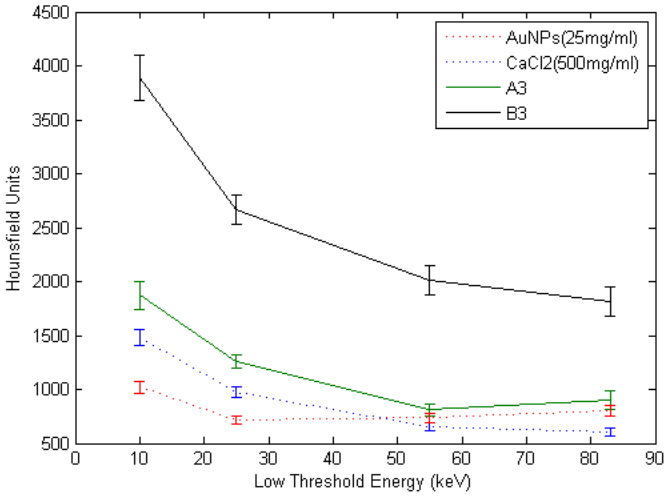

Figure 6.21 Attenuation comparison of suspected regions with known data set. Here suspected region B3 is following the trend of $CaCl_2$ whose HU decreases with increase in energy. It seems to be a highly calcified region due to its high HUs, whereas A3 follow the trend of AuNPs whose HUs are increasing at higher threshold energy due to the influence of the gold K-edge at 80.7 keV.

For Specimen3 (incubated with binding AuNPs), CT slice 207 and 133 were found to have regions A3 and B3. Figure 6.20 and Figure 6.21 show the spectral and attenuation profiles of suspected regions, respectively. From Figure 6.21, it is evident that region A3 has a profile similar to AuNPs but for more assurance, material decomposition

has been applied on both CT slices. Figure 6.22 and Figure 6.23 show the quantification of AuNPs, $CaCl_2$ and water in CT slice 207 and 133, respectively. There is some cross talk observed from the soft tissue signal (due to Compton Scattering) onto the gold image. However, this is not considered to be a problem as the material decomposition algorithm is currently in its development phase. It is expected that, in the near future, cross talk could be subtracted by comparing it with the soft tissue image.

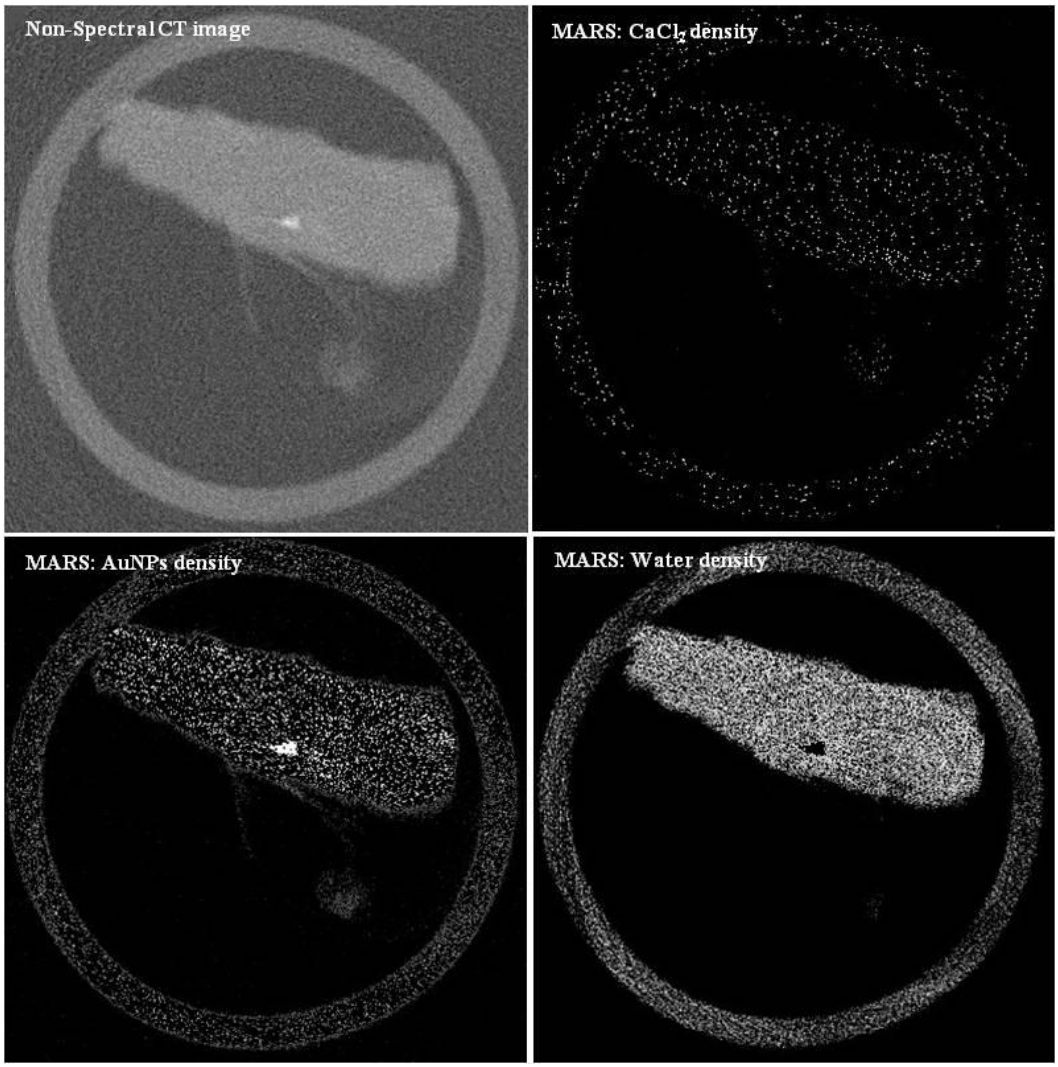

Figure 6.22 Classification of non-spectral CT image into individual elements. *Top (left to right)*: non-spectral CT image, image with only $CaCl_2$ density. *Bottom (left to right)*: image with Au density and image with only water.

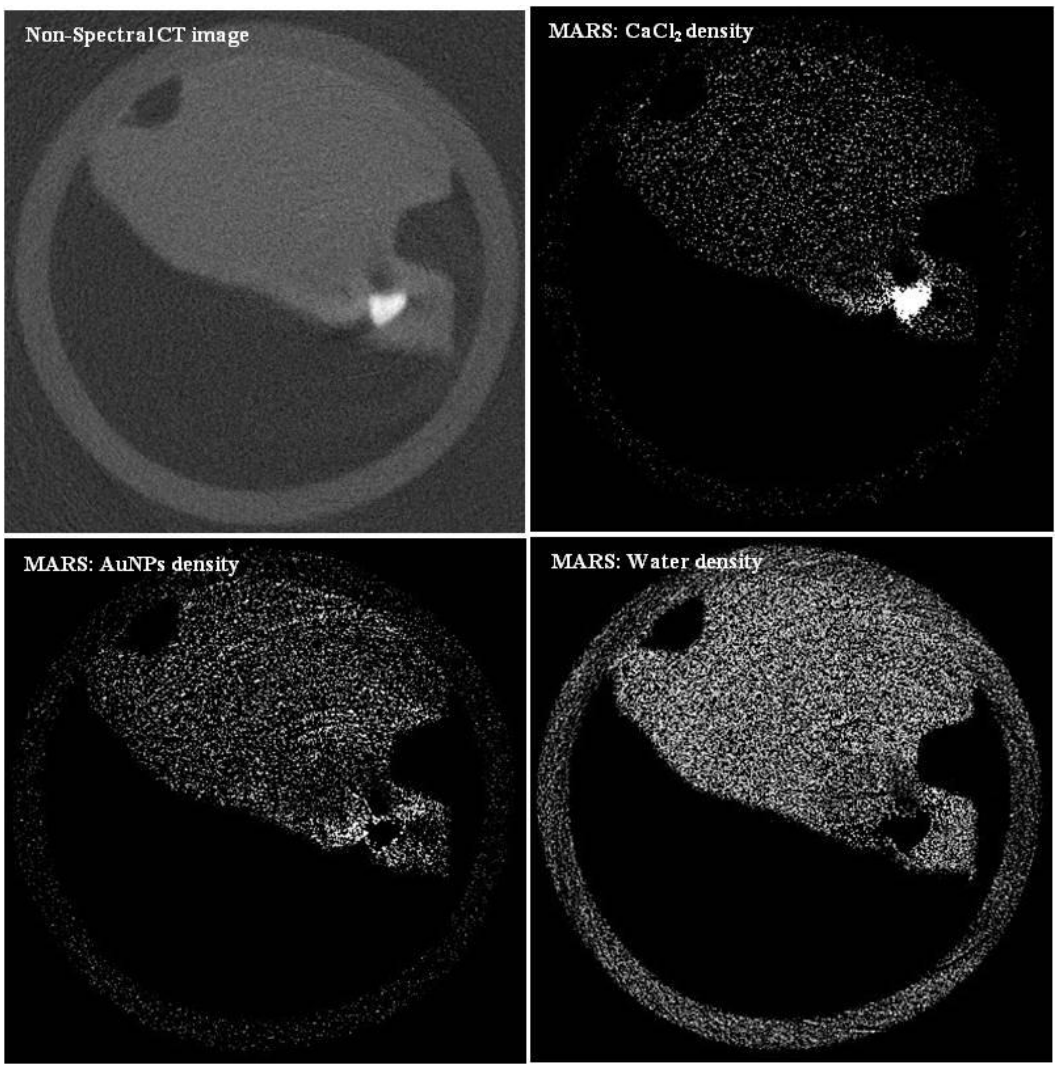

Figure 6.23 Classification of non-spectral CT image into individual elements. *Top (left to right)*: non-spectral CT image, image with only $CaCl_2$ density. *Bottom (left to right)*: image with Au density and image with only water.

To produce a colour (RGB) image from Figure 6.22, Au and water density images combine with the non-spectral CT image under the RGB protocol of imageJ software (ImageJ 2012) to produce Figure 6.24. Similarly, images of $CaCl_2$ and water density from Figure 6.23 combine with the non-spectral CT image to produce a colour image, as shown in Figure 6.25.

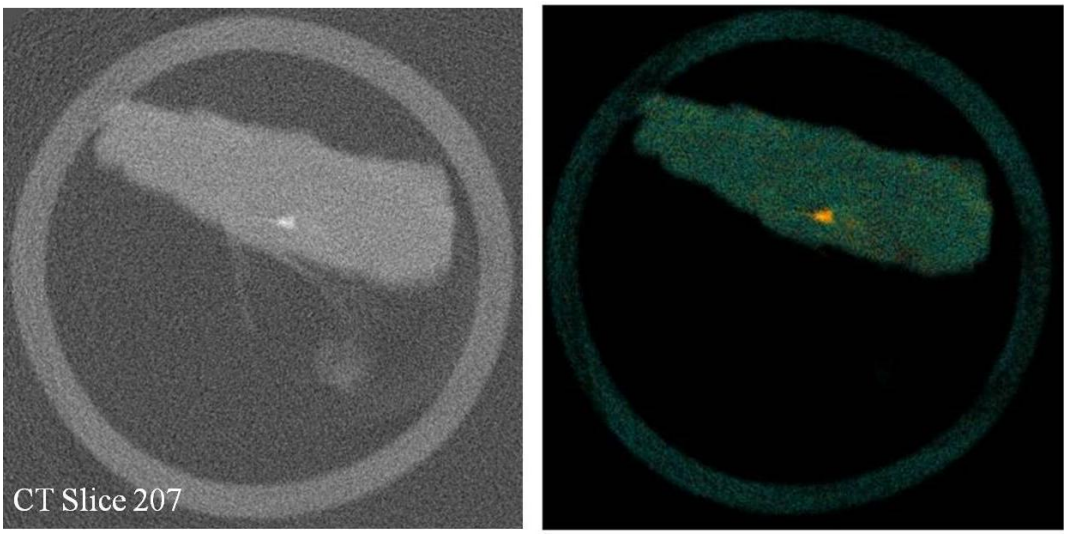

Figure 6.24 *Left*: non-spectral image of CT slice 207. *Right:* Combined RGB image of Au and water densities from the image on left. Specimen3 shows AuNPs attached to regions with platelet rich thrombi with plaque (green) differentiated from gold (yellow).

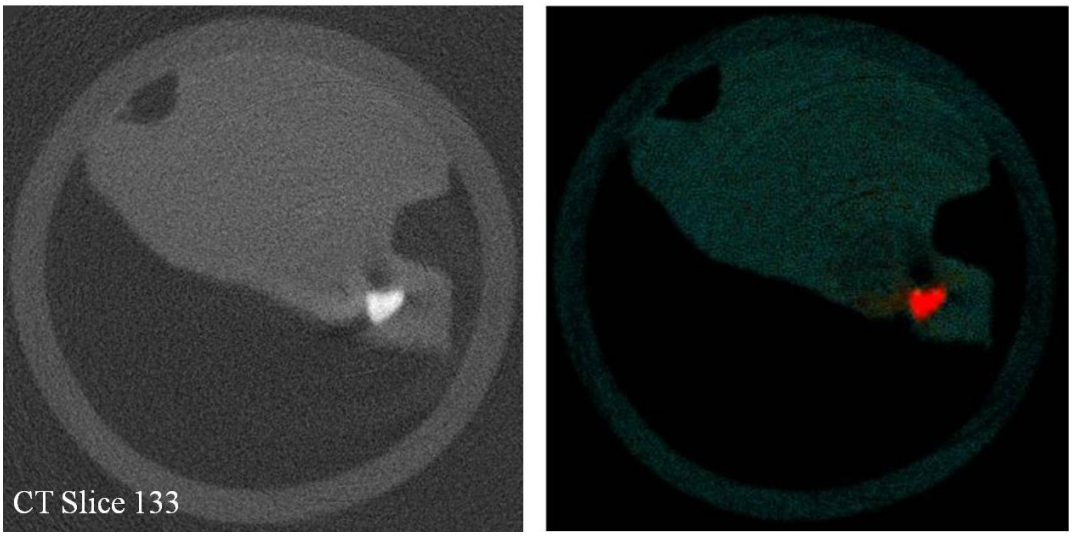

Figure 6.25 *Left*: non-spectral image of CT slice 133. *Right:* Combined RGB image of $CaCl_2$ and water densities from image on left.

6.6.2.4 Imaging of mouse tumour

To explore the architectural morphology of all tumours and expected accumulation of nanoparticles in tumour's core and periphery, every CT slice was

analyzed. Orthogonal views of CT images were also assessed side by side (see Figure 6.26) to identify any suspected regions within the tumour or outside the tumour.

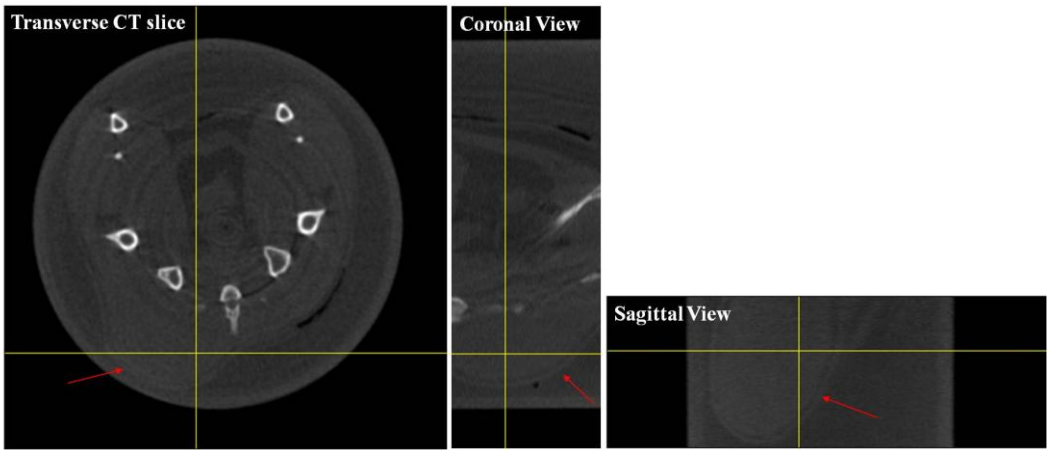

Figure 6.26 Randomly selected CT orthogonal views from one of the tumour mouse having AuNPs. Arrows are pointing the edge of the tumour in all images.

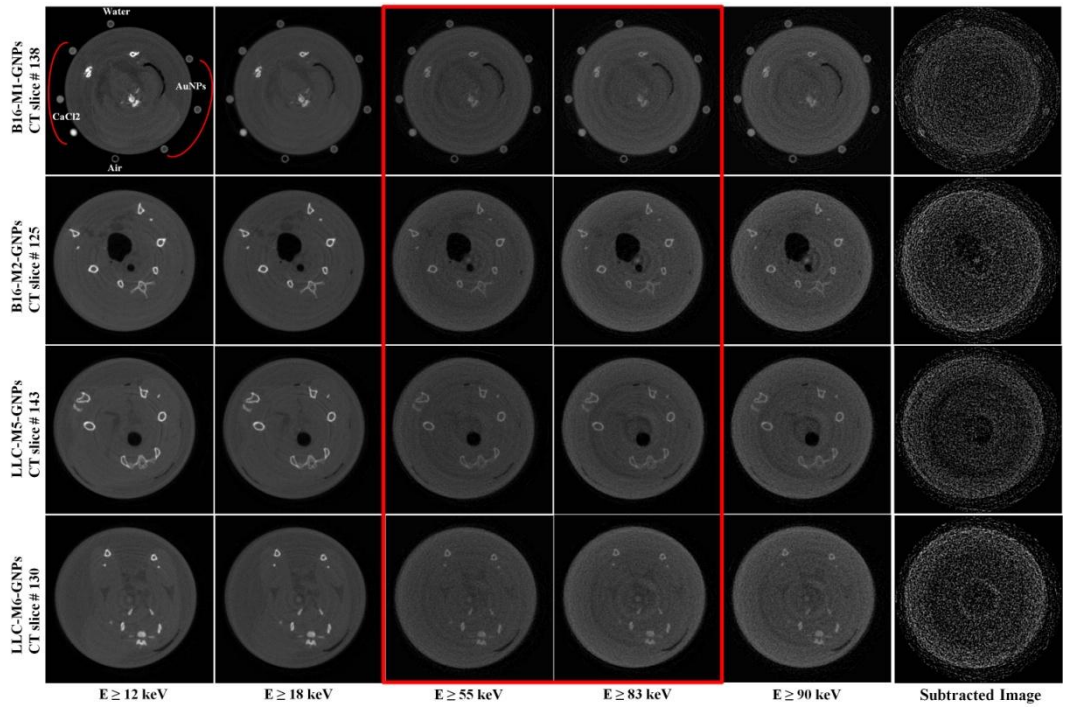

Figure 6.27 Images showing transverse slices of different mouse tumours injected with AuNPs. Since scanning conditions were the same, the capillary tube data from B16-M1-GNPs (top row) was used to calibrate the others in HU, using water and air regions. The images in the sixth column are subtracted images from red highlighted region (below and above gold's K-edge) showing the difference in HU. No presence of gold is observed in tumour regions of subtracted images.

In these experiments, nanoparticles are expected to accumulate in the tumour tissue via a phenomenon known as the enhanced permeability and retention (EPR) effect (see discussion). The dual-energy subtraction technique is used for visualising energy-dependent attenuation differences. Firstly, the spectral images were calibrated to HU, so that air corresponds to -1000 HU and water corresponds to 0 HU, then the difference between the high (above K-edge) and low (below K-edge) energy images were used to identify the contrast agent from the background structure. Figure 6.27 and Figure 6.28 shows the results of this dual-energy subtraction technique on AuNPs and AgNPs datasets respectively. However, no evidence of the accumulation of nanoparticles is observed in the subtracted images in either datasets.

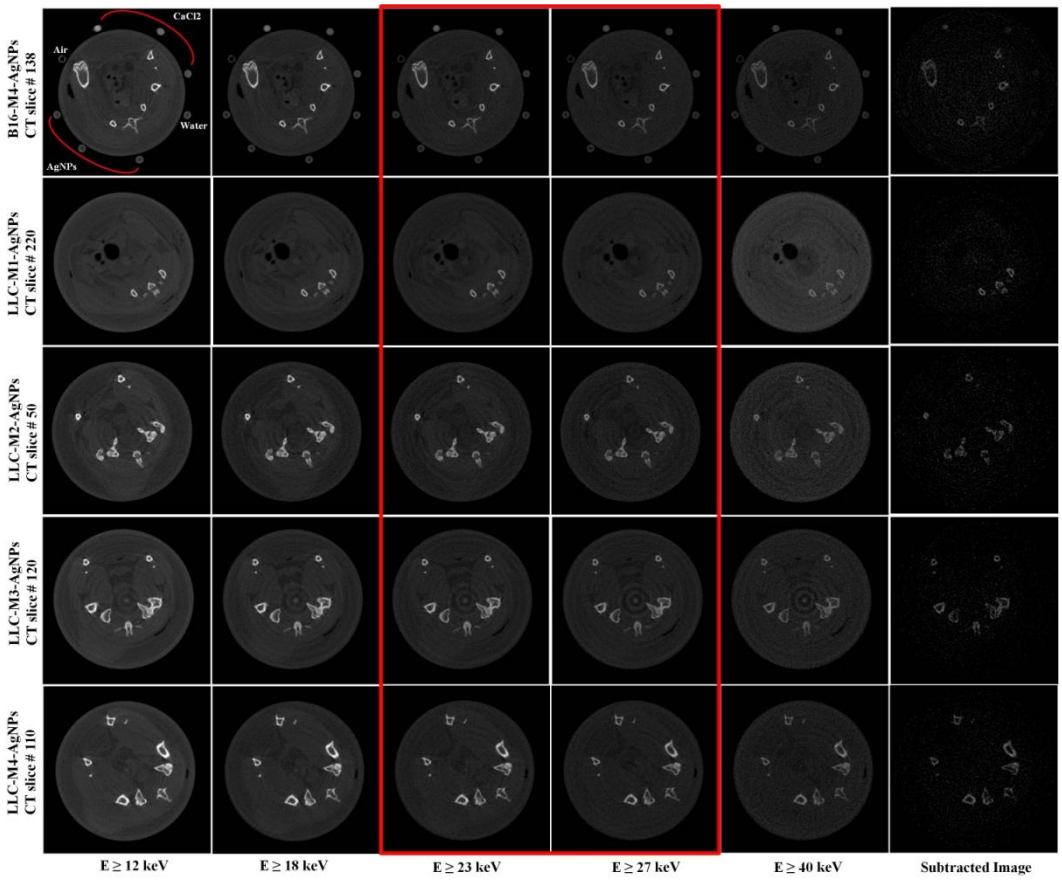

Figure 6.28 Images showing transverse slices of different mouse tumours injected with AgNPs. Since scanning conditions were the same, the capillary tube data from B16-M4-AgNPs (top row) was used to calibrate the others in HU, using water and air regions. The images in the sixth column are subtracted images from red highlighted region (below and above silver's K-edge) showing the difference in HU. No presence of silver is observed in tumour regions of subtracted images.

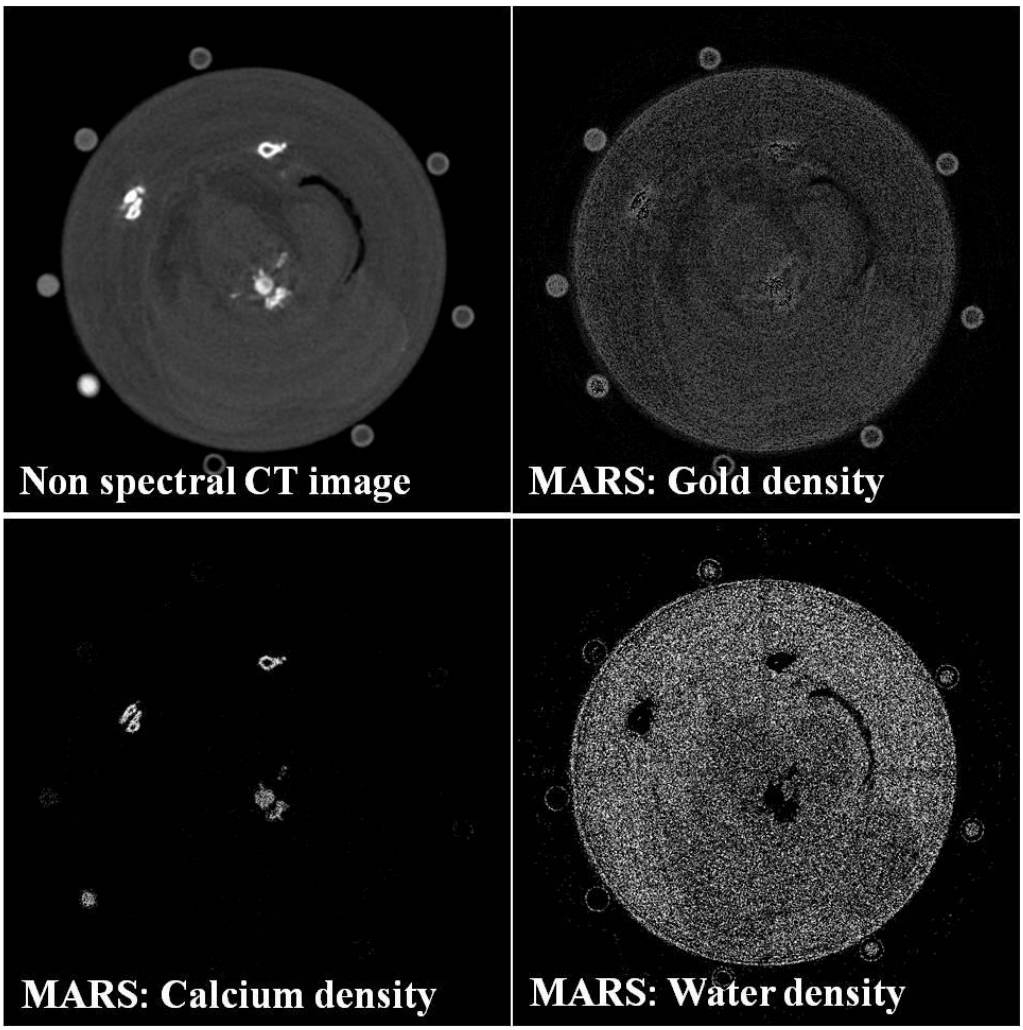

Figure 6.29 Classification of non-spectral CT image into individual elements. *Top (left to right)*: non-spectral CT image, image with only gold density. *Bottom (left to right)*: image with $CaCl_2$ density and image with only water.

The material decomposition technique is also applied as an alternative approach to dual-energy subtraction for imaging and visualizing differences in x-ray absorption. Figure 6.29 shows the quantification of AuNPs, $CaCl_2$ and water in CT slice 138 for one of the gold injected mouse tumours (B16-M1-GNPs). Figure 6.30 also shows AgNPs, $CaCl_2$ and water quantification in CT slice 138 for one of the silver injected mice (B16-M4-AgNPs). However, the material decomposition technique is also unable to quantify gold and silver densities from the spectral datasets, but $CaCl_2$ (refers bone density) and water densities are quantified nicely. Gold and silver density images are showing mostly cross talk from the soft tissue signal (Compton Scattering), which perhaps is an indicator

of the low concentration used in these experiments which will be discussed later in next section.

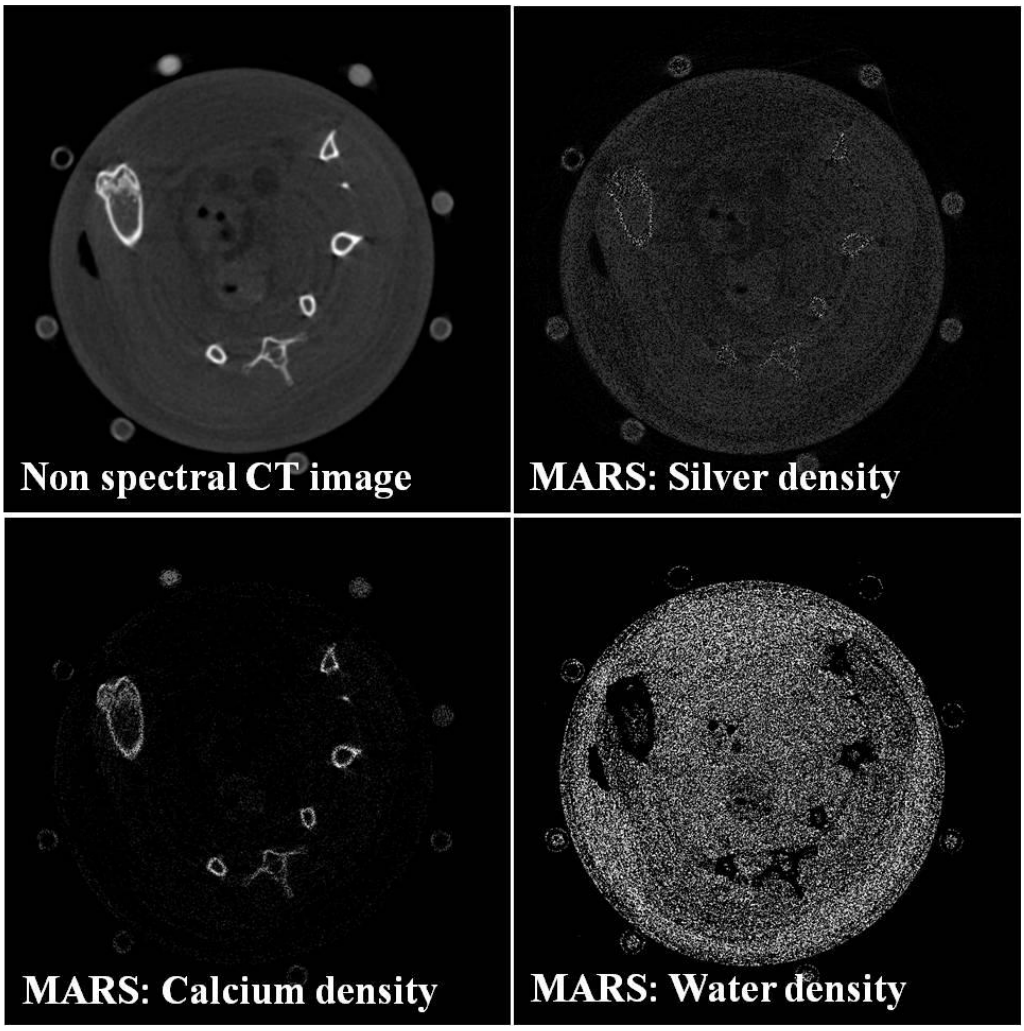

Figure 6.30 Classification of non-spectral CT image into individual elements. *Top (left to right)*: non-spectral CT image, image with only silver density. *Bottom (left to right)*: image with $CaCl_2$ density and image with only water.

6.6.3 Discussion

In these studies, high concentrations of contrast elements have been used deliberately to clearly demonstrate the proof of concepts with appropriate quantification. Detectable limits have also been measured (see Figure 6.15) for future studies with clinical relevance in which doses can be reduced many-fold.

6.6.3.1 Spectroscopic study with AuNPs

The study demonstrates the proof of concept: that the MARS-CT scanner, equipped with CdTe sensors and assembled with a Medipix2 camera, can discriminate between various high Z materials in the diagnostic energy range. We have shown simultaneous discrimination of six materials (AuNPs, Gadolinium, iodine, fat, water and air), and to our knowledge no one has performed a similar study at such scale. It shows that the x-ray photon attenuation is energy dependent and that each material has a specific attenuation curve. This also confirms that discrimination and classification of different materials is possible by spectral imaging. The most important aspect of this study is to demonstrate the potential benefit of Medipix detector in molecular imaging which is considered to be the future of spectral imaging.

Different tube voltages were used just to optimize the energy bins, resulting in reduced noise and less charge sharing. Thomas Koenig at the German Cancer Research Centre has also performed the similar study using my phantom with fixed kVp and with 165µm pixel pitch of hexa (3×2) CdTe assembled Medipix2 detector (under MARS collaboration). The study nicely captures the K-edges of three contrast elements (private communication).

6.6.3.2 Mouse study with AuNPs

After determining the optimum energy range for scanning high Z materials in a phantom study, the evaluation of in-vivo data sets was performed. Figure 6.11 to Figure 6.14 show the presence of AuNPs at different locations at different time intervals. The application of PCA to four grey-scale energy based images produce principal component images, what we display in RGB colours based on the spectral information.

The results of this experimental study demonstrate a successful development of the technique for in-vivo scanning of mice injected with AuNPs. The next step is to translate it to different mouse models e.g., tumour induced mouse models, to demonstrate the feasibility of quantifying macromolecular drug delivery by AuNPs. The goal is to demonstrate the non-invasive identification of tumour markers and drug markers labelled with non-toxic particles of gold.

6.6.3.3 Imaging of vulnerable plaque

The measured profile of contrast materials (AuNPs and $CaCl_2$) was observed to be consistent for all four energies i.e., R^2 = 0.97 to 0.999. This information has been used to correlate between known materials in the capillary tubes and the suspected regions. As expected, the results of specimen1 (incubated with non-binding AuNPs) show no sign of the presence of AuNPs but we can clearly observe the trend of suspected regions similar to calcium (see Figure 6.17). In specimen2 (incubated with binding AuNPs), calcium can be identified spectrally. No gold is present, but presumably this means that there may be few or no activated platelets (see Figure 6.19). Specimen3 (incubated with binding AuNPs) show both calcium (region B3 in CT slice 133) and gold (region A3 in CT slice 207). Both suspected regions are identifiable spectrally (Figure 6.21). Targeted particles mostly attach to the surface but plaques have micro-ruptures and there is a possibility for some of the particles to diffuse inside as shown in Figure 6.20.

To make sure about our findings, material decomposition was applied to decompose the CT image into individual basis, based on their spectral response. Figure 6.22 confirms the presence of AuNPs, whereas Figure 6.23 shows no gold in the suspected region. It is very difficult to correlate between the plaque photograph and the CT image as plaque segments have an irregular shape at the cutting edge. Also the orientation of the plaque specimen changes while placing the specimen inside the falcon tube, make it very difficult to compare the photograph with the CT image.

In this study, we have tested a method for vulnerable plaque assessment using MARS-CT. The idea of spectral imaging is not new (Alvarez and Macovski 1976), but what is new is the extension of the concept from spectral CT imaging to molecular imaging. The aim of the study was to demonstrate the presence of binding nanoparticles in regions with activated platelets of human plaque. We have shown that targeted AuNPs can be identified and quantified spectrally.

There are a few limitations on the biological side which are important to address: 1) it is difficult to determine the number of activated platelets in a specimen, 2) it is not clear how many antibodies are attached to one gold nano-particle or conversely (how many nanoparticles are attached to one antibody). The general assumption is 1 antibody

per particle but this is still not confirmed (private conversation with Baker IDI group, Australia), 3) it is not known how many antibodies attach to the desired site of the specimen, 4) it is not known how long antibodies attach to the platelet on the desired site, 5) it is not known what concentration of gold nanoparticles is required to saturate a human thrombus and 6) it is not known what the effect will be on the coverage of the cell's surface of incubating plaque samples, or on other models with different shapes and sizes of AuNPs (Vital Peretz 2012). These observations may not directly relate to the CT imaging or the physics side but they directly affect the sensitivity of the system due to specimen uptake. Note that for CT imaging, the total amount of gold per unit volume (voxel) is an important parameter, regardless of the shape and size of the particles (Popovtzer, Agrawal et al. 2008). Three samples were used, due to the limited availability of binding and non-binding AuNPs as well as limited samples having significant thrombosis. As mentioned previously, this experiment was performed in collaboration with Atherothrombosis and Vascular Laboratory, Baker IDI Heart and Diabetes Institute, Melbourne, Australia. The group has expertise in making antibody attached nanoparticles. The production of scFv with the AuNP is very expensive, therefore this study was an initial test of the technique and provides a proof of concept. We probably need to do a series of plaques for further development of this approach. Long term collaboration is already under way with Baker group.

6.6.3.4 Imaging of mouse tumour

In this study, low doses were used due to the limited availability of pegylated gold nanoparticles and the acute toxicity of silver nanoparticles. Silver nanoparticles (K-edge = 25.5 keV) are considered as good candidates for CT imaging. However there are few in vivo toxicity studies. These studies encouraged us use low concentrations (Xue, Zhang et al. 2012). While our study was not extensive, it showed the contrast/noise aspects of the nanoparticles as a contrast material, and showed that we could obtain clinical radiology level CT images that clearly discriminated nanoparticles in desired sites.

Mice were euthanized 24 hrs after the injection. The visualization of gold and silver nanoparticles has been assessed in two different types of tumours, at different tube voltages with multiple threshold energies. No evidence of the accumulation of particles

into tumour regions was observed in using any of the MARS team's multiple material analysis techniques. This is most likely due to the low doses of gold (~0.125 g Au per kilogram of body weight) and silver (~0.04 g Ag per kilogram of body weight) that were applied. The tumour signal (with nanoparticles) relative to the background (region other than tumour) was found almost equal. We have detected smaller quantities of gold-labelled anti-platelet antibodies in phantoms and in an excised human atheroma at a concentration of 4.4mg Au/ml (see Figure 5.15) and have already produced images of mouse kidneys. It is understood that the ability to discriminate high Z materials depends primarily on the concentration of the material. Injecting an appropriate concentration will increase the discrimination sensitivity of the system.

By using higher doses, Hainfield et al (Hainfeld JF 2011) showed the accumulation of AuNPs in a tumour's growing edge, as shown in Figure 6.31. Tobi et al (Tobi Reuveni 2011) also used higher dose of Au in their in vivo study of targeted AuNPs, as shown in Figure 6.32. They showed that active tumour targeting (with specific antibodies) is more efficient than passive targeting (with non specific antibodies).

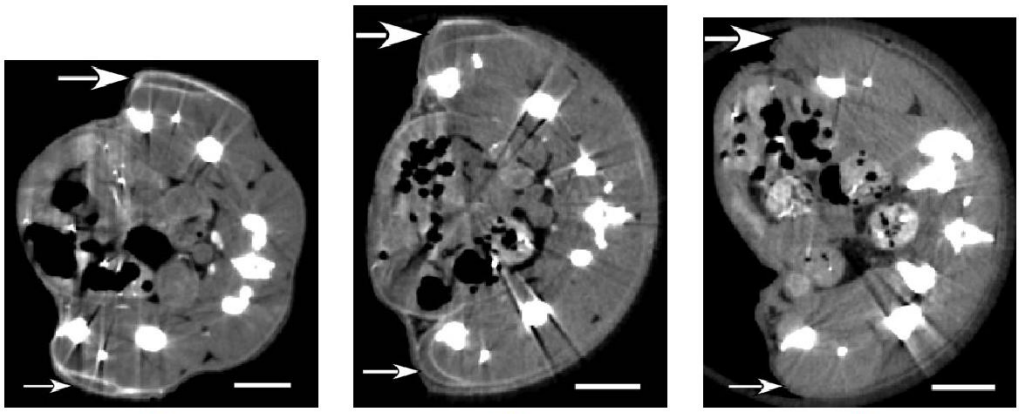

Figure 6.31 CT images of 20 hr post injection mice. Arrow shows (a) 15 nm AuNPs only; (b) 15 nm AuNPs conjugated to a non-specific antibody and (c) no AuNPs injected. Dose applied was 1.1 g Au Kg^{-1} (Hainfeld, Slatkin et al. 2006).

The tumours used in this study were between 350 mm^3 to 970 mm^3 in size, several fold larger than used by Hainfeld et al (~60 mm^3) and Tobi et al (< 80 mm^3). Tumour size could be another, and perhaps a major factor, of not having sufficient accumulation of particles within the tumours. As tumour size reaches about 150–200 μm,

they start developing their own blood vessels to supply nutrients such as oxygen and glucose. Healthy blood vessels (normal vascular physiology) have tight (2–6 nm) endothelial junctions (interior surface of blood vessel), which will restrict nanoparticle distribution, whereas a defective endothelium layer leads to large gaps (few hundred nanometres to a few micrometer) that allow nanoparticles to accumulate in tumour tissue. The nanoparticles extravasations in the tumour cells increase with time in a matter of several hours. This phenomenon of selective accumulation of nanoparticles into tumour tissues is known as the Enhanced Permeability and Retention effect (EPR) (Greish 2012). This phenomenon helps nanoparticles to concentrate most readily in tumour areas with the best blood supply. Large tumour size results in tumour necrosis (dying stage of cells), and causes poor central circulation. High interstitial pressure also limits nanoparticle transport in the tumour (Soltani and Chen 2012). Other factors discussed in section 6.4, may also have prevented sufficient nanoparticles to accumulate in the tumour tissues.

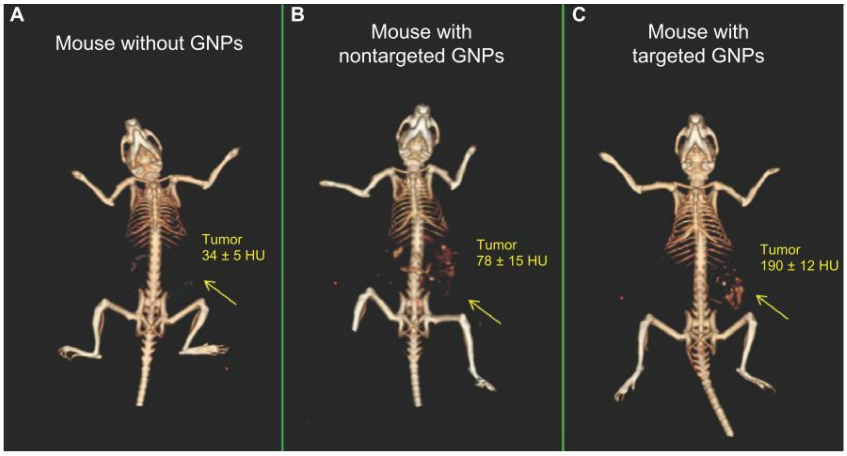

Figure 6.32 Computed tomography volume rendered images of (A) no AuNPs; (B) mouse with 6 hrs post injection of AuNPs with passive targeting and (C) mouse with 6 hrs post injection of AuNPs with active targeting. CT numbers represents the HU of the whole tumour area. Dose applied was ~0.25 g Au Kg^{-1} (Tobi Reuveni 2011).

To overcome these problems, it is important to know the tumour topology. Small tumours should be used as it is critical to detect tumours before they grow large enough to metastasis. The total dose of gold is not limited by its toxicity; rather the limit is the volume that can be injected at any one time. Multiple doses of gold over time can be given to increase the concentration without clearing it out. We could also consider removing a tumour and doing another form of testing to measure the actual gold

concentration achieved in the tumours, similar to comparative fluorescent optical quantitative imaging.

6.7 Summary

In this chapter, we have discussed the limitations of the current contrast agents for CT, especially the shortcomings of iodine in molecular imaging. It is desirable to deliver the contrast material with targeted antibodies to desired sites at detectable concentrations, however current iodine agents result in poor contrast visibility between the small vessels and the tissue surrounding the vessels in many patients. Unlike iodine, gold has very low viscosity and osmolality; it also delivers more gold atoms per molecule than iodine and therefore can be used in small blood vessels without risk of vascular damage. Gold nanoparticle agents provide a high degree of flexibility in terms of functional groups for coating and targeting. Therefore, it can be bound to drugs, targeted to tumour biomarkers, or added to antibodies to attach at desired sites.

Simultaneous discrimination of six materials (AuNPs, gadolinium, iodine, fat, water and air) in the diagnostic energy range demonstrates the potential benefit of Medipix detectors in molecular imaging. A successful development of the technique for in-vivo scanning of mice injected with AuNPs is translatable to different mouse models. Despite of a few limitations from biological side the presence of binding nanoparticles in regions with activated platelets of human plaque was shown. In imaging mice tumours, though the results are not positive, a brief comparison of experiments with previously published images has been done. The probable reason for our failure to observe the gold nanoparticles is thought to be too low a concentration and bigger tumours.

7 Conclusion

This thesis has presented an overview of the candidate's contribution to the development of various MARS spectral CT scanners; especially it demonstrates the feasibility of their molecular imaging feature. The scientific outcomes of candidate's research have already been listed in terms of publications (see Academic contribution). A brief description of MARS CT systems, the concept of the spectral CT imaging using Medipix x-ray detectors, and some of its benefits over conventional CT and dual energy CT has been discussed and reviewed. The utility of MARS CT scanners for molecular imaging has been demonstrated. It is shown that the scanner can identify both drug markers and stenosis of atherosclerosis labelled with non-toxic nanoparticles. It is also shown that spectral computed tomography, using MARS scanners, can give quantitative measurements of concentrations of gold nanoparticles in phantoms, mice and excised atheroma.

The characterization of a 300-µm-thick Si and 1 mm thick CdTe sensor bump bonded to a Medipix2 chip has been discussed. I have analyzed the sensitivity of 65,536 pixels in Si and 131,072 pixels in CdTe over a hundred frames. A high degree of repeatability is shown across one hundred consecutive exposures. With the detectors tested, about 0.02 % pixels in Si and ~ 0.7 % pixels in dual CdTe are found to be dead (giving zero counts). Both detectors at higher tube currents are observed to saturate. From the mechanical aspect, the dead region of ~1.238 mm (~23 pixels) between dual CdTe chips is one of the leading causes of undesirably long scans. Another reason for long scans is the saturation of CdTe semiconductor material at high fluxes which limits the detector operation at high tube currents. A possible reason for the saturation of the sensors at high photon fluxes could be sensor pulse pileup or ASIC pileup. The effect of charge sharing on the performance of Medipix2 is another factor which compromises energy resolution much more than spatial resolution. The Medipix3 chip has overcome some of the causes leading to long scans by the simultaneous measurement of 8 energy bins. It also has the capability of a charge sharing correction. The largest remaining cause, the stop-start motion of the gantry between images, has since been resolved by the MARS team members working on the robotic aspects of the software. Finally, I have performed a

flat field correction and have demonstrated the improvement this has on the image quality.

After the characterization of the Medipix detectors, the geometrical quality assurance routines for MARS-CT scanners have been established by fabricating customized phantoms. Motor driven movements have been plotted to check the measured displacement against corresponding index values, determining key parameters such as source-to-detector and source-to-object distances. The system performance is evaluated in terms of spatial resolution, linearity response, spectroscopic discrimination response and the quality imaging of biological samples. Overall, a spatial resolution of ~165μm with good linearity response and spectroscopic discrimination has been shown by using CdTe-Medipix2. Ring artefacts were observed in almost all data sets. The major cause of these artefacts is the pixel variations, which were not compensated by the flat-field protocol used. Latest version of Medipix (Medipix3.2 also known as Medipix3RX) has improved inter pixel communication which will minimize these problems and while writing this, preliminary testing is being done by one of the MARS group members.

The thesis also demonstrates proof of the concept: that the MARS-CT scanner, equipped with CdTe sensors assembled with a Medipix2 camera, can discriminate among low Z materials, and from various concentrations of high Z materials in the diagnostic energy range. I have shown simultaneous discrimination of six materials (AuNPs, gadolinium, iodine, fat, water and air). This confirms the potential benefit of Medipix detector in molecular imaging which is considered to be the future of spectral imaging. I have also demonstrated a successful development of the technique for the in-vivo scanning of mice injected with AuNPs which can be translated to different mouse models e.g., tumour induced mouse models. The molecular imaging feature of MARS CT scanners is assessed using gold nanoparticles attached to antibodies that targeted to thrombotic events in excised plaque. It is shown that targeted AuNPs can be identified and quantified spectrally. Proof of principle give the concept that spectral CT imaging should be able to perform the molecular imaging required for non-invasive assessment of vulnerable plaque (the major reason for heart attack and stroke). Gold nanoparticles were also used for non-invasive quantification of macromolecular drug delivery in mouse cancer models. The ability to non-invasively image and quantify drug delivery into tumours has direct relevance to cancer treatment, as it provides an imaging method for

longitudinal studies of efficacy of drug therapy, and provides a tool for rapid drug development. The limitations of this study were mostly observed from the biological side, that is, it is not directly related to the CT imaging (the physics side). Rather it indirectly affects the sensitivity of the system due to low specimen uptake. In particular, the large tumour sizes and low applied doses of gold (~0.125 g Au per kilogram of body weight) could be the major factors for not getting any evidence of the accumulation of particles into tumour regions.

The results have strong health significance. Vulnerable plaque poses a very high risk for stroke and myocardial infarction. Plaque vulnerability is critical for preventing the severe effects of heart disease. Although the inflammatory status of the atherosclerotic plaque may be imaged by a combination of different imaging methods, it would be best to have a single imaging modality. MARS Spectral CT has the potential to quantify the biological processes taking place at the molecular and cellular level by using biomarkers. Such biomarkers advance CT imaging from an anatomical imaging modality into a physiological imaging modality. We have demonstrated that we can see the labelled activated platelets in human plaque using x-ray parameters that translate to human imaging. For further development of this approach we need to do a series of plaque scans, e.g., 10 samples with binding antibodies and 10 samples with non-binding antibodies.

In imaging mouse tumours, though the results are not positive, a brief comparison of experiments with previously published images has been done. The probable reason for our failure to observe the gold nanoparticles is thought to be too low a concentration. The ongoing questions regarding the ability to visualize biological processes at the molecular and cellular level for non-invasive quantification of macromolecular drug delivery in mice cancer models by using nanoparticles in MARS scanner have been answered.

In future, live animal imaging studies can be performed by additional work in terms of continuous development of scanner which includes continuous and faster gantry rotation, improved detector performance, faster read-out, improved semiconductor performance, iterative reconstruction algorithms etc. Scanner calibration protocols and post processing routines are also need to be revised to minimize system and software related artefacts respectively. With small pixels, charge sharing in Medipix2 based detectors counts an artificially high number of photons with an incorrect energy

assignment and affects the overall energy resolution. Charge summing mode in Medipix3 is designed to resolve this problem but has not yet fully implemented. To explore full spectroscopic molecular imaging by MARS scanners, energy calibration of the Medipix detectors and their optimization need to be performed at the individual pixel level. CdTe versions of Medipix efficiently measure photons up to 120 keV and have similar detection efficiency to most other x-ray detectors used in CT. This energy range is also suitable for human imaging, enabling an eventual translation of this program's work into spectral molecular human imaging.

REFERENCES

Aamir, R., N. G. Anderson, et al. (2011). Characterization of Si and CdTe sensor layers in Medipix assemblies using a microfocus x-ray source. Nuclear Science Symposium and Medical Imaging Conference (NSS/MIC), 2011 IEEE.

Aamir, R., S. P. Lansley, et al. (2010). "Pixel sensitivity variations in a CdTe-Medipix2 detector using poly-energetic x-rays." Journal of Instrumentation **6**(01): C01059.

Abrosimov, N. V., S. N. Rossolenko, et al. (1997). "Czochralski growth of Si- and Ge-rich SiGe single crystals." Journal of Crystal Growth **174**(1): 182-186.

Achenbach S, A. K., Kalender WA (2008). "Dual-source cardiac computed tomography: image quality and dose considerations " Eur Radiol **18**: 1188-1198.

Acrorad. "***http://www.acrorad.co.jp/us/index.html***."

Alvarez, R. E. and A. Macovski (1976). "Energy-selective reconstructions in X-ray computerised tomography." Physics in Medicine and Biology **21**(5): 733.

Anas, E. M. A., S. Y. Lee, et al. (2010). "Removal of ring artifacts in CT imaging through detection and correction of stripes in the sinogram." Physics in Medicine and Biology **55**(22): 6911.

Anderson, N., A. Butler, et al. (2010). "Spectroscopic (multi-energy) CT distinguishes iodine and barium contrast material in MICE." European Radiology **20**(9): 2126-2134.

Badea, C. T., S. M. Johnston, et al. (2011). "Dual-energy micro-CT imaging for differentiation of iodine- and gold-based nanoparticles." Medical Imaging 2011: Physics of Medical Imaging **7961**: 79611X-10.

Ballabriga, R., M. Campbell, et al. (2006). The Medipix3 Prototype, a Pixel Readout Chip Working in Single Photon Counting Mode with Improved Spectrometric Performance. Nuclear Science Symposium Conference Record, 2006. IEEE.

Barber, W. C., E. Nygard, et al. (2009). Characterization of a novel photon counting detector for clinical CT: count rate, energy resolution, and noise performance. Medical Imaging 2009: Physics of Medical Imaging, Lake Buena Vista, FL, USA, SPIE.

Barreto, J. A., W. O'Malley, et al. (2011). "Nanomaterials: Applications in Cancer Imaging and Therapy." Advanced Materials **23**(12): H18-H40.

Barrett, J. F. and N. Keat (2004). "Artifacts in CT: Recognition and Avoidance1." Radiographics **24**(6): 1679-1691.

Bartling, S. H., W. Stiller, et al. (2007). "Small Animal Computed Tomography Imaging." Current Medical Imaging Reviews **3**(1): 45-59.

Boote, E., G. Fent, et al. (2010). "Gold Nanoparticle Contrast in a Phantom and Juvenile Swine: Models for Molecular Imaging of Human Organs using X-ray Computed Tomography." Academic Radiology **17**(4): 410-417.

Braun, H., Y. Kyriakou, et al. (2010). "The influence of the heel effect in cone-beam computed tomography: artifacts in standard and novel geometries and their correction." Physics in Medicine and Biology **55**(19): 6005.

Brenner, D. J. and E. J. Hall (2007). "Computed Tomography — An Increasing Source of Radiation Exposure." New England Journal of Medicine **357**(22): 2277-2284.

Brixner, L. H. (1987). "New X-ray phosphors." Materials Chemistry and Physics **16**(3–4): 253-281.

Buis, C., E. Gros d'aillon, et al. (2011). Effects of dislocation walls on the performance of cadmium telluride X-ray detectors. Nuclear Science Symposium and Medical Imaging Conference (NSS/MIC), 2011 IEEE.

Bushberg, J. T. (1998). "The AAPM/RSNA physics tutorial for residents. X-ray interactions." Radiographics **18**(2): 457-468.

Butler, A. P. H., N. G. Anderson, et al. (2008). "Bio-medical X-ray imaging with spectroscopic pixel detectors." Nuclear Instruments and Methods in Physics Research Section A: Accelerators, Spectrometers, Detectors and Associated Equipment **591**(1): 141-146.

Butler, A. P. H., J. Butzer, et al. (2011). "Processing of spectral X-ray data with principal components analysis." Nuclear Instruments and Methods in Physics Research Section A: Accelerators, Spectrometers, Detectors and Associated Equipment **633, Supplement 1**(0): S140-S142.

Butler, P. H., A. J. Bell, et al. (2008). Applying CERN's detector technology to health: MARS Biomedical 3D spectroscopic x-ray imaging. International Symposium on Peaceful Applications of Nuclear Technologies in the GCC Countries. Jeddah, University of Canterbury. Physics and Astronomy.

Butzer, J. S. (2009). MARS-CT: Biomedical Spectral x-ray imaging with Medipix. Karlsruhe, Karlsruhe Institute of Technology. **M.Sc Thesis**.

Cai, Q.-Y., S. H. Kim, et al. (2007). "Colloidal Gold Nanoparticles as a Blood-Pool Contrast Agent for X-ray Computed Tomography in Mice." Investigative Radiology **42**(12): 797-806 10.1097/RLI.0b013e31811ecdcd.

Cai, W., T. Gao, et al. (2008). "Applications of gold nanoparticles in cancer nanotechnology." Nanotechnology, Science and Applications **2008**: 17-32.

Campbell, M. (2010). "10 years of the Medipix2 Collaboration." Nuclear Instruments and Methods in Physics Research Section A: Accelerators, Spectrometers, Detectors and Associated Equipment **633, Supplement 1**(0): S1-S10.

Campbell, M., E. H. M. Heijne, et al. (1998). "A readout chip for a 64×64 pixel matrix with 15-bit single photon counting." Nuclear Science, IEEE Transactions on **45**(3): 751-753.

Campbell. M, H. E. H. M., Jarron. P, Krummenacher.F, Enz. C. C, Declercq. M, Vittoz. E and Viertel. G. (1990). "A 10 MHz Micropower CMOS Analog Front-End for Direct Readout Pixel Detectors." Nuclear Instruments and Methods in Physics Research **A290**: 149-157.

Chmeissani, M. and B. Mikulec (2001). "Performance limits of a single photon counting pixel system." Nuclear Instruments and Methods in Physics Research Section A: Accelerators, Spectrometers, Detectors and Associated Equipment **460**(1): 81-90.

Crooke, M. (2007). "New Zealand Cardiovascular Guidelines: Best Practice Evidence-based Guideline: The Assessment and Management of Cardiovascular Risk December 2003." Clin Biochem Rev **28**(1): 19-29.

Daruwalla, J., M. Nikfarjam, et al. (2010). "In vitro and in vivo evaluation of tumor targeting styrene-maleic acid copolymer-pirarubicin micelles: Survival improvement and inhibition of liver metastases." Cancer Science **101**(8): 1866-1874.

Del Sordo, S., L. Abbene, et al. (2009). "Progress in the Development of CdTe and CdZnTe Semiconductor Radiation Detectors for Astrophysical and Medical Applications." Sensors **9**(5): 3491-3526.

Dierick, M., B. Masschaele, et al. (2004). "Octopus, a fast and user-friendly tomographic reconstruction package developed in LabViewÂ®." Measurement Science and Technology **15**(7): 1366.

Doesburg, R. M. N. (2012). The MARS photon processing cameras for Spectral CT. Physics & Astronomy. Christchurch, University of Canterbury. **PhD Thesis**.

E1695, A. S. (2006). Standard Test Method for Measurement of Computed Tomography (CT) System Performance. West Conshohocken, PA, ASTM International.

Ferrari, M. (2005). "Cancer nanotechnology: opportunities and challenges." Nat Rev Cancer **5**(3).

Flohr, T., C. McCollough, et al. (2006). "First performance evaluation of a dual-source CT (DSCT) system." European Radiology **16**(6): 1405-1405.

Fornaro, J., S. Leschka, et al. (2011). "Dual- and multi-energy CT: approach to functional imaging." Insights into Imaging **2**(2): 149-159.

Frallicciardi, P. M., J. Jakubek, et al. (2009). "Comparison of single-photon counting and charge-integrating detectors for X-ray high-resolution imaging of small biological objects." Nuclear Instruments and Methods in Physics Research Section A: Accelerators, Spectrometers, Detectors and Associated Equipment **607**(1): 221-222.

Frey, E. C., X., et al. (2007). Investigation of the use of photon counting x-ray detectors with energy discrimination capability for material decomposition in micro-computed tomography. Society of Photo-Optical Instrumentation Engineers (SPIE) Conference Series.

Fujita, K., K. Matsue, et al. (2011). "Development of CdTe hybrid detector with CMOS charge integration amplifier." Nuclear Instruments and Methods in Physics Research Section A: Accelerators, Spectrometers, Detectors and Associated Equipment **636**(1, Supplement): S222-S225.

Gao, J., H. Gu, et al. (2009). "Multifunctional Magnetic Nanoparticles: Design, Synthesis, and Biomedical Applications." Accounts of Chemical Research **42**(8): 1097-1107.

Gormley, A. J., K. Greish, et al. (2011). "Gold nanorod mediated plasmonic photothermal therapy: A tool to enhance macromolecular delivery." International Journal of Pharmaceutics **415**(1–2): 315-318.

Graser, A., T. C. Johnson, et al. (2009). "Dual energy CT: preliminary observations and potential clinical applications in the abdomen." European Radiology **19**(1): 13-23.

Greiffenberg, D. (2011). Characterization of CdTe-Medipix2 detector. Physics Department. Freiburg, University of Freiburg, Germany. **PhD**.

Greish, K. (2012). "Enhanced permeability and retention effect for selective targeting of anticancer nanomedicine: are we there yet?" Drug Discovery Today: Technologies **9**(2): e161-e166.

Greish, K., J. Fang, et al. (2003). "Macromolecular Therapeutics: Advantages and Prospects with Special Emphasis on Solid Tumour Targeting." Clinical Pharmacokinetics **42**(13): 1089-1105.

Grossman, J. H. and S. E. McNeil (2012). "Nanotechnology in Cancer Medicine." Physics Today **65**(8): 38-42.

H. Zeller, S. D., M. Clark, P.H. Butler, A.P.H. Butler, N. Cook, L. Tlustos (2009). Charge sharing between pixels in the spectral Medipix2 x-ray detector. Image and Vision Computing New Zealand, 2009, 'IVCNZ '09.

Hainfeld JF, O. C. M., Dilmanian FA, Slatkin DN, Adams DJ, Smilowitz HM. (2011). "Micro-CT enables microlocalisation and quantification of Her2-targeted gold nanoparticles within tumour regions." Br J Radio **84**(1002).

Hainfeld, J. F., D. N. Slatkin, et al. (2006). "Gold nanoparticles: a new X-ray contrast agent." British Journal of Radiology **79**(939): 248-253.

Hay, D. (2004). "http://www.heartfoundation.org.nz/know-the-facts/statistics." 2012.

Health, M. o. (2011, 02 June 2011). "Cancer: New registrations and deaths 2008." 2012, from http://www.health.govt.nz/publication/cancer-new-registrations-and-deaths-2008.

Heikkinen, H., A. Gadda, et al. (2011). Low-temperature bump bonding of Timepix readout chips and CdTe sensors at Different Sensor pitches. Nuclear Science Symposium and Medical Imaging Conference (NSS/MIC), 2011 IEEE.

Hounsfield, G. N. (1973). "Computerized transverse axial scanning (tomography): Part 1. Description of system." British Journal of Radiology **46**(552): 1016-1022.

Hsieh, J. (2003). Computed Tomography: Principles, Design, Artifacts, and Recent Advances. Washington, USA, SPIE Press.

ImageJ (2012). from http://rsb.info.nih.gov/ij/.

J. T. Bushberg, J. A. S., E. M. Leidholt, Jr., and J. M. Boone, (2002). The Essential Physics of Medical Imaging. Philadelphia, Lippincott Williams Wilkins.

Jackson, P. A., W. N. W. A. Rahman, et al. (2010). "Potential dependent superiority of gold nanoparticles in comparison to iodinated contrast agents." European journal of radiology **75**(1): 104-109.

Jakubek (2007). "Data processing and image reconstruction methods for pixel detectors." Nuclear Instruments and Methods in Physics Research Section A: Accelerators, Spectrometers, Detectors and Associated Equipment **576**(1): 223-234.

Jakubek (2009). "Energy-sensitive X-ray radiography and charge sharing effect in pixelated detector." Nuclear Instruments and Methods in Physics Research Section A: Accelerators, Spectrometers, Detectors and Associated Equipment **607**(1): 192-195.

Jurgen, G. (2005). "Medical quantum X-ray imaging with 2D detectors." Nuclear Instruments and Methods in Physics Research Section A: Accelerators, Spectrometers, Detectors and Associated Equipment **551**(1): 125-138.

Kachelrieß, M., W. Semmler, et al. (2008). Micro-CT
Molecular Imaging I, Springer Berlin Heidelberg. **185/1:** 23-52.

Kedar, U., P. Phutane, et al. (2010). "Advances in polymeric micelles for drug delivery and tumor targeting." Nanomedicine : nanotechnology, biology, and medicine **6**(6): 714-729.

Khan, F. M. (2003). The Physics of radiation therapy. Philadelphia, Lippincott Williams & Wilkins.

Kirpotin, D. B., D. C. Drummond, et al. (2006). "Antibody Targeting of Long-Circulating Lipidic Nanoparticles Does Not Increase Tumor Localization but Does Increase Internalization in Animal Models." Cancer Research **66**(13): 6732-6740.

Koenig, T. (2011). Exploring Coherent Phenomena and Energy Discrimination in x-ray Imaging. Natural Sciences. Heidelberg, University of Heidelberg, Germany. **PhD Thesis**.

Koenig, T., M Zuber, et al. (2011). "A comparison of various strategies to equalize the lower energy thresholds of a CdTe Medipix2 hexa detector for X-ray imaging applications." Journal of Instrumentation **6**(01): C01074.

La Riviere, P. J. and P. Vargas (2008). "Correction for Resolution Nonuniformities Caused by Anode Angulation in Computed Tomography." Medical Imaging, IEEE Transactions on **27**(9): 1333-1341.

Llopart, X. (2007). Design and characterization of 64K pixels chips working in single photon processing mode, Mid Sweden University. **PhD Thesis**.

Llopart, X., M. Campbell, et al. (2002). "Medipix2: A 64-k pixel readout chip with 55-μm square elements working in single photon counting mode." Nuclear Science, IEEE Transactions on **49**(5): 2279-2283.

Lobatto, M. E., V. Fuster, et al. (2011). "Perspectives and opportunities for nanomedicine in the management of atherosclerosis." Nat Rev Drug Discov **10**(11): 835-852.

Lutz, G. (1999). Semiconductors Radiation Detectors. Verlag Berlin Heidelberg New York, Springer.

Maeda, H. (2010). "Tumor-Selective Delivery of Macromolecular Drugs via the EPR Effect: Background and Future Prospects." Bioconjugate Chemistry **21**(5): 797-802.

Maeda, H., J. Fang, et al. (2003). "Vascular permeability enhancement in solid tumor: various factors, mechanisms involved and its implications." International Immunopharmacology **3**(3): 319-328.

Martin, N. (2006). "Scintillation detectors for x-rays." Measurement Science and Technology **17**(4): R37.

Melzer, T., N. Cook, et al. (2008). "Spectroscopic biomedical imaging with the Medipix2 detector." Australasian Physical & Engineering Science in Medicine **31**(4): 300-306.

Mikulec, B. (2000). Single Photon Detection with Semiconductor Pixel Arrays for Medical Imaging Application. Vienna, University of Vienna, Austria. **PhD Thesis**.

Moghimi, S. M., A. C. Hunter, et al. (2005). "Nanomedicine: current status and future prospects." The FASEB Journal **19**(3): 311-330.

Mohr, J. (2011). Quality Assurance Protocols: Geometrical Alignment. Christchurch.

Niederlohner, D., J. Karg, et al. (2005). "The energy weighting technique: measurements and simulations." Nuclear Instruments and Methods in Physics Research Section A: Accelerators, Spectrometers, Detectors and Associated Equipment **546**(1-2): 37-41.

Owens, A. (2012). Compound Semiconductor Radiation Detectors. Hoboken, Taylor & Francis.

Paul, R. J. (2012). Quantitative soft-tissue imaging by spectral CT with Medipix3. Bioengineering Department. Christchurch, University of Otago. **PhD**.

Pavlo, B., A. Yahya, et al. (2012). "Spectral CT imaging of vulnerable plaque with two independent biomarkers." Physics in Medicine and Biology **57**(13): 4117.

Pfeiffer, K. F. G. (2004). Evaluation of the Medipix Detectors for Medical X-Ray Imaging, with Special Consideration of Mammography, Universitat Erlangen-Nurnberg. **PhD Thesis**.

Poludniowski, G., G. Landry, et al. (2009). "SpekCalc : a program to calculate photon spectra from tungsten anode x-ray tubes." Physics in Medicine and Biology **54**(19): N433.

Popovtzer, R., A. Agrawal, et al. (2008). "Targeted Gold Nanoparticles Enable Molecular CT Imaging of Cancer." Nano Letters **8**(12): 4593-4596.

R Aamir, M. F. W., Stuart P. Lansley, Robert M. Doesburg, Rafidah Zainon, N. J. A. De Ruiter, Philip H. Butler, Anthony P. H. Butler (2011a). "Characterization of CdTe X-Ray Sensor Layer on Medipix Detector Chips." Materials Science Forum (Volume 700) **Advanced Materials and Nanotechnology**: 170-173.

Rabin, O., J. Manuel Perez, et al. (2006). "An X-ray computed tomography imaging agent based on long-circulating bismuth sulphide nanoparticles." Nat Mater **5**(2): 118-122.

Roessl, E. and R. Proksa (2007). "K-edge imaging in x-ray computed tomography using multi-bin photon counting detectors." Physics in Medicine and Biology **52**(15): 4679.

Ronaldson, J. P. (2012). Quantitative soft-tissue imaging by spectral CT with Medipix3. Bioengineering Department. Christchurch, University of Otago. **PhD**.

Ronaldson, J. P., A. P. Butler, et al. (2011). The performance of MARS-CT using Medipix3 for spectral imaging of soft-tissue. Nuclear Science Symposium and Medical Imaging Conference (NSS/MIC), 2011 IEEE.

Ronaldson JP, S. A., Scott N, Butler AP, Butler PH, Anderson NG (2011). Towards quantifying the composition of soft-tissues by spectral CT imaging with Medipix3. RSNA 97th Annual and Scientific Meeting, Chicago, USA.

Ruat, M. and C. Ponchut (2011). Characterization of a X-ray pixellated CdTe detector with TIMEPIX photon-counting readout chip. Nuclear Science Symposium and Medical Imaging Conference (NSS/MIC), 2011 IEEE.

Schlomka, J. P., E. Roessl, et al. (2008). "Experimental feasibility of multi-energy photon-counting K-edge imaging in pre-clinical computed tomography." Physics in Medicine and Biology **53**(15): 4031.

Schmidt, T. G. (2009). "Optimal ``image-based" weighting for energy-resolved CT." Medical Physics **36**(7): 3018-3027.

Seibert, J. A. and J. M. Boone (2005). "X-Ray Imaging Physics for Nuclear Medicine Technologists. Part 2: X-Ray Interactions and Image Formation." Journal of Nuclear Medicine Technology **33**(1): 3-18.

Shikhaliev, P. M. (2005). "Beam hardening artefacts in computed tomography with photon counting, charge integrating and energy weighting detectors: a simulation study." Physics in Medicine and Biology **50**(24): 5813.

Shikhaliev, P. M. (2008). "Energy-resolved computed tomography: first experimental results." Physics in Medicine and Biology **53**(20): 5595.

Shikhaliev, P. M. and S. G. Fritz (2011). "Photon counting spectral CT versus conventional CT: comparative evaluation for breast imaging application." Physics in Medicine and Biology **56**(7): 1905.

Shiraki, H., M. Funaki, et al. (2007). Improvement of the productivity in the growth of CdTe single crystal by THM for the new PET system. Nuclear Science Symposium Conference Record, 2007. NSS '07. IEEE.

Shiraki, H., M. Funaki, et al. (2010). "Improvement of the Productivity in the THM Growth of CdTe Single Crystal as Nuclear Radiation Detector." Nuclear Science, IEEE Transactions on **57**(1): 395-399.

Soltani, M. and P. Chen (2012). "Effect of tumor shape and size on drug delivery to solid tumors." Journal of Biological Engineering **6**(1): 4.

Spieler, H. (2006). *Semiconductor Detector Systems*, Oxford University Press.

Stolzmann, P., H. Scheffel, et al. (2008). "Dual-energy computed tomography for the differentiation of uric acid stones: ex vivo performance evaluation." Urological Research **36**(3): 133-138.

Ta, H. T., S. Prabhu, et al. (2011). "Enzymatic Single-Chain Antibody Tagging / Novelty and Significance." Circulation Research **109**(4): 365-373.

Taguchi, K., E. C. Frey, et al. (2010). "An analytical model of the effects of pulse pileup on the energy spectrum recorded by energy resolved photon counting x-ray detectors." Medical Physics **37**(8): 3957-3969.

Taguchi, K., S. Srivastava, et al. (2009). Enabling photon counting clinical X-ray CT. Nuclear Science Symposium Conference Record (NSS/MIC), 2009 IEEE.

Thurn, K., E. Brown, et al. (2007). "Nanoparticles for Applications in Cellular Imaging." Nanoscale Research Letters **2**(9): 430 - 441.

Tlustos, L. (2005). Performance and limitations of high granularity single photon processing X-ray imaging detectors, Technischen Universitat Wien. **PhD**.

Tlustos, L., R. Ballabriga, et al. (2006). "Imaging properties of the Medipix2 system exploiting single and dual energy thresholds." Nuclear Science, IEEE Transactions on **53**(1): 367-372.

Tobi Reuveni, M. M., Zimam Romman, Aron Popovtzer and Rachela Popovtzer (2011). "Targeted gold nanoparticles enable molecular CT imaging of cancer: an in vivo study." Int J Nanomedicine: 6.

Tran, D. N., M. Straka, et al. (2009). "Dual-energy CT Discrimination of Iodine and Calcium: Experimental Results and Implications for Lower Extremity CT Angiography." Academic Radiology **16**(2): 160-171.

Ulbrich, W. and A. Lamprecht (2010). "Targeted drug-delivery approaches by nanoparticulate carriers in the therapy of inflammatory diseases." Journal of The Royal Society Interface **7**(Suppl 1): S55-S66.

Vancraeynest, D., A. Pasquet, et al. (2011). "Imaging the Vulnerable Plaque." Journal of the American College of Cardiology **57**(20): 1961-1979.

Vital Peretz, M. M. C., N. Sukenik and Rachela Popovtzer (2012). "The Effect of Nanoparticle Size on Cellular Binding Probability." Journal of Atomic, Molecular, and Optical Physics **Volume 2012** 7 pages.

Weber, M. J. (2002). "Inorganic scintillators: today and tomorrow." Journal of Luminescence **100**(1–4): 35-45.

Weber, W. A., J. Czernin, et al. (2008). "Technology Insight: novel imaging of molecular targets is an emerging area crucial to the development of targeted drugs." Nat Clin Prac Oncol **5**(1).

Weissleder, R. (2006). "Molecular Imaging in Cancer." Science **312**(5777): 1168-1171.

Wickline, S. A., A. M. Neubauer, et al. (2007). Targeted nanoparticle contrast agents for vascular molecular imaging and therapy. The Vulnerable Plaque**:** 289-302.

Wojtowicz, A. J. (2002). "Rare-earth-activated wide bandgap materials for scintillators." Nuclear Instruments and Methods in Physics Research Section A: Accelerators, Spectrometers, Detectors and Associated Equipment **486**(1–2): 201-207.

Writing Group, M., V. L. Roger, et al. (2012). "Heart Disease and Stroke Statistics—2012 Update." Circulation **125**(1): e2-e220.

Xue, Y., S. Zhang, et al. (2012). "Acute toxic effects and gender-related biokinetics of silver nanoparticles following an intravenous injection in mice." Journal of Applied Toxicology **32**(11): 890-899.

Yamamoto, S., J. McWilliams, et al. (2009). "Dual-energy CT angiography of pelvic and lower extremity arteries: dual-energy bone subtraction versus manual bone subtraction." Clinical Radiology **64**(11): 1088-1096.

Yang K, K. A., Miller DF, Boone JM. (2006). "A geometric calibration method for cone beam CT systems." Med Phys **33**(6): 1695-1706.

Yu, H., Q. Xu, et al. (2012). "Medipix-based Spectral Micro-CT." CT Theory and Applications **21**(4).

Zainon, R., J. Ronaldson, et al. (2012). "Spectral CT of carotid atherosclerotic plaque: comparison with histology." European Radiology: 1-8.

Zainon, R. B. (2012). Spectral Micro-CT Imaging of Ex Vivo Atherosclerotic Plaque Physics & Astronomy Department. Christchurch, University of Canterbury. **PhD Thesis**.

Zhang, L., F. Gu, et al. (2007). "Nanoparticles in Medicine: Therapeutic Applications and Developments." Clin Pharmacol Ther **83**(5).

Zhu, S., J. Tian, et al. (2009). "Cone Beam Micro-CT System for Small Animal Imaging and Performance Evaluation." International Journal of Biomedical Imaging **2009**.